MULTIBEAM ANTENNA DESIGN FOR ADVANCED WIRELESS COMMUNICATION SYSTEMS

by

Yubo Wen

A thesis submitted in fulfilment of the requirements
for the degree of

Doctor of Philosophy
in
Engineering

under the supervision of
Associate Prof. Pei-Yuan Qin and Prof. Y. Jay Guo

to

School of Electrical and Data Engineering
Faculty of Engineering and Information Technology
University of Technology Sydney
NSW - 2007, Australia

June 2023

CERTIFICATE OF ORIGINAL AUTHORSHIP

I, Yubo Wen, declare that this thesis is submitted in fulfilment of the requirements for the award of DOCTOR OF PHILOSOPHY, in the Faculty of Engineering and Information Technology at the University of Technology Sydney.

This thesis is wholly my own work unless otherwise referenced or acknowledged. In addition, I certify that all information sources and literature used are indicated in the thesis.

This document has not been submitted for qualifications at any other academic institution.

This research is supported by the Australian Government Research Training Program.

Signature: Production Note: Signature removed prior to publication.

Date: June 19, 2023

Abstract

Multibeam antennas (MBAs) have gained significant attention as essential components in the development of advanced wireless communication systems, particularly for Beyond Fifth Generation (B5G) and Sixth Generation (6G) networks. They enhance beam coverage, serving multiple users simultaneously with commercial advantages over digital or hybrid alternatives.

Chapter 1 discusses the background of MBA design and applications. Chapter 2 provides a comprehensive review of the Fourier transform (FT), a valuable tool in antenna analysis and design. This review establishes the foundational basis for the subsequent analysis discussed in the following chapters.

In the next few chapters, this thesis focuses on three critical issues in MBA design: coverage, compactness, and directivity.

In the third chapter, the thesis explores the coverage aspect of MBAs, with a specific focus on full azimuthal coverage. As an example, the thesis presents a design of a multiport circular array of endfire Yagi-Uda monopoles. The thesis investigates and mitigates the known issue of a vertical monopole antenna on a finite-sized ground plane radiating an elevated beam. The simulated and measured results of a sector of this circular array validate the concepts.

The thesis then explores the utilization of metamaterials or metasurfaces to achieve compact MBA designs.

In the fourth chapter, fundamental concepts of modeling metasurfaces are reviewed, starting from general sheet transition conditions (GSTCs) and extending to impedance boundary conditions (IBCs). Based on IBCs and modulated metasurfaces (MTS), the single beam compact antennas and a seven-beam antenna have been designed.

Furthermore, in the fifth chapter, the thesis explores the application of the shared aperture approach to enhance the directivity of each MBA beam. The thesis addresses the challenges of mutual interference between different impedance modulations in MTS and presents a design method. A seven-beam MTS antenna validates the design method, and the fabrication and measurement of the antenna confirm its successful implementation.

In the final chapter, the conclusion is presented along with a discussion on potential future work.

In summary, this research contributes to advancing MBA technologies, enhancing coverage, compactness, and directivity for specific antenna designs.

Keywords: Multibeam antennas, coverage, compactness, directivity, beam scanning, metamaterials, metasurfaces, modulated metasurface.

Acknowledgments

It feels unbelievable that I've been a PhD student at UTS for almost four years. Time has gone by so quickly, and it's been a journey filled with unexpected challenges, especially with the pandemic hitting in 2019. When I return to the university after the pandemic, in the morning of some days, I can't help but be amazed that I'm in Sydney, one of the best cities I've ever visited. None of this would have been possible without the incredible help from my supervisors, professors, and colleagues who have become dear friends.

First and foremost, I want to thank Prof. Pei-Yuan Qin for his constant guidance, support, and help throughout my four-year research journey. Prof. Qin is a dedicated and motivated researcher who always encourages me to take responsibility for my life and career. His ability to solve complex engineering problems is impressive and has inspired me to do the same.

I also want to express my heartfelt appreciation to my co-supervisor, Prof. Y. Jay Guo, who is internationally recognized for his expertise in antenna design. I'm grateful for his patience, guidance, and valuable feedback during my time at UTS. Prof. Guo has a knack for identifying the main issues in complicated problems and helping us find quick solutions, which is essential in real-world engineering. On a personal level, I admire his sense of humor and open-mindedness, which have had a positive impact on me.

A special thanks goes to Prof. Richard W. Ziolkowski, a humble and knowledgeable researcher, for his invaluable suggestions and comments on my work. Prof. Ziolkowski's expertise and experience have greatly influenced my research. I'm thankful for his willingness to help, even with the most basic problems. His support has been invaluable to me.

I would also like to express my heartfelt gratitude to Prof. Stefano Maci from University of Siena, Italy for his assistance with my paper. Without his help, the paper wouldn't have been as clear for readers. I appreciate his expertise and guidance, which have significantly improved the quality and impact of my research.

I would like to sincerely thank Dr. Bevan Jones, Dr. Can Ding, and Dr. Shulin Chen for their unwavering support and help throughout my academic journey. Their guidance and expertise have been incredibly valuable in shaping my research and personal growth.

I also want to express my heartfelt appreciation to Dr. Xuan Wang, Dr. Maral Ansari, Dr. Lizhao Song, Dr. He Zhu, Dr. Hao Zhang, Dr. Wei Lin, Dr. Tianyu Yang and Dr. Haihan Sun for their invaluable help and support, both academically and personally.

Furthermore, I am deeply grateful to my colleagues, including Gengming Wei, Dr. Hongyang Zhang, Dr. Ming Li, Yang Xu, Shangyi Sun, Fanchao Zeng, Xingyu Cheng, Yi He, Zhaoqi Cui, and David Thomas, for their assistance and support. Their collaboration, friendship, and expertise have been invaluable in both my professional and personal life.

I would also like to extend my gratitude to Kevin Sharp and Dr. Majid Amiri for helping me with antenna measurements, as well as Brett Lowder amd Dr. Farhana Afroz for their support during lab classes. I would also like to thank Dr. Anh Tuyen Le for giving me the opportunity to participate in the measurements for his board.

Thanks for Xinyuan Liu, Ruotong Hu, Xiaole Zhang and Trong-Dai Hoang, with whom I have shared many wonderful moments outside of work. I would like to give a special thanks to Katie Gypsiotis, Genie Tan and Aprillia Tanudjaja for their invaluable assistance with the administrative processes related to my studies.

I am grateful for the early guidance and support provided by Dr. Renzun Lian and Dr. Meng Zou at the beginning of my research.

To my friends, Dr. Yuyue Luo, Ying Zhou, Yaohui Wang, Dr. Guozhang Chen, Guangsen Yue, Xingkui Feng, Yichen Li, I am sincerely thankful for their help and support. The care and encouragement from them have been the driving force behind my efforts.

Lastly, I want to extend my heartfelt thanks to my family members, especially Huiling Zeng. Without their unwavering support and assistance, completing this work would have been impossible.

List of Publications

Peer-reviewed Journal Articles :

1. **Yubo Wen**, Peiyuan Qin, Gengming Wei and Richard. W. Ziolkowski, "Circular Array of Endfire Yagi-Uda Monopoles With a Full 360 degree Azimuthal Beam Scanning," *IEEE Transactions on Antennas and Propagation*, vol. 70, no. 7, pp. 6042-6047, July 2022.

2. **Yubo Wen**, Peiyuan Qin, Stefano Maci, and Y. Jay Guo, "Low-profile Multi-beam Antenna Based on Modulated Metasurface," *IEEE Transactions on Antennas and Propagation*, doi: 10.1109/TAP.2023.3281677.

Peer-reviewed Conference Articles :

3. **Yubo Wen** and Peiyuan Qin, "Yagi-Uda Monopoles with Elevated-Angle Suppression for Endfire Radiation," *2022 International Symposium on Antennas and Propagation (ISAP)* , Sydney, Australia, 2022.

4. **Yubo Wen**, Peiyuan Qin, and Y. Jay Guo, "A Multi-Beam Antenna Based on Modulated Metasurface," *2023 5th Australian Microwave Symposium (AMS)*, Melbourne, Australia, 2023..

5. **Yubo Wen**, Peiyuan Qin, and Y. Jay Guo, "A Low Profile Modulated Metasurface Antenna for Multi-Beam Applications," *2023 17th 2023 17th European Conference on Antenna and Propagation (EuCap)*, Florence, Italy, 2023.

TABLE OF CONTENTS

List of Tables

ABBREVIATIONS

B5G - beyond fifth generation

IF - intermediate frequency

RF - radio frequency

DDA - discrete dipole approximation

ESPARs - Electronically steerable parasitic array radiators

FT - Fourier transform

FFT - fast Fourier transform

GSTC - general sheet transition condition

IBC - impedance boundary condition

MBA - multiple beam antenna

MIMO - multiple-input multiple-output

mm-wave - millimeter-wave

MoM - method of moments

MTM - metamaterial

MTS - metasurface

NLOS - non-line-of-sight

SVWF - spherical vector wave function

SLL - side lobe level

CHAPTER 1

INTRODUCTION

This chapter aims to provide an overview of the context and importance of the research conducted in this thesis. It begins by discussing the background and significance of the study, as well as the current state of research in this field. The chapter then focuses on the key problems and challenges addressed by this thesis, highlighting the contributions and innovations that this research brings to the field. Finally, an outline of the structure of the thesis is presented.

1.1 Research Background and Significance

In this section, we will focus on the definition and the application of multibeams in advanced wireless communication.

1.1.1 Multibeam systems

A Multibeam system refers to a system capable of supporting multiple independent beams, and it can be implemented through a variety of approaches. When considering

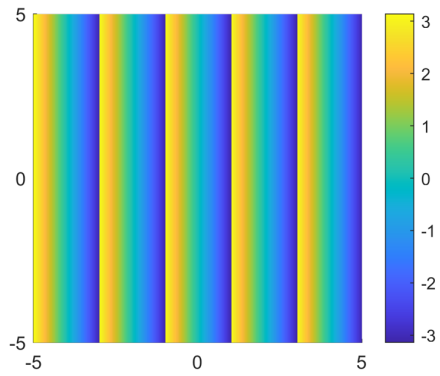

Figure 1.1: Phase distribution on a $10\lambda \times 10\lambda$ aperture for a 30° beam.

different beam angles, it signifies that the aperture fields of the antenna exhibit a specific phase distribution, e.g. Figure. 1.1. While amplitude modulation is often introduced for purposes such as achieving low side lobe levels, this discussion will focus solely on phase distribution for brevity. The methods to realize multiple beams involve achieving multiple phase distributions simultaneously in some way.

As is widely known, the phase can be adjusted along the signal channel, spanning from the baseband, intermediate frequency (IF) band, radio frequency (RF) band, and extending to the antenna itself. For instance, in the baseband scenario, multiple beams can be formed in the digital domain. In the IF case, channel phases can be adjusted using local oscillators. In the RF case, the phase of the channels can be tuned using phase shifters or complex feeding networks. For MBAs, the ultimate goal of a multibeam system is realized at the antennas, which forms the central focus of this thesis.

It is evident that, aside from the baseband and antenna scenarios, intricate feeding networks are necessary. Nevertheless, in the baseband case, the requirement for numerous RF channels leads to an escalation in the overall system cost and power consumption. Conversely, in the antenna case, the system's complexity is concentrated on the antenna itself, simplifying the overall system and affording more room for antenna designers to make meaningful contributions.

1.1.2 Multibeam antennas

A Multibeam antenna (MBA) is an advanced antenna system capable of generating multiple high-gain beams in different directions. It serves as a fundamental component in advanced wireless communication systems, enabling the simultaneous provision of multiple independent beams to serve users across various regions as shown in Figure. 1.2. On the other hand, in certain scenarios such as mobile users, tracking becomes essential. MBAs offer the capability to scan and track users by utilizing switches to activate different beams dynamically as shown in Figure. 1.3.

In the first scenario, MBAs utilize multiple directive beams to cover different directions. MBAs offer higher gain and better connection reliability than conventional wireless communication systems that use single-beam coverage. When compared to conventional MIMO technology with similar antennas, MBAs are capable of covering a region of interest with multiple independent directive beams, each with high gain values. This provides rich spatial channel information, making it a valuable tool for wireless communication system optimization. However, the complexity and cost of the antenna system increase due to the need for beam selection and management.

In the second scenario, similar to the first one, the high-gain beams of MBAs can be scanned towards different directions using switches. This approach provides a simplified feeding network compared to conventional phased arrays. The advantage lies in the reduced complexity and cost associated with the feeding network of the MBA system. In satellite communications, some antenna systems have been proposed based on MBAs and phased array diagram as shown in Figure. 1.3.

It is noting that MBA can be categorized into two kinds according to the number of the feeds. In this thesis, we will focus on the multiple port multiple beam case. However, we will also give some examples for single port multiple beam case for the purpose of comparison.

Figure 1.2: Application scenario 1: cover varies regions.

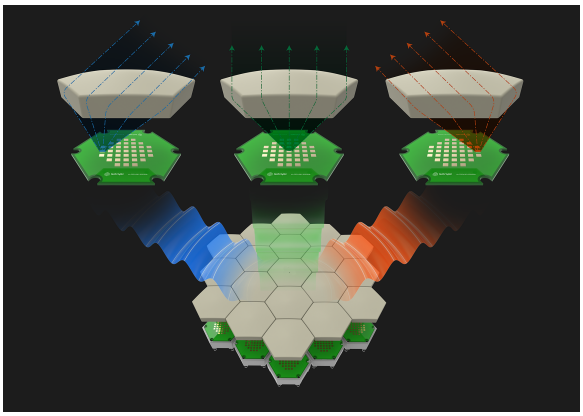

Figure 1.3: Application scenario 2: tracking [1].

1.2 Research History and State

The focus of this thesis is the design of high-performance MBAs for modern wireless communication systems. This subsection provides an overview of the history and current state of MBA design.

In the following discussion, we will categorize MBAs briefly based on their working principles. However, it's important to note that designs utilizing quasi-optical MBA technologies can be found in most of these categories and will be separately introduced.

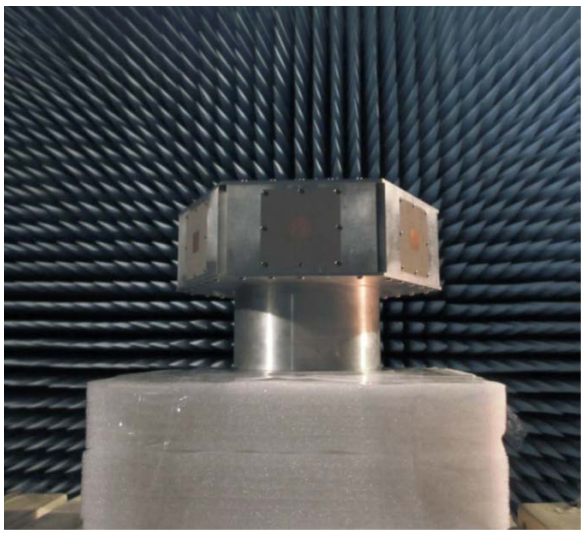

Figure 1.4: A MBA based on circularly located antenna units [2].

1.2.1 Category of MBAs

Multi-port MBAs can be classified into two main categories based on their working principles.

The first category involves arranging subarrays or antenna units in such a way that they cover different directions. Each subarray or antenna unit is responsible for generating a specific beam in a particular direction. This approach allows for independent control and adjustment of each beam direction.

The first method, as illustrated in Figure. 1.4, is the simplest approach to implement MBAs. It involves utilizing subarrays or individual antenna units to cover different directions. However, one limitation of this approach is that the effective region of the antenna, where high gain is achieved, is confined to a sector corresponding to the direction covered by each subarray or antenna unit. Consequently, this limitation can impose restrictions on the maximum gain for beams directed towards specific directions.

The second category involves sharing the entire antenna structure among all the beams, regardless of their respective directions. In this case, the same antenna structure is utilized to generate beams in different directions. This approach offers the advantage

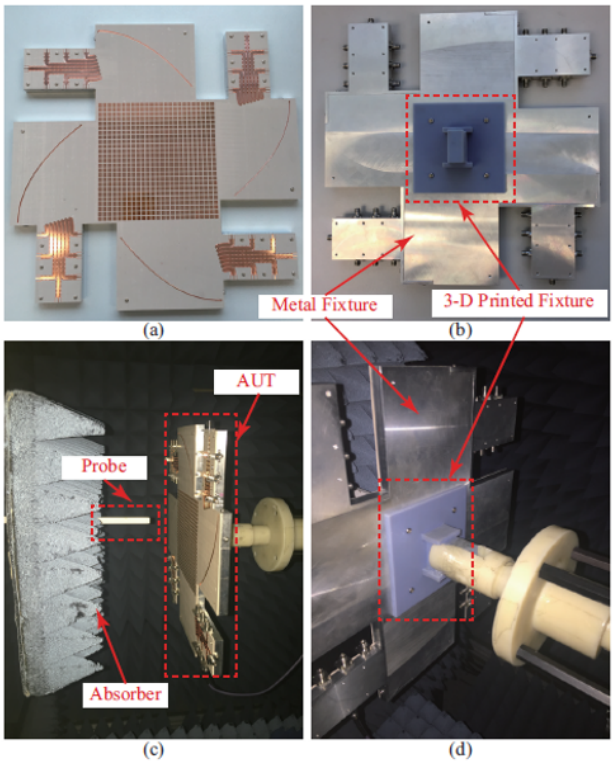

Figure 1.5: A Shared aperture MBA [3].

of reduced complexity and potentially lower cost, as the same structure is shared among multiple beams [3].

By sharing the aperture, this approach offers the advantage of increased flexibility in beam steering and beamforming. However, it is important to note that the sharing of the aperture among different beams may introduce some trade-offs in terms of beam quality, gain, and sidelobe levels. Design considerations must be made to optimize the performance of each beam while utilizing the shared aperture efficiently.

Overall, the second method provides a more compact and potentially cost-effective solution by sharing the aperture among different beams, but it requires careful engineering to achieve desired performance characteristics. While the first solution still holds significant relevance in certain applications, such as end-fire MBAs.

Regarding to design methods, MBAs can be implemented using various methods,

such as Quasi-optical technology, phased arrays, and beamforming networks. Each of these methods constitutes a substantial topic [4]. Notably, the core concept of phased arrays and beamforming networks revolves around the feeding network in analog and or digital domains. Our preference lies in designing antennas based on the antenna structure itself rather than emphasizing the feeding network. Consequently, this section will focus on reviewing Quasi-optical technology.

1.2.2 Quasi-Optical MBA technology

The early history of antenna design, many classic designs were developed without a comprehensive understanding of electromagnetic theory. Instead, these designs were influenced by concepts from optics. One notable example is the parabolic reflector, which finds its origins in optical reflector systems. This approach, known as quasi-optical technology, continues to be valuable for antenna designs in advanced wireless communication systems. The experience gained from designing in the optical frequency range can be applied and adapted to antenna design in other frequency ranges.

Based on Quasi-Optical technology, there are many terms can be utilized in the designs, such as focal point, focal length. For MBAs, actually, we are seeking the so called "multi-focal" design. Usually, lens, transmit-array and reflect-array can be utilized in MBA designs.

1.2.2.1 Lens

The lens is one of the most widely used and classic antennas for MBA designs. It serves the purpose of transforming a spherical wavefront into a planar one, applicable to both three-dimensional (3D) and two-dimensional (2D) cases. The idea of utilizing lenses to generate multiple beams can be traced back to the 1950s when they were first employed in radar applications [5]. Recently, this solution has found commercial applications due

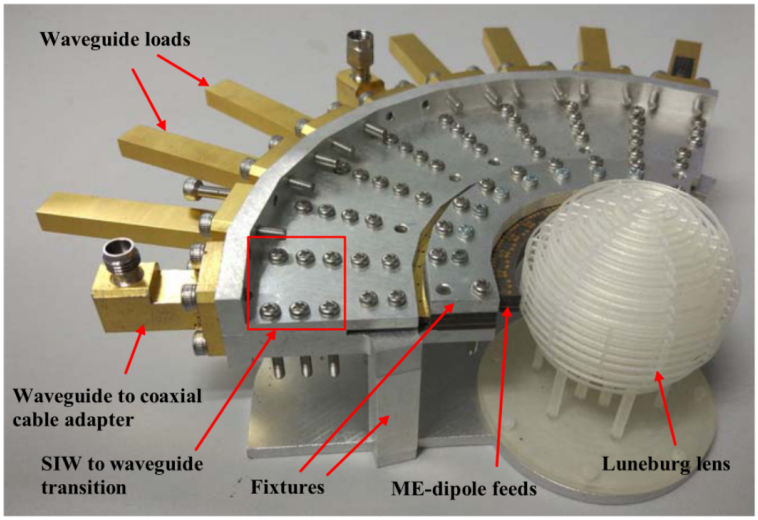

Figure 1.6: Lunebrug lens [6].

to the advancements in millimeter-wave (mm-wave) technology and the utilization of metamaterials. These developments have facilitated the practical implementation of lens-based solutions in various industries.

As mentioned earlier, a lens has the ability to transform a spherical wavefront into a planar one. The spherical wavefront is typically generated by a source positioned at a focal point within the lens. If multiple focal points can be introduced into the lens through various means, it becomes possible to design a MBA. Based on this, the common-used lens, such as Ruze lens, Rotman lens and Luneburg lens (as shown in Figure. 1.6) can be utlized to realize a MBA by introducing such multiple focal points for both 2D and 3D case [6].

One of the advantages of lens-based MBAs is their ability to provide wide coverage due to the utilization of the structural symmetry. The symmetrical arrangement of the focal points enables the generation of beams with consistent characteristics across a wide angular range.

One of the limitations of MBA systems based on lenses is their dimensions. Due to the physical size and configuration of the lens elements, these antennas may become

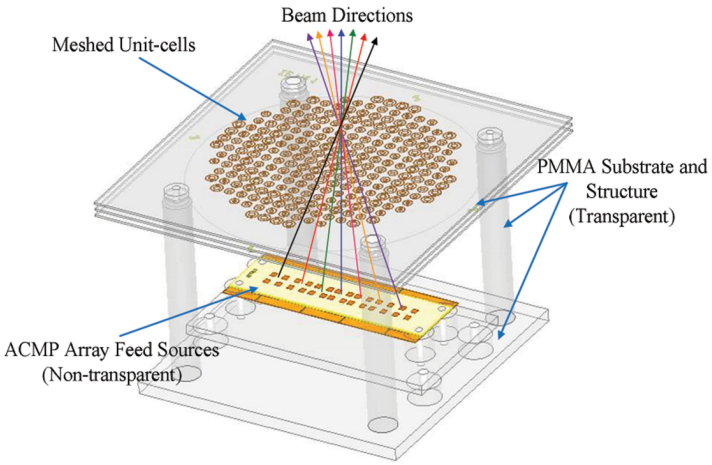

Figure 1.7: MBA based on transmit-array [8].

larger in size compared to other antenna designs. The increased size can limit their practicality in certain applications where space is constrained. It is important to consider these limitations while designing and implementing lens-based MBA systems and to evaluate the trade-offs between coverage, size, and aperture efficiency (AE) in order to optimize their performance for specific applications.

1.2.2.2 Transmit-Array and Reflect-Array

Transmit-arrays, initially proposed by McGrath [7], are thin, multilayered structures that can be either planar or conformal. They are primarily used in high directivity applications. The fundamental principle behind beam steering in transmit-arrays involves manipulating the phase delay across the surface to achieve phase shifting [8]. Such designs offer several benefits, including the absence of feed blockage and the potential for reducing the focal distance, resulting in more compact antenna systems.

Reflect-array antennas were first introduced in the 1960s [9], combining the benefits of both array theory and geometrical optics. Reflector antennas rely on shaped reflective surfaces and prescribed illumination to achieve the desired radiation characteristics. Their operation is analogous to mirrors in optics, where reflection and redirection of

waves enable control over the radiation pattern and beam characteristics.

One of their primary advantages is the flexibility they offer in array designs, as they do not require complex beamforming systems. Reflect-arrays are composed of an aperture or surface that has a specific reflection coefficients, as well as a primary radiator that illuminates it. The performance of reflector-based MBAs can be improved by modifying the shape of the reflector, optimizing the design of the feeding antennas, and adjusting the relative orientation and positioning of the reflector with respect to the feed antennas.

The comprehensive review on this topic can be found in [10] and [4].

1.2.3 Surface-Wave MBAs

In this subsection, we will review the design of MBAs based on surface wave propagation. These antennas are specifically relevant to advanced wireless communication systems due to their compactness and associated benefits.

In electromagnetism, surface waves refer to electromagnetic waves that propagate along an interface, where the energy is concentrated. The study of surface waves in electromagnetism dates back to 1909 when Zenneck and Sommerfeld first investigated overground propagation [11, 12]. However, it was not until the 1960s that comprehensive theoretical studies on different types of surface waves and the discovery of new applications emerged. In the last decade, there has been a growing interest in the exploration of surface waves and their potential applications.

Typically, when a suitable interface is present, electromagnetic waves can be guided along that interface, essentially acting as a waveguiding structure. Extensive research and studies on such waveguiding interfaces have been reviewed in the reference [13].

In the case of surface wave antennas, the interface serves a dual purpose: waveguiding and radiation. The name "surface wave antenna" is derived from the fact that the energy appears to "leak" or radiate from the interface. In these antennas, the interface not

only guides the waves along its surface but also facilitates their radiation into free space. The concentrated energy near the interface leads to the emission of surface waves, contributing to the antenna's radiation pattern and overall performance.

The structure supporting surface waves, referred to as a surface waveguide, is typically analyzed using conventional eigenmode methods outlined in [14]. However, these surface waveguides are homogenous surfaces, lacking spatial modulation. To design antennas based on such surface waveguides, modulation needs to be introduced. Oliner and Hessel detailed sinusoidally modulated scalar impedance surfaces, crucial for antenna design on low-profile impedance surfaces [15]. In 2010, [16] has developed MTS leaky-wave 2D antenna by using a design inspired by a holographic concept. [17] extended Oliner-Hessel theory to sinusoidally modulated tensor impedance surfaces. The same group introduced a more general form of modulation for amplitude, phase, and polarization control of waves and fields [18]. The fundamental concept in these methods remains consistent: the eigenmodes of surface waveguides.

Similar to the analysis for microstrip lines in [14], the eigenmodes of the non-modulated surface waveguide are initially examined. Introducing modulation causes the orthogonal eigenmodes to couple with other modes. Fortunately, radiation is one of the modes for surface waveguides. The analysis reveals the coupling relationships among the modes, allowing for the connection of radiation with the corresponding mode in antenna design. This enables the completion of antenna design using various methods with highly effective feedback.

Drawing inspiration from the concept of the modulated surface waveguide, various low-profile MBAs have been put forth. One notable example is a Si/GaAs metasurface (MTS) antenna designed to operate at 94 GHz [19]. This antenna presents holographic beam shaping and steering capabilities, all achieved without the necessity of intricate phase-shifting circuits.

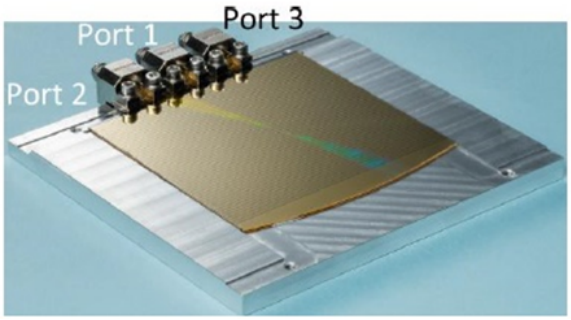

Figure 1.8: Fabricated Si/GaAs MTS antenna placed on a supporting structure for characterization [19].

In [20], the possibility of designing multibeam antennas using a single circular MTS aperture has been demonstrated. Three different solutions were studied in this research.

The first two solutions utilize a single source to generate N simultaneous beams. In the first solution, the aperture is divided into N angular sectors, each supporting the necessary modulation for beam production in the desired direction. However, this approach has a lower beam efficiency (approximately 18% for four beams) despite amplitude-field control.

The second solution involves adding up the modulations for each individual beam across the entire MTS aperture, resulting in higher gains compared to the sector-divided aperture. Sharing the aperture increases beam efficiency by a factor of three.

The third approach introduces multiple feeds to achieve independent control of the beams. Each source can activate one beam at a time or detect the direction of an incoming signal by selecting the appropriate port. The beams produced are quasi-orthogonal, providing an advantage in processing signals from different directions. While a single-source multibeam antenna is useful for simultaneously transmitting signals to different locations, it has limitations in reception as the feed terminal cannot distinguish between different directions of arrival.

The paper [21] explores the multibeam and beam-scanning capabilities of MTS antennas using multiple feeds. Two approaches are investigated: one based on a discrete

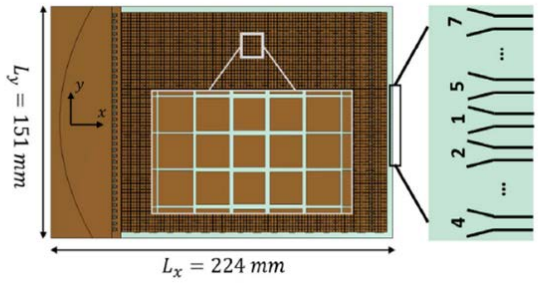

Figure 1.9: Top view of MTS antenna. Disposition of patches and ports in the pillbox beamformer [22].

azimuthal symmetry assumption and the other without any prior assumptions on the impedance profile. The research demonstrates the feasibility of achieving multibeam functionality, polarization diversity, and continuous beam scanning using MTS antenna designs.

In paper [22], a new modulated MTS antenna topology for wireless backhaul at the K band is proposed, as shown in Figure. 1.9. This antenna design incorporates a quasi-optical beamformer and a modulated MTS radiating aperture, vertically stacked in a two-layer pillbox architecture. The result is a compact antenna capable of generating multiple beams at different pointing angles.

1.3 Application Requirements and Challenges

From the research history and the state discussed in the last subsection, the application requirements and challenges behind the design of MBAs will be summarized in this subsection.

1.3.1 Coverage

In a conventional single beam antenna system, the coverage of a certain region is achieved by utilizing a single beam that delivers the signal uniformly throughout that

region, regardless of the location of the receiving terminal. However, in wireless communication systems incorporating MBAs, the coverage of a specific region is accomplished through the use of multiple beams with high gain. In addition to achieving high gain, ensuring comprehensive coverage is a crucial factor in MBA design.

There are several methods available to achieve the desired coverage using MBAs. One approach involves carefully arranging the antenna units or feeds in a strategic manner to ensure proper gain overlap and effectively cover the desired regions. By optimizing the arrangement of the antenna units or feeds, the beams generated by the MBA can be directed towards the intended coverage areas, resulting in enhanced coverage performance. This is very similar to the MBA shown in Figure. 1.4.

Another method to achieve the desired coverage is by employing a shared aperture design with well-arranged feeds. In this approach, the antenna aperture is shared among multiple feeds, each strategically placed to cover specific regions of interest. By carefully designing the distribution of the feeds and their corresponding beamforming capabilities, the MBA can generate multiple beams that collectively cover the desired regions effectively. The lens shown in Figure. 1.6 is an example.

Both of these methods, whether through careful arrangement of antenna units/feeds or utilizing a shared aperture with well-arranged feeds, aim to ensure comprehensive coverage in wireless communication systems employing MBAs. By leveraging the high-gain capabilities of MBAs and optimizing the distribution of beams, these methods enable efficient and effective coverage across the intended regions, enhancing the overall performance of the wireless communication system.

1.3.2 Compactness

Compactness is a crucial requirement for MBAs to enable integration with other components and achieve a compact overall system. However, many existing MBAs suffer from

being bulky and having a high profile, which can restrict their potential applications. This is particularly evident in antennas utilizing lenses, as well as transmit/reflect-arrays, where the source is often located far away from the aperture. The need for a large structure to accommodate this distance can result in an antenna with a bulky and high-profile design, limiting its practicality in certain scenarios.

To overcome these limitations and design MBAs with a low profile, various methods have been explored. Researchers have sought innovative approaches to reduce the size and profile of MBAs while maintaining their desired performance characteristics. These methods are shown as follows.

One solution involves modifying the current MBA structure to a more compact version. The Transforming Optics (TO) method can be employed for such transformations [23] shown in Figure. 1.10. While the existing design, such as the refractive index distribution, is already known, TO allows obtaining a compact version with similar performance. However, a challenge with this method is that TO is typically designed for 2D cases, and when applied to rotationally symmetric lenses, complications arise. Additionally, TO may result in a complex material, rather than an isotropic one, posing challenges for antenna design.

Another approach is selecting a compact antenna to achieve MBAs, like the surface wave antenna. However, this solution introduces its own set of problems, as the surface itself becomes the sole entity to accommodate waves, leading to high interference. This issue will be explored further in Chapter 5 of this thesis [24].

Furthermore, alternative methods can be considered. For instance, utilizing metasurface synthesis, it's possible to reduce the distance between the metasurface and the source, as demonstrated in [25] shown in Figure. 1.11. However, challenges with this method include the accuracy of the synthesis process and the realization of the metasurface. The current complexity of metasurfaces makes their design challenging, and for

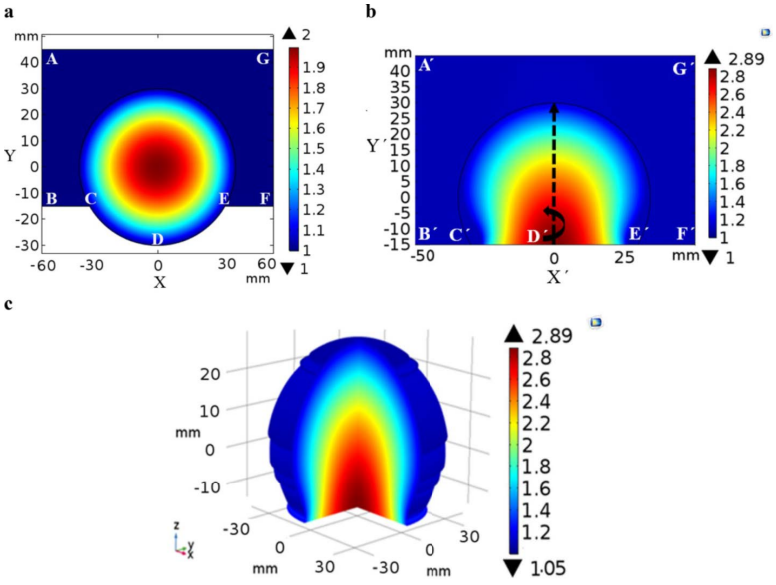

Figure 1.10: MBA based on modified Luneburg lens [23].

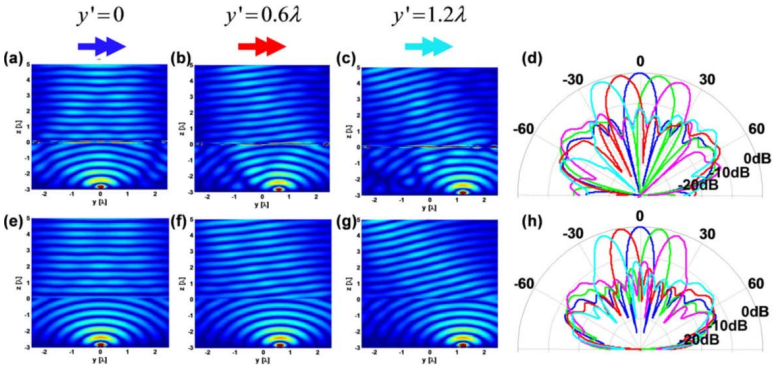

Figure 1.11: MBA based on Huygens' metasurface [25].

practical applications, bandwidth remains a concern.

1.3.3 Directivity

To improve the gain of each beam in MBAs, the utilization of a large aperture is often employed. Efforts are made to enhance the AE of each beam, ensuring that a significant portion of the incident power is radiated in the desired direction. Various techniques are employed to achieve high AE in MBA designs.

When designing lenses for multiple beam usage, optimization techniques based on

optical theory are employed. Both the shape of the lens and the location of the feeds can be carefully optimized to maximize the AE. By considering factors such as focal length, curvature, and feed arrangement, the lens can be designed to efficiently collimate and direct the incoming radiation to the desired beams, resulting in improved AE.

In the case of surface-wave antenna designs, MTSs are used to improve the AE. A MTS is carefully designed and shared among different beams to enhance the radiation efficiency for each beam. The MTS elements are engineered to manipulate the surface waves and control their propagation direction, ensuring that a larger portion of the power is radiated in the desired direction, thus improving the AE.

By employing these optimization techniques and utilizing MTSs, the AE of each beam in MBAs can be significantly improved. This leads to enhanced gain and better utilization of the available aperture, resulting in improved performance and more efficient beam coverage. The ongoing research and development in aperture design for MBAs aim to further optimize the AE and achieve even higher gains for each beam, enabling advanced applications in wireless communication and other fields.

1.4 Contributions and Innovations of This Thesis

Considering the three application requirements discussed in previous section, this thesis has made significant contributions and introduced innovative solutions. The contributions and innovations can be summarized as follows:

Coverage Requirement: To address the coverage requirement in MBA antenna design, a full-360° azimuth coverage end-fire array has been proposed. The detrimental effect of the elevated beam generated by a monopole antenna mounted on a finite ground plane, caused by induced currents on the ground plane, was taken into consideration. The insertion of resonant slot structures into the ground plane was demonstrated to suppress this undesirable effect. Additionally, monopole-based Yagi-Uda antennas were developed

with their main beams directed at the endfire direction along the horizontal plane, resulting in improved realized gain. A circular array of these monopole-based Yagi-Uda antennas was designed and simulated, enabling full azimuthal beam scanning by exciting different sectors formed by sets of these antennas. Measurements of a prototype sector of this array confirmed the effectiveness of the overall design process. The innovative circular array, with its high realized gain and ability to scan the beam for full 360° coverage of the azimuthal plane, is expected to be of practical interest for providing multicell coverage to manage extreme traffic density in wireless ecosystems.

Compactness: regarding the compactness requirement in MBA design, the use of MTSs is indeed a promising solution. The basic concept behind MTSs has been thoroughly investigated, providing valuable insights for the synthesis and design of MTSs. By leveraging the properties of MTSs, a surface-wave antenna has been realized using a modulated MTS approach. This innovative technique allows for the control and manipulation of surface waves, enabling the design of compact antennas. Furthermore, a subarray-based MBA has been designed, taking advantage of the compactness achieved through MTS technology. The subarray-based approach allows for the integration of multiple antenna elements in a smaller physical footprint. This design significantly reduces the overall size of the MBA, making it more suitable for compact applications. However, it is important to note that while compactness is achieved in the MBA design, there may be limitations in terms of AE. The compact nature of the MBA may result in reduced aperture size, leading to lower efficiency in capturing and radiating electromagnetic waves. This trade-off between compactness and AE needs to be carefully considered in the design process.Overall, the utilization of MTSs offers a promising avenue for addressing the compactness requirement in MBA design. The investigation of MTS concepts, the realization of surface-wave antennas, and the development of subarray-based MBAs contribute to achieving compact designs, although it is important to consider the impact

on AE.

High Directivity: In terms of achieving high directivity of the beam, a low-profile 7-beam MTS antenna has been proposed. A new method is presented in the related chapter to address the mutual interference between surface waves excited by multiple ports in an MTS-based MBA. This method employs a time-efficient optimization of the port locations to generate multiple high-gain pencil beams with low side lobe levels (SLLs). A 7-beam prototype is designed, fabricated, and successfully measured to validate the proposed method. The developed MBA offers a compact design solution and is expected to find wide applications in future advanced wireless communication systems where multiple beams are used to serve multiple users simultaneously.

Overall, the contributions and innovations presented in the thesis offer valuable solutions for addressing the coverage, compactness, and high directivity requirements in MBA design. These advancements not only enhance the performance of MBAs but also open up new possibilities for their application in advanced wireless communication systems. These contributions and innovations collectively enhance the overall performance and capabilities of MBAs. By providing solutions for coverage, compactness, and high directivity, the thesis offers valuable insights and advancements for the design and implementation of MBAs in advanced wireless communication systems.

1.5 Outline of This Thesis

The first chapter introduces the background of the research topic. In chapter two, the spectrum technology for antenna analysis for the sequent chapters will be introduced. In chapter three, the proposed end-fired array for achieving 360° azimuth coverage is presented in detail. Chapter Four lists important fundamental concepts related to MTSs and also derives relevant equations for surface MTS antennas. The fifth chapter outlines the design method for MTS MBAs and presents the proposed 7-beam antenna. Finally,

the last chapter draws conclusions based on the findings presented in the preceding chapters.

CHAPTER 2

SPECTRUM DOMAIN ANALYSIS IN ANTENNA DESIGNS

2.1 Chapter Introduction

In this chapter, we will introduce the analysis of the spectrum domain in antenna theory, which plays a crucial role in the design of antennas, including MBAs, for advanced wireless communication systems. Understanding the spectral characteristics of antennas is essential for optimizing their performance and achieving desired outcomes in wireless communication. Throughout this chapter, we will explore various concepts and techniques related to spectrum domain analysis in antenna theory, providing a foundation for the subsequent discussions on MBAs and their applications in the analysis in the subsequent chapters.

Table 2.1: Parameters for time- and space-varying fields

	Period	Frequency	Angular frequency	Relationship
Time-Frequency	T (second)	f=1/T (1/s or Hz)	ω=2πf (rad/s)	f/ξ=c_0
Space-Frequency	λ (meter)	ξ=1/λ (1/m)	k=2$\pi\xi$ (rad/m)	

2.2 Fourier Transform

2.2.1 Parameters for Time- and Space-Varing fields

In signal theory, the analysis typically focuses on the time-varying properties of signals. Fourier transform (FT) is a widely used mathematical tool that has made significant contributions to signal analysis. When studying time-varying properties, such as sinusoidal functions, we can define several key parameters for each harmonic component.

Period T (s) of a sinusoidal function refers to the time it takes for the function to complete one full cycle. It is denoted by the symbol T and is measured in seconds.

Frequency f (1/s or Hz) of a sinusoidal function represents the number of cycles it completes in one second. It is the reciprocal of the period and is denoted by the symbol f. The unit of frequency is hertz (Hz).

Angular frequency ω (rad/s) is closely related to the frequency and is defined as the product of 2π and the frequency. It is denoted by the symbol ω and has units of radians per second.

In the analysis of electromagnetic fields, which are both time-varying and space-varying, we often examine specific points in space or specific moments in time to study their characteristics.

When we study the time-varying properties of electromagnetic fields, we focus on a particular point in space and analyze how the field changes over time. The FT that we mentioned earlier is commonly used to analyze the time-varying characteristics of

electromagnetic fields by introducing the concept of phasor. By applying the FT to a time-varying field, we can obtain its frequency spectrum, revealing the different frequency components present in the field and their corresponding strengths.

On the other hand, when we study the space-varying properties of electromagnetic fields, We concentrate on a specific component at a given frequency (in Hz) and analyze how the field varies across different points in space. In this case, we can use similar mathematical tools to analyze the spatial distribution of the field, such as the spatial FT or other spatial-domain analysis techniques. These methods allow us to examine the field's spatial spectrum, which reveals the distribution of spatial components and their magnitudes across different spatial frequencies or wave vectors.

In summary, the FT is a powerful tool that can be applied to both time-varying and space-varying electromagnetic fields. It enables us to analyze the frequency components in time-varying fields and the spatial components in space-varying fields, providing valuable insights into the characteristics of electromagnetic phenomena.

In spatial domain, the counterparts of the properties such as period, frequency and angular frequency can be found.

Wavelength λ (meter) represents the distance between two consecutive points of similar field behavior in space. It is the counterpart to the period in time-varying analysis.

Spatial frequency ξ (1/meter) represents the rate of change of the electromagnetic field in space and is typically measured in cycles per unit distance. It is often denoted as radians/meter (rad/m). Unlike temporal frequency, which has a specific unit of hertz (Hz) representing cycles per second, spatial frequency is a measure of how rapidly the field changes over a given distance in space.

Wavenumber k (rad/meter) is the counterpart in space-varying analysis just similar to the ω in time-varying analysis. It is defined as the ratio of 2π to the wavelength.

Another property, wavevector (vector wavenumber), which can be defined as $\vec{k}$=$\vec{e}_k$·k where $\vec{e}_k$ is the direction of the wave, includes both magnitude and direction information.

In the analysis of time-varying properties, we are familiar with the FT operation, which allows us to decompose a time-varying signal into its constituent frequency components. Similarly, in the analysis of space-varying properties of electromagnetic fields, we can apply a similar operation to obtain the spectrum of the space-varying fields. This operation is known as the Spatial Fourier Transform (SFT), which allows us to decompose a space-varying electromagnetic field into its constituent spatial frequency components. By applying the SFT, we can obtain the spatial frequency spectrum of the field, which reveals the distribution of spatial components and their magnitudes across different spatial frequencies or wavevectors. This spectrum provides valuable information about the spatial behavior and characteristics of the field.

In the next subsection, the details of the SFT operation and its application in analyzing space-varying properties of electromagnetic fields will be explained. This analysis plays a significant role in antenna design and other advanced wireless communication systems, as it helps in understanding the spatial properties and optimizing the performance of these systems.

2.2.2 Spectrum of Antenna Aperture Fields

In general, the design of antennas emphasizes the distribution of electromagnetic sources. The primary objective of antenna design is to achieve the desired spatial distribution of electromagnetic fields. Extensive research has been conducted on the spatial and spectral characteristics of antenna fields [26].

The analysis of the spectral properties of radiating fields is particularly important for understanding the operating principles of antennas. While the spatial properties of radiating fields are well understood, since antenna designers primarily focus on the

source, which involves spatial distribution, the spectral characteristics of radiating fields require more attention for antenna designers.

Numerous studies have been conducted on the spectral analysis of antennas. In this context, we will present a simplified case for the spectrum analysis of aperture fields, which holds significant relevance in various applications.

From the perspective of the FT, it is known that any periodic function with a well-defined period can be accurately represented using a Fourier series. However, when dealing with aperiodic functions, the situation is different. In such cases, a Fourier series can still be constructed, but the approach involves extending the function periodically in various ways. For example, we can simply assign a value of zero in those regions. As a result, there is no need for a series representation beyond the defined interval.

The FT can be defined as follows in n-dimentional Ruclidean space:

$$\tilde{f}\left(\vec{k}\right) = \int_{\mathbb{R}^n} f(\vec{x}) e^{-j\vec{k}\cdot\vec{x}} d\vec{x} \tag{2.1}$$

where $\vec{k}$ and $\vec{x}$ are vectors in n-dimentional Ruclidean space. "$\cdot$" represents the dot product of two vectors.

By applying the FT to the aperture fields, we can obtain their angular spectrum. This process can be visualized as the expansion of a planar wave. When we analyze the aperture fields using FT, we effectively decompose them into a spectrum of plane waves. Each plane wave corresponds to a specific spatial frequency component. The resulting spectrum provides valuable information about the spatial distribution of the electromagnetic fields generated by the aperture. It reveals the amplitude and phase characteristics of different spatial frequency components, allowing us to understand the behavior and performance of the aperture in terms of its radiating properties.

In antenna engineering, the commonly used radiation pattern provides information about the spectral domain of the antenna. It is significant that the beam characteristics in the far-field region are associated with the field spectrum generated by the impressed

source on the antenna. The radiation pattern is a function that varies with direction, rather than space, as it pertains to the spectral domain rather than the spatial domain.

2.3 Application of Spectrum Domain Analysis

2.3.1 Near-Field to Far-Field Transformation

Following the FT mentioned above, the far-fields of the antenna can be obtained in a simple form by using the method of stationary phase. The FT of the aperture fiels can be understood as an expansion of the fields into plane waves with the same frequency (Hz) but different directions, amplitudes, and phases. Once the amplitudes and phases are obtained, the aperture fields can be reconstructed using these plane waves. However, in practical applications where only the far fields are required, this reconstruction process can be simplified using the method of stationary phase. For example, for a rectangular aperture on ground plane, the far fields can be obtained by using the FT of the aperture fiels as follows [27], which can be viewed as the near-far fields transformation.

$$\vec{E}(r,\theta,\varphi) \approx \frac{jke^{-jkr}}{2\pi r}\left[\hat{e}_\theta\left(\tilde{f}_x\cos\varphi+\tilde{f}_y\sin\varphi\right)+\hat{e}_\varphi cos\theta\left(-\tilde{f}_x\sin\varphi+\tilde{f}_y\cos\varphi\right)\right] \tag{2.2}$$

As an example, the fast FT (FFT) based near-field to far-field transformation has been utilized for a standard horn operating at 1.645 GHz. The results agree well with that obtained by feko.

2.3.2 Antenna Array Synthesis based on FT

Indeed, FT can be helpful in antenna synthesis. Both the array factor (AF) and space factor (SF) can be understood as pairs of Fourier Transforms. However, it's important to note that AF is defined for an array composed of discrete units, while SF is defined for a continuous source. Mathematically, the main difference between AF and SF lies in the operations used: AF involves summation while SF involves integration.

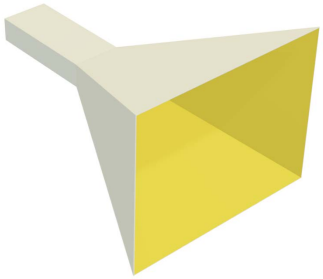

(a)

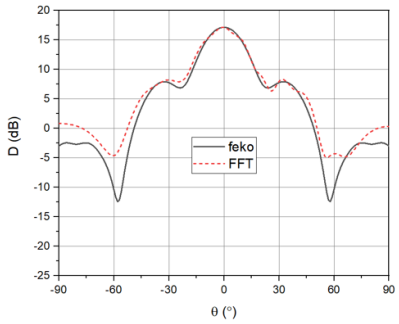

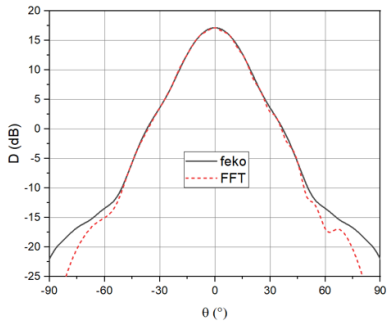

(b) (c)

Figure 2.1: (a) The standard horn operating at 1.645 GHz, (b) directivity pattern at E-plane, (c) directivity pattern at H-plane.

The radiation pattern for an antenna carrying a certain electric current is defined as follows [28].

$$\vec{E}_{\infty}(\hat{u}_r) = -\frac{jk\eta}{4\pi}\int_{V_0}\left[\vec{J} - \left(\vec{J}\cdot\hat{u}_r\right)\hat{u}_r\right]e^{jk\hat{u}_r\cdot\vec{r}'}dV\left(\vec{r}'\right) \tag{2.3}$$

where $\hat{u}_r$ represents the unit vector for the observation. While the SF can be defined as follows [27].

$$SF(\hat{u}_r) = \int_{V_0} I\left(\vec{r}'\right)e^{jk\hat{u}_r\cdot\vec{r}'}dV\left(\vec{r}'\right) \tag{2.4}$$

SF and the radiation pattern share similarities in their representation, including the $e^{jk\hat{u}_r\cdot\vec{r}'}$ term representing the phase introduced by the observation. SF solely considers the magnitude and phase of the field, while the radiation pattern incorporates polarization information.

Specifically, for a linear continuous source along x-axis, the space factor (SF) can be

defined as follows:

$$SF(\zeta) = \int_{-\infty}^{+\infty} I\left(x'\right) e^{j\zeta x'} dx' \tag{2.5}$$

where $\zeta = k\hat{u}_r \cdot \hat{u}_x = k\sin\theta$, and θ represents the angle off the normal direction of the linear array. This parameter is defined to simplify the form of the intergral.

Therefore, the FT pair can be defined.

$$I(x) = \frac{1}{2\pi} \int_{-\infty}^{+\infty} SF\left(\zeta'\right) e^{jx\zeta'} d\zeta' \tag{2.6}$$

According to this (2.6), the source, including the magnitude and phase, can be calculated. As an example, suppose the desired SF is a sector with a width of $2\theta_0$ defined as (2.7).

$$SF(\theta) = \begin{cases} 1 & -\theta_0 \le \theta \le \theta_0 \\ 0 & elsewhere \end{cases} \tag{2.7}$$

The excitation can be obtained in close form.

$$I(x) = \frac{1}{2\pi} \int_{-\infty}^{+\infty} SF(\zeta) e^{jx\zeta'} d\zeta' = \frac{\sin(kx\sin\theta_0)}{\pi x} \tag{2.8}$$

The SF obtained in (2.8) sometimes will be represented using the sinc function. For array synthesis, the discret form of excitation will be utilized, which means the fields will be sampled using unit antenna. It is important to note that in practical scenarios, the Array Factor (AF) often lacks phase information, or in other words, only the magnitude of the expected AF is known. This limitation is common in many real-world applications of antenna arrays.

Let's consider an example with a desired sector width of θ_0=30°. As shown in Figure. 2.2, the distance between the antenna unit is half of the wavelength. When comparing the synthesized AF with the desired AF, it becomes evident that a longer array leads to a smaller error between the expected SF and the realized one. By increasing the length of the array, more unit antennas are included, resulting in a finer sampling of the desired radiation pattern. This increased sampling density allows for better approximation of

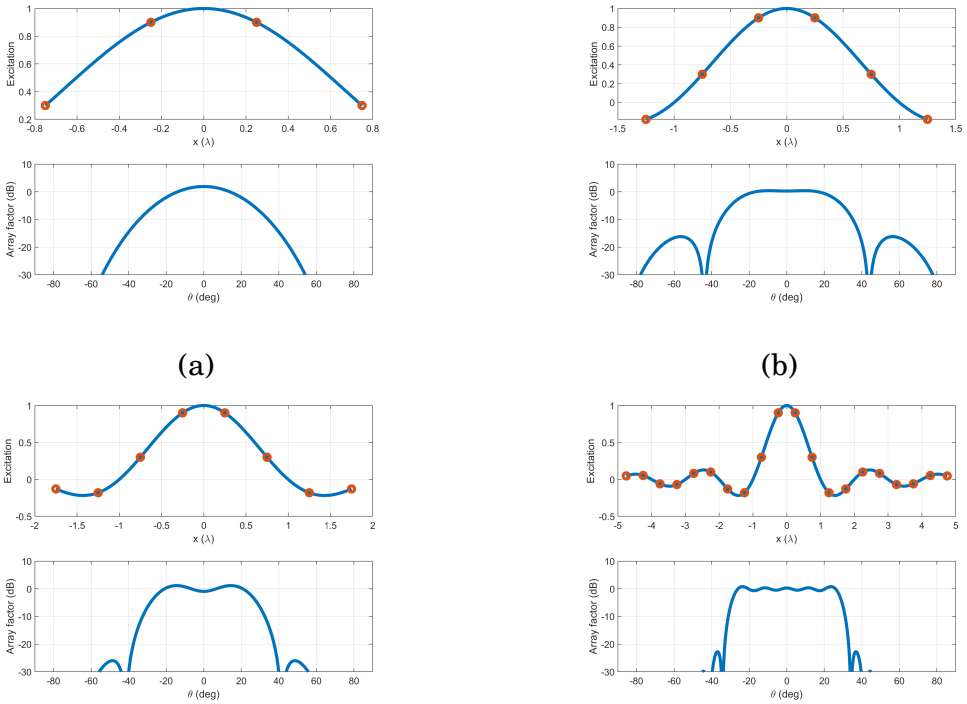

Figure 2.2: FT-based linear array synthesis for a fan-shaped beam. (a) 4 units; (b) 6 units; (c) 8 units; (d) 20 units.

the desired SF within the sector. Consequently, the discrepancy between the expected SF and the realized SF decreases as the array length grows.

However, the application of FT goes beyond this. By using the FT, it becomes possible to transform near fields to far fields, or vice versa, thereby aiding in the synthesis of aperture fields for antennas that exhibit specific far field characteristics. In some antenna synthesis method, such as the intersection approach [29], FT has been used for the feedback for the forward and backward process in the optimization. In subsequent chapters, we will explore how spectrum analysis significantly simplifies the analysis process.

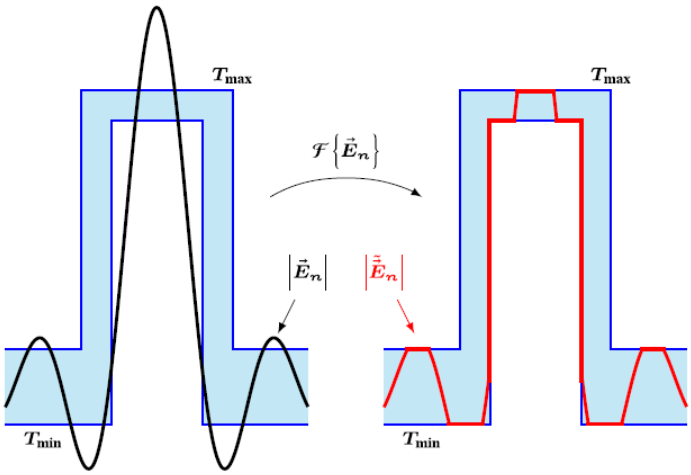

Figure 2.3: Schematic illustration of the operation performed by the forward projection in the classical intersection approach [29].

2.3.3 Evanescent Field Analysis

In a general radiating problem with an impressed source in the source region, the electromagnetic fields extend throughout space. These fields can be classified into two types: propagating fields and evanescent fields [30].

Propagating fields are observed in the far-field region, where they exhibit a radiation pattern characteristic of the source and propagate outward in the form of waves. These fields can be detected at distant points from the source and contribute to the far-field radiation pattern.

On the other hand, evanescent fields are present near the source region and decay exponentially with distance. These fields do not propagate as traditional waves and quickly diminish in magnitude as we move away from the source. Evanescent fields are typically characterized by high spatial frequencies and have limited reach beyond the near-field region.

In most conventional antenna arrays, it is desirable to suppress evanescent fields because they can lead to decreased port isolation and array gain. These fields are

considered unwanted as they do not contribute to the far-field radiation and can introduce unwanted coupling and interference between array elements. Techniques such as proper spacing, decoupling networks, and mutual coupling compensation can be employed to minimize the impact of evanescent fields in array designs.

However, there are certain types of antennas and systems where evanescent fields play a crucial role and need to be intentionally manipulated. One example is a surface wave antenna, which utilizes evanescent fields along the interface to guide and propagate the wave along the surface. In such cases, evanescent fields are harnessed and controlled to achieve the desired antenna performance.

Understanding the behavior and characteristics of evanescent fields is essential for effectively manipulating them in various antenna and wave propagation scenarios, whether to suppress their influence or exploit their unique properties for specific design objectives.

In chapter 4 and 5, we will provide specific examples for the analysis of evanescent fields in surface wave antennas.

2.4 Discussion of MBA in Spectrum Domain

To analyze the coverage of MBAs, it is advantageous to consider it in the u-v plane. The u-v plane provides a useful representation for visualizing and analyzing the coverage of MBAs. For the convenience of those who are not familiar with spectrum analysis for antennas, let's consider an array with beam scanning as an example. Suppose the first beam direction is θ=0°, ϕ=0°, while the second is θ=50°, ϕ=0°. Typically, the performance of the array is observed in a rectangular coordinate system as shown in Figure 2.4(a), with the x-axis representing θ here. However, if we display the directivity patterns in the u-v plane, as shown in Figure. 2.4(b), which represents the visible region of the spectrum domain, we can convey more information in a straightforward manner. The u-v

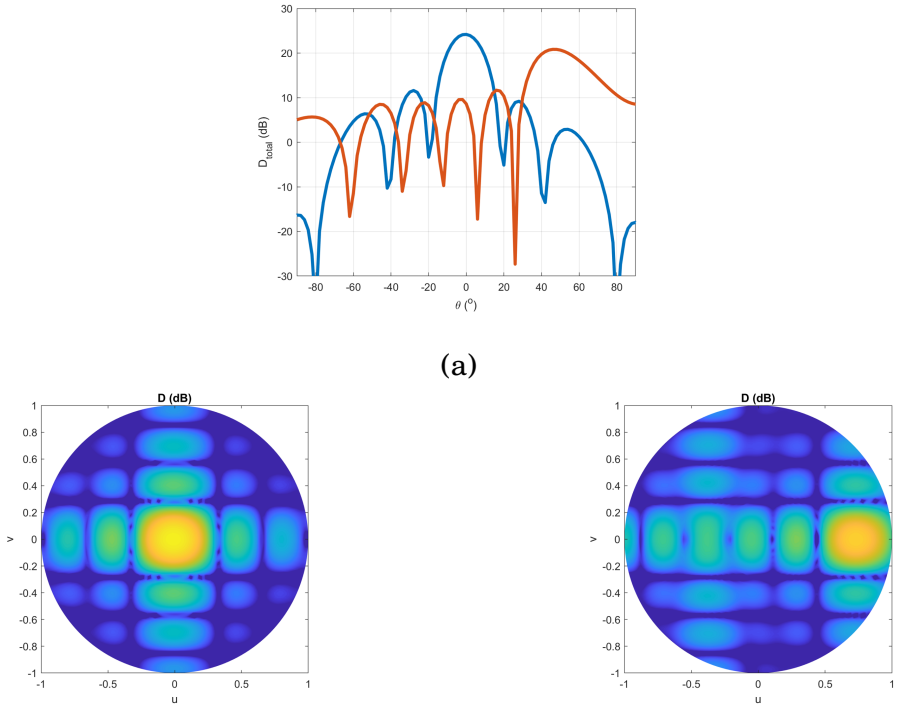

(a)

(b) (c)

Figure 2.4: The directivity patterns of a scanning beam (a) rectangular coordinate, (b) u-v plane for beam 1, (c) u-v plane for beam 2.

plane allows us to visualize the coverage and characteristics of the array's beams more effectively. The relationship between the spherical coordinate system with u-v plane is simple as u=sinθcosϕ and v=sinθsinϕ.

In scenarios where MBAs are employed to achieve beam scanning, one of the primary considerations is the coverage of the beams. Let's explore two different approaches to coverage: Firstly, as shown in Figure. 2.5(a), let's consider the utilization of MBAs with fan-shaped beams. This configuration offers a coverage pattern where the beams resemble a fan shape. By exciting the antenna units in a coordinated manner, the beams can be directed to cover specific directions of interest simultaneously. This approach allows for targeted coverage in multiple directions by adjusting the excitation of the antenna elements. The fan-shaped beams provide flexibility in beam steering and enable coverage of desired directions by appropriately controlling the phase and amplitude of

(a) (b)

Figure 2.5: The schematic diagram of coverage for MBA (a) Fan-shaped beam, (b) conical beam.

the individual elements. Secondly, as shown in Figure. 2.5(b), in the case of MBA with conical beams, each MBA covers multiple directions using narrow conical beams. By exciting different antenna units with proper phase, similar to a phased array, beam scanning can be achieved.

In addition to coverage considerations, the dimension of the array can be estimated based on the relationship between the spatial domain and spectral domain. This relationship can be understood through the FT. For example, a large array consisting of multiple small antenna with different distance between each unit are shown in Figure. 2.6. Large distance between the units in spatial domain means small distance between grating lobes in spectrum domain.

2.5 Chapter Summary

This chapter provides an overview of spectrum analysis in antenna analysis and design. We compare parameters for time-varying and space-varying properties and explore their applications. Examples of the applications of spectrum techniques are also discussed. The straightforward applications in MBA design will be given in sequent chapters.

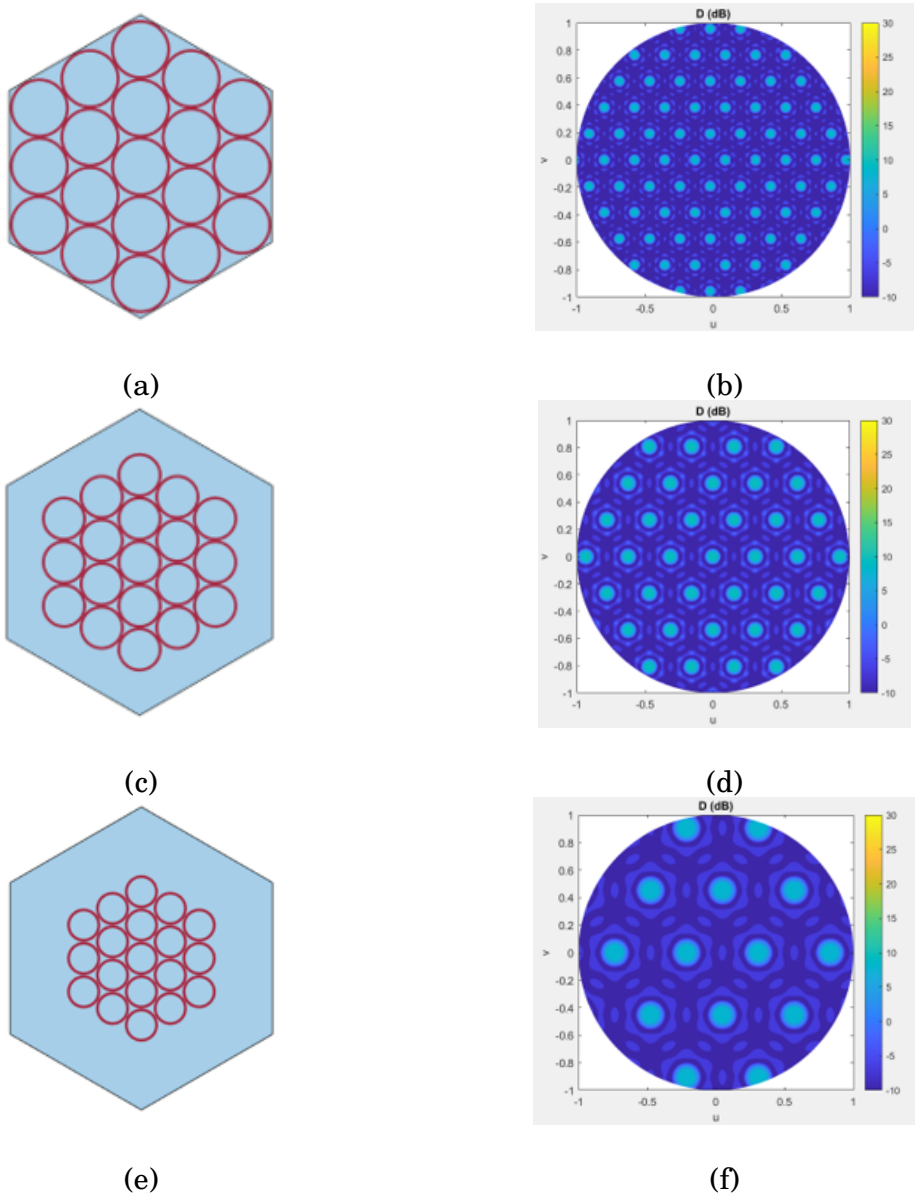

Figure 2.6: The schematic diagram of antenna unit and the array factors in u-v plane.(a), (c) and (e) are the array with the distance between each unit to be 5λ, 3.5λ, 2λ, (b), (d) and (f) are the corresponding array factors.

CHAPTER 3

CIRCULAR ARRAY WITH 360° AZIMUTHAL BEAM SCANNING

3.1 Chapter Introduction

In this chapter, the well-known fact that the beam generated by a monopole antenna mounted on a finite ground plane becomes elevated because of the currents it induces on it was considered [31]. It was demonstrated that by inserting resonant slot structures into the ground plane, this undesirable effect can be suppressed. Monopole-based Yagi-Uda antennas were then developed that have their main beams directed at their endfire direction along the horizontal plane with a realized gain improvement. A circular array of these monopole-based Yagi-Uda antennas was also designed and simulated. By exciting different sectors formed by sets of these Yagi-Uda antennas, full azimuthal beam scanning was achieved. Measurements of a prototype sector of this array confirmed the efficacy of the overall design process. It is anticipated that this innovative circular array with its high realized gain and its ability to have its beam scanned to provide a full 360°

coverage of the azimuthal plane will be of practical interest since it can provide multicell coverage to manage the extreme traffic density in many wireless ecosystems.

Beam scanning or multi-beam antennas that provide a 360° full azimuthal coverage have attracted more and more attention because they have applications in a wide variety of electronic systems, e.g.,cognitive radios, direction-of-arrival estimation and cellular base stations. Beam scanning antennas can serve multiple users at different times by dynamically changing the directions at which their beams point. Multi-beam arrays that are fed by multiple ports can provide multiple concurrent, yet independent beams to enable multipoint-to-multi-point communications.

A general method to achieve beam scanning with a full 360° azimuthal coverage is to employ a circular antenna array with a reconfigurable feed network which has multiple input ports. These antennas can radiate a single beam by energizing one port or multiple beams by exciting multiple ports simultaneously. By activating different sectors of a circular array, beams can be radiated towards a particular set of directions. A full 360° azimuthal coverage has been achieved in several reported systems. For instance, an eight-port fed, tightly coupled slot antenna array was presented in [32] that achieved a maximum gain of 5.2 dBi in its endfire direction. A six-element circular patch array was developed in [33] that achieved a maximum gain of 8.45 dBi. A four-element dipole array was presented in [34] that had a maximum gain of 5.4 dBi. A six-element dipole circular array was developed in [35] that had a maximum gain of 3.12 dBi.

Electronically steerable parasitic array radiators (ESPARs) [36–41] and active frequency-selective surface [42–44] based arrays are also capable of a full 360° coverage of the azimuthal plane. The ESPAR is a classic antenna that was developed to facilitate beam scanning along the azimuthal plane. Some of the original key concepts and interesting designs are discussed in [36]. A circular array of monopoles with both active and passive elements was proposed in [38]. A dual-band ESPAR was presented in [39]. However,

these types of antennas are less flexible. Because they have only one driven radiator, they can only achieve a single steered beam rather than being able to radiate multiple beams.

It is found that all of these beam scanning and multi-beam arrays have achieved a realized gain that is below 10 dBi. This limitation is mainly attributed to the fact that the radiator associated with each beam is either a single slot/patch/dipole or a small array of them. An interesting method to achieve a full 360° azimuthal coverage with a high gain is to use an array driven with multipole ports to excite a high-impedance surface or metasurface. The high-impedance surface developed in [3] was arranged into four sectors and fed with 28 ports. Each sector produced a steered beam within its 90° quadrant and attained a maximum measured gain of 16 dBi. Furthermore, a single-layered annular surface plasmon polariton -based leakywave antenna was developed in [45] that provided a 270° scanning over the azimuthal plane with a maximum gain of 19.7 dBi. The beam scanning was achieved by sweeping the operating frequency. However, the main beam direction was elevated to 46° above the azimuthal plane.

A monopole-based Yagi-Uda circular array is a very simple technology that can achieve a full 360° azimuthal scan with a high gain [46]. However, the main beam direction of the array with its finite-sized ground plane is also elevated above it as a consequence of the fields radiated by the non-trivial currents existing on its edges [37, 47]. This is usually undesirable since it reduces the terrestrial coverage. This disadvantage limits the applications of such arrays. A very early design that used a resonant slot in a flange attached to the ground plane in order to modify the radiation pattern of a Yagi-Uda linear array was introduced in [48]. The purpose of the slot was to remove an interference null by suppressing the foreground reflection. Recently, one way to enhance the endfire performance characteristics of a monopole-based array is to employ a skirted ground structure [37]. The height of the skirt affects the main beam direction. A skirt

that is nearly a quarter wavelength in height will enable the beam to be pointed along the horizontal direction. Nevertheless, the size of the ground plane in the design is half a wavelength. Moreover, the feasibility of this method on a large ground plane was not considered. Another way is to place a reflector on top of the monopole antenna to make the beam directed towards the endfire direction, but the profile of the antenna becomes much higher [47].

In this chapter, we report the development of an innovative monopole-based Yagi-Uda endfire antenna. Resonant slots are inserted into its ground plane; they mitigate the fields radiated by it. This configuration enables endfire beams which are radiated along the horizontal plane. Furthermore, a full 360° azimuthal scanning is achieved with a maximum realized gain over 12 dBi by forming a circular array with 18 of these endfire antennas. It is noted that a planar microstrip Yagi-Uda antenna [49, 50] can also achieve endfire performance along the azimuthal plane. However, because the driven dipole is printed on the azimuthal plane and is a half wavelength long, a circular array of planar microstrip Yagi-Uda antennas will have less beam resolution than a compact monopole array, whose radiators are perpendicular to it.

3.2 Monopole Antenna With An Endfire Radiation

It is well known that if a monopole is mounted perpendicular to an infinite ground plane, it will radiate an omnidirectional pattern whose maximum direction is along that horizontal plane. However, if the ground plane is finite in size, the main beam direction will be substantially elevated above that horizontal plane. This negative feature is mainly due to the fields radiated by the currents that the monopole fields induce on the ground plane. We have developed a finite-sized monopole-based antenna whose maximum beam direction is along the horizontal plane.

The configurations of the reference (Ref.) monopole antenna and our innovative

design are shown in Figure. 3.1(a) and (b), respectively. The differences between the two systems are the four resonant slots etched in the ground plane in Figure. 3.1(b); they are more clearly detailed in Figure. 3.1(c). The length of the slot is 0.42 λ_0, λ_0 being the free space wavelength of the operating frequency. The width of the slot is 0.015 λ_0. The four slots are not connected end to end. There is a small gap, 0.0075 λ_0 wide, between the ends of each slot. The length of the monopole in both systems is $\lambda_0/4$. The length and the width of the ground plane of both antennas are selected to be λ_0 simply for comparison purposes. It will be shown later that this resonant slot method is suitable to any finite-sized ground plane. Note that arc shaped slots are also capable of eliminating the current on the ground and redirecting the beam to the horizontal direction. The rectangular slots were chosen for our design and prototype simply because they were the easiest ones to fabricate. We first present the currents of these two monopoles in order to show the effects of the slots on the radiation patterns of the monopole alone. Those of the bare monopole are given in Figure. 3.2(a); those of the monopole with the slots are given in Figure. 3.2(b). They were obtained using feko.

The currents on the edges and a majority of the ground plane when the slots are present in Figure. 3.2(b) are significantly smaller than those in Figure. 3.2(a) when they are not. As a consequence, the fields radiated from the ground plane are significantly reduced when the slots are present. Thus, there are minimal additional fields impacting those of the monopole, which facilitates the overall fields being radiated along the horizontal direction. It must be noted that there are strong currents around the resonant slot structures. However, as indicated by their directions (black arrows), the currents near the slots essentially cancel each other. There are no field components from them to elevate the pattern off from the horizontal plane on which they lie. The resonant slot structures also act to minimize the currents on the ground plane away from the slots as shown in Figure. 3.2(b). Therefore, a larger ground plane will not lead to fields that

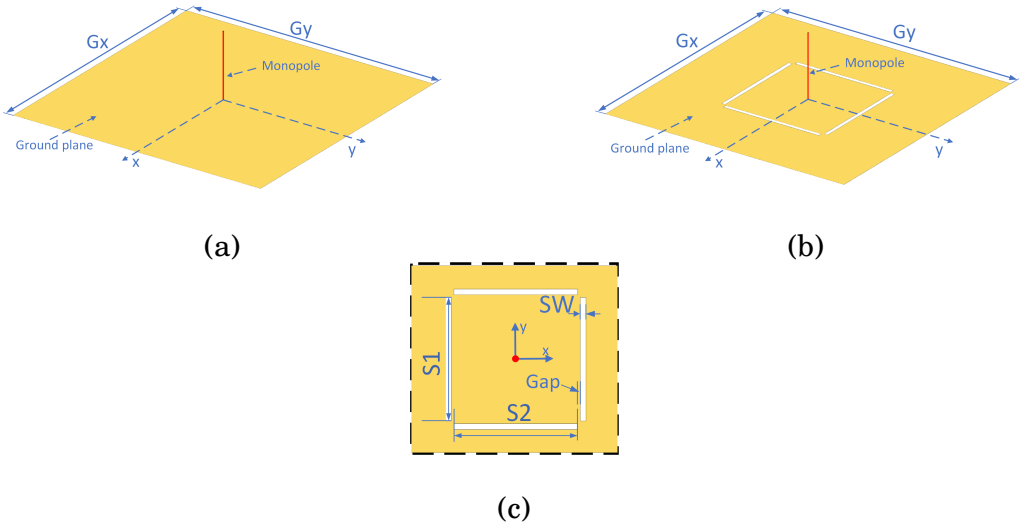

Figure 3.1: Monopole-based antennas. Isometric view of the (a) Ref. monopole and (b) the monopole with the slots. (c) Top view of the slots in (b). The lengths of the ground plane along the x- and y- axes are denoted by Gx and Gy, respectively. The slot length S1 = S2 = $0.42\lambda_0$, slot width SW = $0.015\lambda_0$ and slot Gap = $0.0075\lambda_0$.

would lift the monopole fields away from the horizontal plane. In fact, the resonant slot structures would also perform a similar function for an arbitrarily shaped ground plane.

When one dimension of the ground plane is reduced small enough, the slots perpendicular to this direction are not needed. For example,when the width of the ground plane Gy is reduced to $0.5\lambda_0$, the slots along the x-axis are not required because the currents on the ground plane away from the y-directed slots are small. The length of the remaining slots was optimized to be $0.49\lambda_0$ to minimize the fields radiated from the ground plane. The overall current distribution is shown in Figure. 3.2(d). In contrast, the current distribution of the Ref. monopole antenna with this reduced-size ground plane is given in Figure. 3.2(c). Comparing Figures. 3.2(c) and 3.2(d), the currents on the ground plane along the x-axis have indeed been reduced significantly for the monopole with slots. Moreover, the currents around the slots still cancel each other.

The radiation patterns of these Ref. monopole and monopole with slots cases are presented in Figure. 3.3. The peaks of the Ref. monopole cases are clearly elevated substantially above their ground planes. In contrast, the monopole cases with the slots have

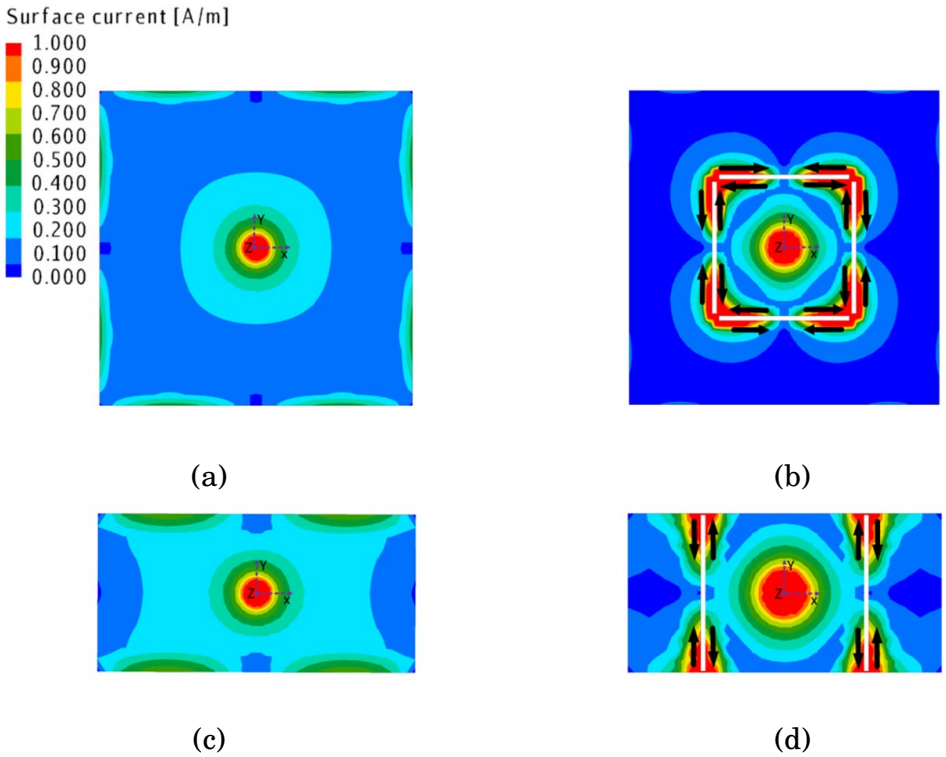

Figure 3.2: Magnitude of the currents on the ground for the Ref. monopole and the monopole with slots. Gx=λ_0. (a), (b): Gy=λ_0. (c), (d): Gy=0.5λ_0.

their radiation peaks along the horizontal direction. These results clearly demonstrate that by inserting resonant slots into the ground plane near the monopole, the fields radiated by the ground plane are reduced significantly and the peaks of the antenna,Äôs overall radiation pattern become horizontally directed.

From the analysis based on spherical vector wavefunctions (SVWF), it is shown that the elevated angle arises from higher order TM modes from the ground plane. By inserting resonance structures, i.e., slots, in the ground plane, a dipole-like (TM_{01} mode dominated) radiation can be achieved as shown in Figure. 3.4. SVWF is utilized to analyze the antenna. For SVWF, the power radiated by outcoming modes is one half of the summation of squares of coefficient magnitudes. This means that the percentage of radiated power of every mode can be calculated respectively, considering the orthogonality of SVWF [51]. For the antenna here, only TM_{01} mode from the monopole and TM_{mn}

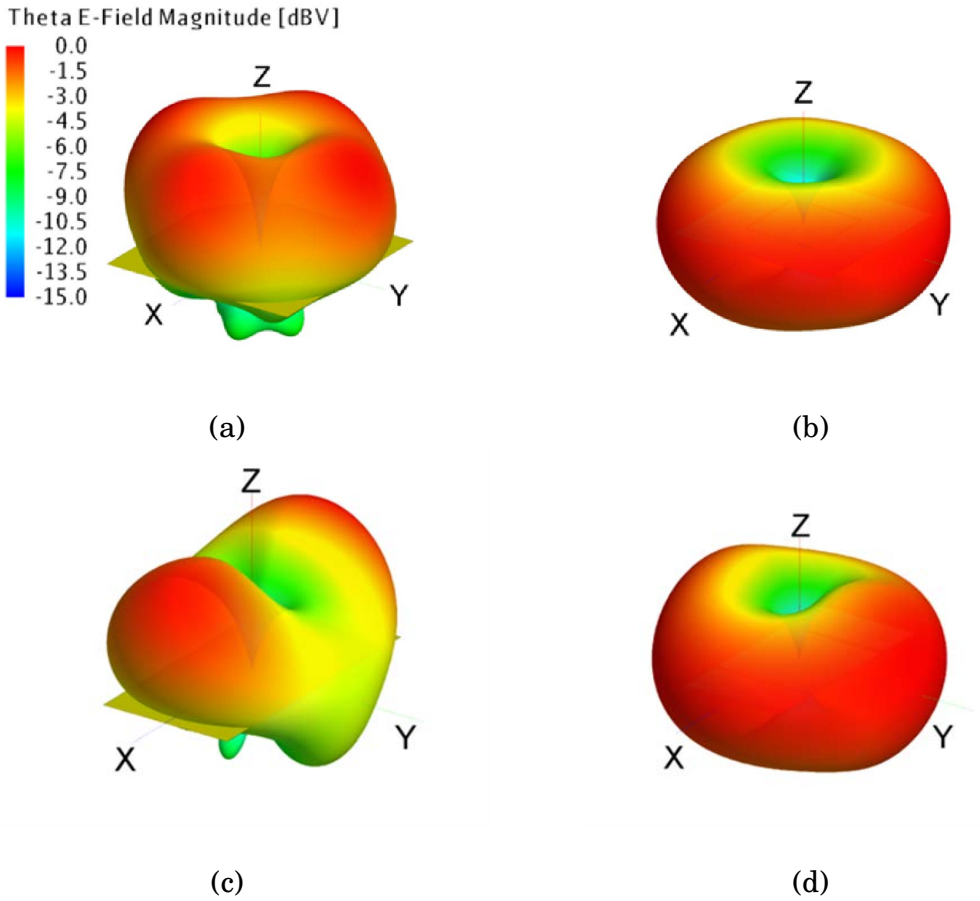

Figure 3.3: Radiation patterns of the Ref. monopole and the monopole with slots. (a): Ref. case, Gx=λ_0, Gy=λ_0. (b): Slot case, Gx=λ_0, Gy=λ_0. (c): Ref. case, Gx=λ_0, Gy=0.5λ_0. Slot case, Gx=λ_0, Gy=0.5λ_0.

(n=odd) from the ground plane are necessary. For spherical coordinate system, TM_{mn} means there are m cycles in H-plane and n cycles in E-plane.

In Figure. 3.4, the dimension of the modified monopole is shown. The reference one is with the same dimension and only difference is that there is no slots in the ground. The percentages of radiated power from the first two TM modes are compared in Figure. 3.4. It is obvious that by inserting slots in the ground plane, the radiated power from TM_{01} mode will dominate (over 90%) and the TM_{02} mode, which is the most significant higher order mode from the ground, will be suppressed (below 10%).

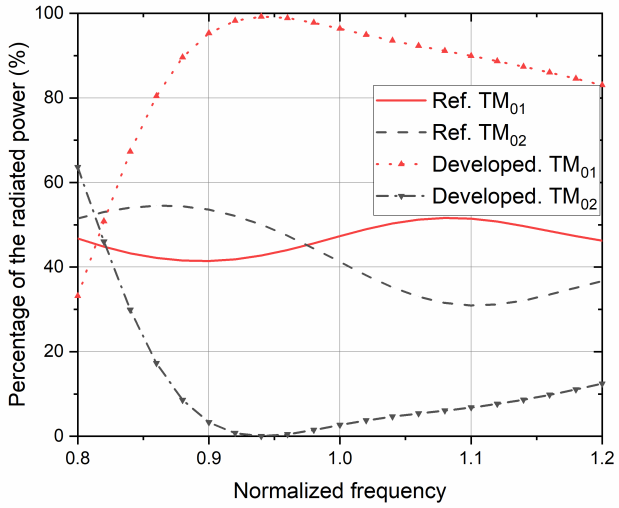

Figure 3.4: Percentage of the radiated power from different TM modes.

3.3 Monopole-Based Yagi-Uda Antenna With Slots

Based on the developed monopole antenna with its slot structures, we have designed a monopole-based Yagi-Uda antenna whose main beam is pointed along its endfire direction. A typical Yagi-Uda antenna with no ground plane consists of a reflector, a driven dipole and several directors. It radiates an endfire beam. On the other hand, a monopole-based Yagi-Uda antenna without any slot structures radiates an elevated main beam. We employ the resonant slot approach developed for the single monopole antenna to suppress the fields radiated by the ground plane in the array version. Since the standard Yagi-Uda antenna has a directive beam with a very small backlobe, only one resonant slot per element is actually needed to implement the strategy instead of four surrounding each monopole.

Three monopole-based Yagi-Uda antennas are shown in Figure. 3.5. Each has its array oriented along the x-axis. The lengths of all of their elements are selected to have their main beam be pointed along the +x-axis at 3 GHz [27]. The antenna in Figure. 3.5(a) is the Ref. case without any slots. The antenna in Figure. 3.5(b) is the rectangular

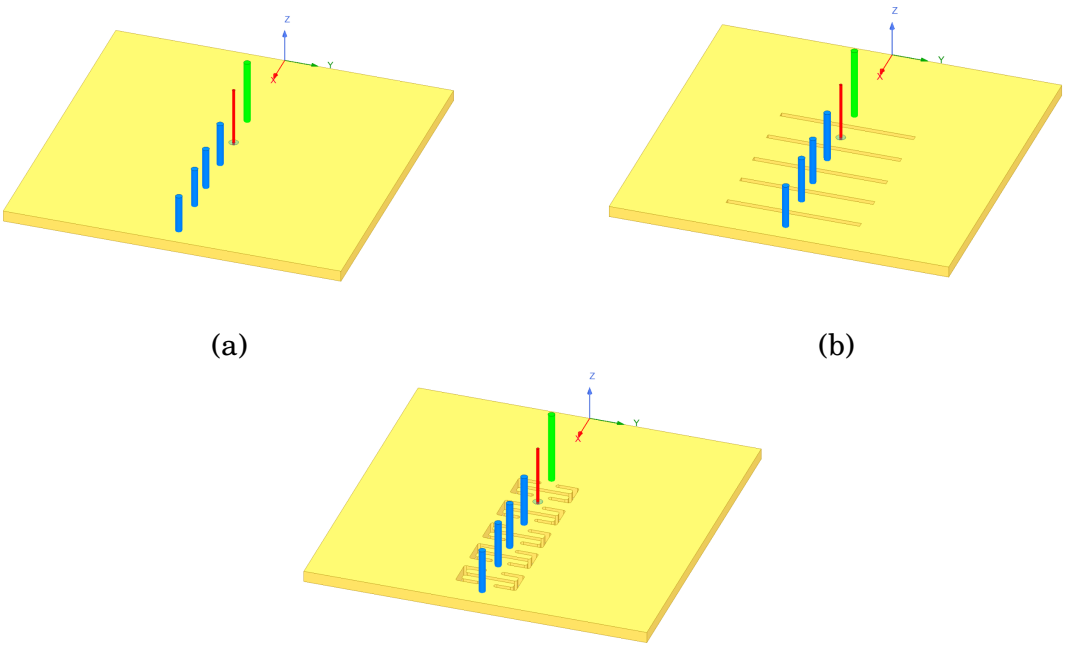

(a) (b)

(c)

Figure 3.5: Monopole based Yagi-Uda antennas with a square ground plane.

slot (RS) version of modified Yagi-Uda antenna, and Figure. 3.5(c) is the Ishaped slot (IS) version.

The optimized parameters of the array design are illustrated in Figure. 3.6(a). The slots of the two cases are presented in Figure. 3.6(a) and (b). The slots of the two cases are presented in Figure. 5 (a) and (b). The dimensions of each parameter are given in the caption of Figure. 3.6. The radius of the cross section of reflectors and directors are 1.5 millimeter (mm), while it is 0.65 mm for the driver, which is fabricated by extending the inner conductor of the coaxial line. The resonant rectangular slots in Figure. 3.5(b) and 3.6(a) are $0.59\lambda_0$ long. The resonant I-shaped slots in Figure. 3.5(c) and 3.6(b) are much smaller, being only $0.265\lambda_0$ long.

These three monopole-based Yagi-Uda antennas were simulated using the commercial software-ANSYS Electromagnetics Suite (HFSS), version 19. Their simulated realized gain patterns at 3.0 GHz and their maximum realized gains as a function of the source

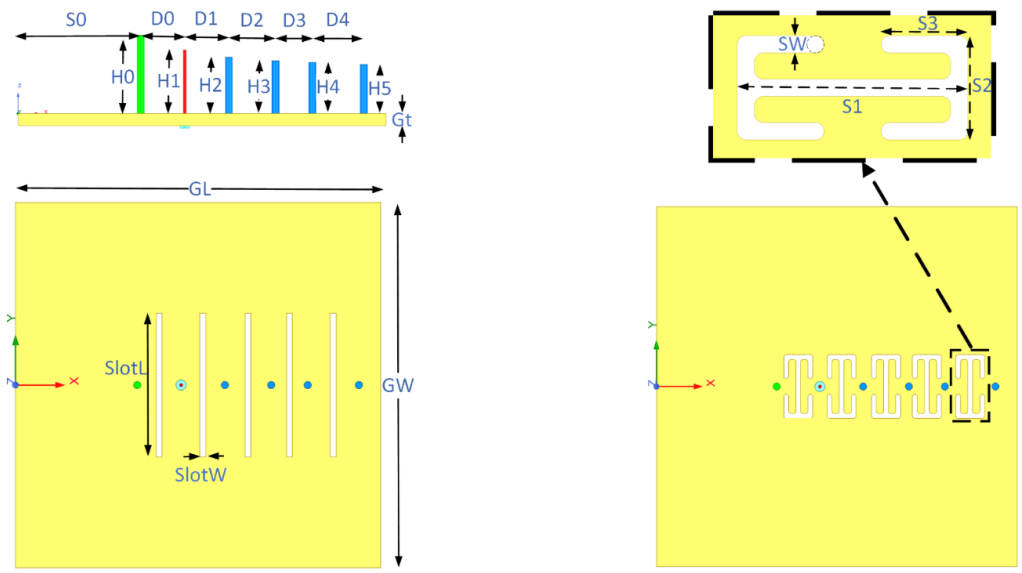

(a) (b)

Figure 3.6: Monopole-based Yagi-Uda antennas having slots in their ground planes. Optimized design parameters (Dimensions in mm): Shared values: GL=150, GW=150, Gt=5, S0=50, D0=18, D1=18, D2=19, D3=15, D4=21, D5=21. Ref. Yagi-Uda Antenna: H0=29, H1=26, H2=20, H3=19, H4=18, H5=17. RS version: H0=32, H1=26, H2=23, H3=21.5, H4=21, H5=20, SlotL=59, SlotW=2. IS version: H0=32, H1=26, H2=23, H3=21.5, H4=21, H5=20, S1=26.5, S2=12, S3=10, SW=2.

frequency are compared in Figure. 3.7(a) and 3.7(b), respectively. It is found in Figure. 3.7(a) that the main beam direction of the Ref. antenna is noticeably elevated around 15° above the ground plane. On the other hand, those of the two slot-based cases are pointed along the +x-axis (θ=90°), i.e., along the horizontal direction. Moreover, both slotbased antennas show an improvement of the maximum gain when compared to the Ref. case of about 3.0 dB at 3.0 GHz.

The resonant I-shaped slots in Fig are much smaller, being only $0.265\lambda_0$ long.These three monopole-based Yagi-Uda antennas were simulated using HFSS, version 19. Their simulated realized gain patterns at 3.0 GHz and their maximum realized gains as a function of the source frequency are compared in Figure. 3.7(a) and (b), respectively. It is found in Figure. 3.7(a) that the main beam direction of the Ref. antenna is noticeably

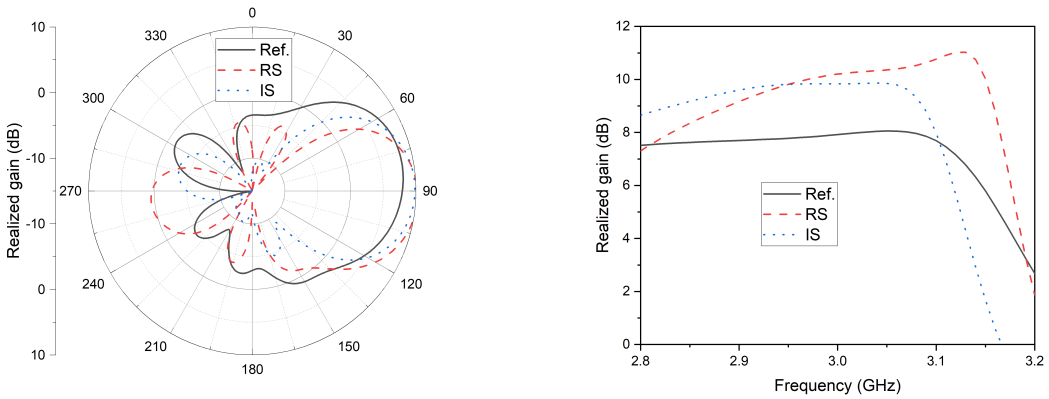

(a) (b)

Figure 3.7: Simulated performance characteristics of all three monopole-based Yagi-Uda antennas with square ground planes. (a) Realized gain patterns in the ϕ=0° (xoz) plane at 3.0 GHz. (b) Realized gain along the endfire direction (+x-axis) as a function of the source frequency.

elevated around 15° above the ground plane. On the other hand, those of the two slot-based cases are pointed along the +x-axis (theta = 90°), i.e., along the horizontal direction. Moreover, both slotbased antennas show an improvement of the maximum gain when compared to the Ref. case of about 3.0 dB at 3.0 GHz.

Because the rectangular slots of the RS version are longer than those of IS version, its radiated beam in Figure. 3.7 is clearly narrower, but its backlobe is larger. Moreover, while Figure. 3.7 shows that it also has a higher peak gain at higher frequencies, nevertheless the RS and IS versions have about the same value at the target frequency 3.0 GHz. The back lobe of the RS version is 1.78 dB larger than that of the Ref. antenna. This feature occurs because the beam generated by the Ref. antenna is tilted with respect to the horizontal plane. Consequently, the back-radiated fields are reflected in the ground, thus reducing the backlobe level. Moreover, the IS version requires considerably less transverse space. Consequently, it will be selected to form the circular array of 18 monopole-based Yagi-Uda antennas (termed units below) with the I-shaped slot structures illustrated in Figure. 3.8.

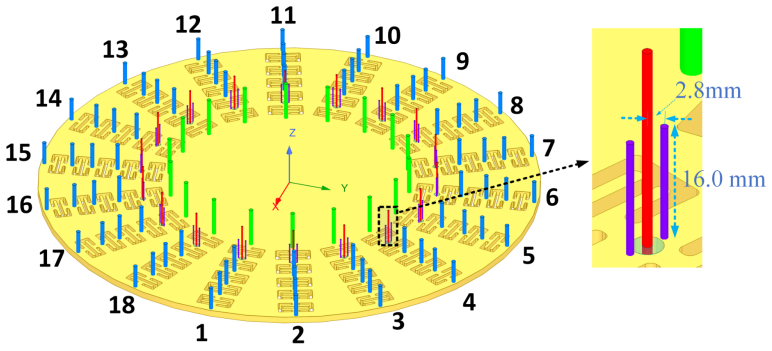

Figure 3.8: Circular array of 18 monopole-based Yagi-Uda antennas with Ishaped slot structures. The diameter of its circular ground disc is 374.0 mm. The angle between any two adjacent elements is 20°.

In summary, analyzing the monopole, it is reasonable to infer that this angle in a Yagi-Uda array is a result of undesired currents on the ground plane, like those in a monopole. Moreover, the mitigation of these undesired currents can be achieved using resonant slots, a technique applicable to monopoles with larger ground planes. Through an examination of a single monopole, we have identified both the cause of the elevated angle and a solution for its suppression.

3.4 Yagi-Uda Array for Full Azimuth Coverage

The ground plane is now circular rather than rectangular. Its diameter is 374.0 mm (3.74 λ_0). The distance between the reflector element and the center of the ground plane is S0 = 90.0 mm, and the angle between the center lines of any two adjacent units is 20°. Two small metallic rods are located beside the driven dipole to improve the impedance matching as illustrated in Figure. 3.8. The distance between each rod and the corresponding driver is 2.8 mm. The height of each rod is 16.0 mm. The main beam of the array can be scanned to cover the full horizontal plane by exciting different Yagi-Uda units. Furthermore, a few Yagi-Uda units forming a sector can be excited together with the same phase to achieve a high gain. The simulated magnitude of the S-parameters

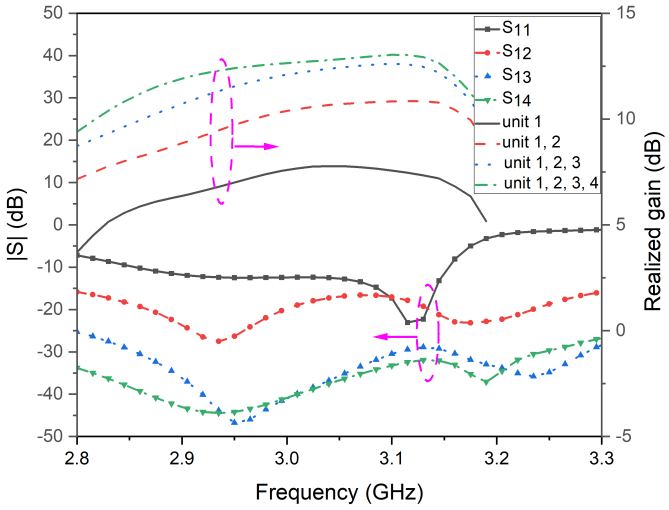

Figure 3.9: Magnitude of the S-parameters and the realized gain values of the circular array as functions of the source frequency and the number of active ports.

and the realized gain values for the array are presented in Figure. 3.9. Because of the symmetry of the array, only the input reflection coefficient of Port 1 is shown along with a comparison of the coupling coefficients between Port 1 and their adjacent ports - Port 2, Port 3, and Port 4. It is clearly seen that the antenna is matched well to its assumed 50 Ω source with $|S_{11}|$ < -10 dB between 2.85 and 3.15 GHz, a 10% fractional bandwidth. The mutual coupling between unit 1 and its adjacent unit - the Yagi-Uda unit excited by Port 2 - is the strongest, but it is less than -15.0 dB over its entire -10.0 dB impedance bandwidth.

The simulated peak realized gain values of the array with different numbers of active units are compared in Figure. 3.9. When more than one unit is active, they are all excited in phase. These curves show that the total realized gain increases across the entire operating band as more elements become active. In fact, the maximum response occurs when unit 1-unit 4 are excited in phase. The peak value of the 4-unit case is 12.5 dBi at 3.0 GHz, which is around 5 dB higher than the single active unit case.

The simulated realized gain patterns of the array with different numbers of active

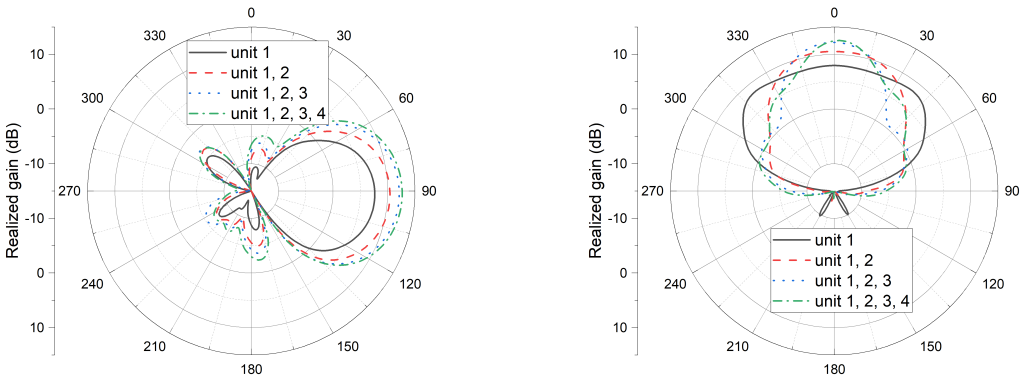

(a) (b)

Figure 3.10: Realized gain patterns of the circular Yagi-Uda array with different number of active elements. (a) E-plane. (b)H-plane.

units are presented in Figure. 3.10 in both the E-plane and the H-plane. The peak of the beam in the E-plane (xoz) of each array in Figure. 3.10(a) is pointed towards the endfire direction, i.e., the beams are no longer elevated. The corresponding realized gain patterns in the H-plane (xoy) are given in Figure. 3.10(b); they have been manually rotated so that the main beam of each case is centered on the x-axis for comparison purposes. The H-plane realized gain patterns of the array with 4 sequential sets of 4 active units are shown in Figure. 3.11 to illustrate its beam scanning ability. The beam directions for each sector are 30°, 50°, 70°, and 90°, respectively. A 20° resolution between the beam directions is thus demonstrated, and the gain drop of the overlapping patterns is below 1.6 dB. Other scanning angles to cover a full azimuth plane can be achieved when other sets of units are excited. The developed system and several reported circular arrays of monopoles are compared in Table. 3.1. It is recognized that in comparison to [37, 39, 41, 47], our circular array of monopoles with a set of resonant slots introduced into its ground between its active and passive elements provides an innovative approach that redirects the main beam to the horizontal direction, facilitates the steering of it in the azimuthal plane, and realizes a higher peak realized gain.

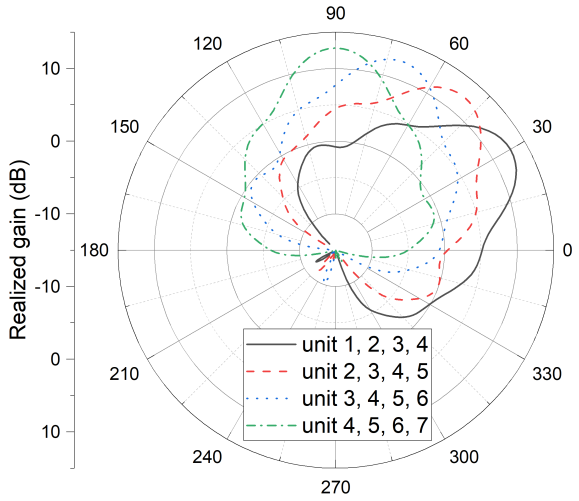

Figure 3.11: Realized gain pattern of the array in the xoy plane when its beam is scanned. 30°: units 1-4; 50°: units 2-5; 70°: units 3-6; and 90°: units 4-7.

Due to a limited budget, we only fabricated a 60° sector of the whole array, i.e., three Yagi-Uda units, to verify the validity of the developed method. The prototype is shown in Figure. 3.14. The dimensions of the Yagi-Uda array units are the same as those in Figure. 3.6 for the IS case. The unit excited by Port 1 is our focus as it has two adjacent elements. This configuration can mimic the units in the whole circular array in Figure. 3.8. The slots are etched in a 5.0 mm thick, fan-shaped aluminum plate. A 1.0 mm thick solid sector, which has the same shape as the slot-based one, is placed 0.3 λ_0 below the antenna and is grounded. The reflectors and drivers are threaded on the floor from the top of the ground to the bottom. A requisite pair of copper rods was soldered beside each of the driven dipoles. The two plates are supported by 4 Nelon posts. The radius of the inner arc Rin is 55.0 mm; the distance from the edge of the sector to the nearest element axis line S is 25.0 mm. This mechanically stable configuration greatly simplified the measurement setup.

The simulated and measured S-parameters are shown in Figure. 3.13. When Port 1 is excited, the other two ports were loaded with a 50 Ω matched impedance. It can

Table 3.1: Performance Comparison of Circular Arrays of Monopoles

Ref.	Number of passive units in the circular array	Freq. (GHz)	Peak realized gain of beam (dBi)	Main beam direction in the E-plane	Method to suppress the undesired currents on the ground
[37]	5	1.575	6.4	horizontal	Skirted ground
[39]	5	0.9/1.9	2.8/4.0	horizontal	Infinite ground
[41]	6	2.4	8.08	9.7° above the ground plane	Skirted ground
[47]	18	2.45	10.0	horizontal	Reflector on top of the array
This work	18	3.0	12.5	horizontal	Ground with resonant slots

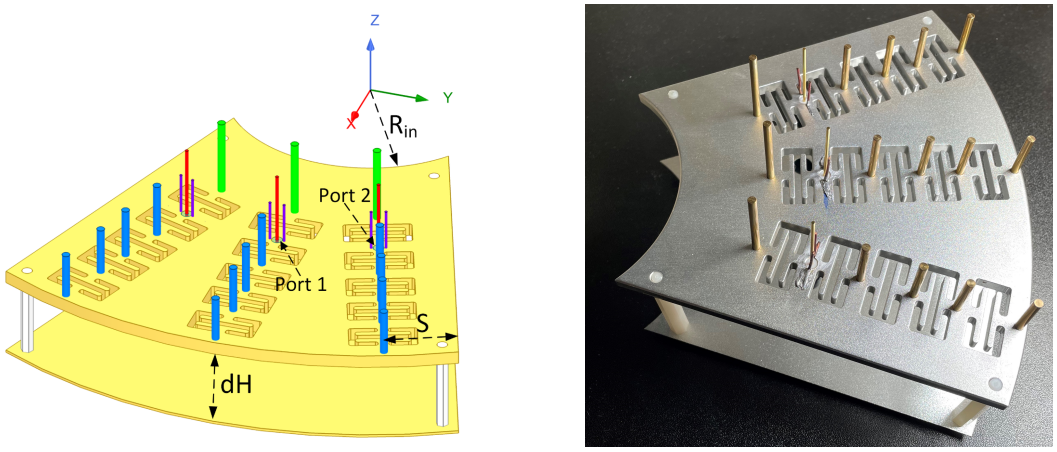

(a) (b)

Figure 3.12: Prototype 60° sector of the circular Yagi-Uda array. (a) Model. (b) Photo of the prototype. S = 25.0 mm, R_{in}=55.0 mm, dH=30.0 mm.

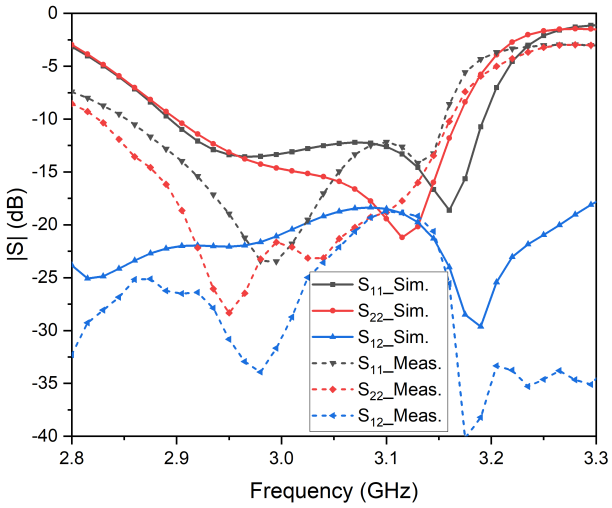

Figure 3.13: Simulated and measured S-parameters of the prototype sector.

be seen that the simulated input reflection coefficients are below -10 dB from 2.9 to 3.15 GHz, and the measured results are below -10.0 dB across this frequency band. The mutual coupling is less than -18.0 dB over the entire band for the simulated and measured systems. Thus, good agreement between the simulated and measured results is demonstrated.

The simulated and measured realized gain patterns in the E- and H-planes for the prototype at different frequencies are compared in Figure. 3.14. Only vertical polarization components are shown in the figures because of the high polarization purity of the monopole antenna. The cross-polarized values are too small to be included on the given scale. Overall, good agreement is found in these results and the main beams of the E-plane are pointed in the horizontal direction.

Therefore, the technology developed to re-direct the main beam of a monopole-based Yagi-Uda array to the horizontal direction is validated. It is noted that the realized gain patterns of the Yagi-Uda unit excited by Port 1 in the prototype sector are slightly different from those of the single unit (unit 1) of the circular array shown in Figure. 3.10.

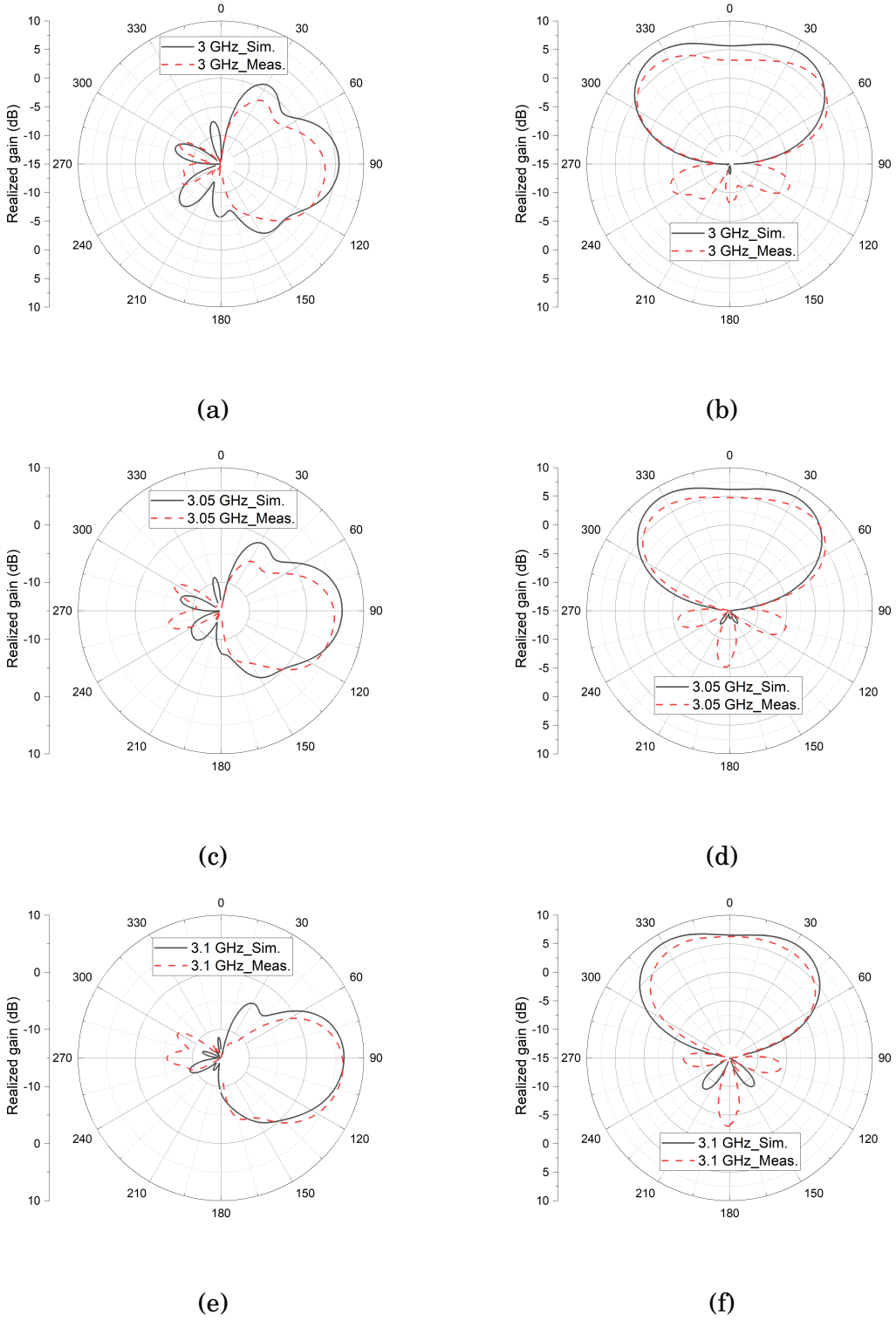

Figure 3.14: Simulated and measured realized gain patterns of the fabricated prototype sector when it is excited by Port 1 at three freqency points. (a) 3.0 GHz, E-plane. (b) 3.0 GHz, H-plane. (c) 3.05 GHz, E-plane. (d) 3.05 GHz, H-plane. (e) 3.1 GHz, E-plane. (f) 3.1 GHz, H-plane.

These differences occur because the dimensions of the three fabricated units of the sector were optimized in regards to the entire circular array environment, not just as a single unit. The measured radiation patterns have larger backlobe levels than the simulated ones do. This difference is attributed to inaccuracies in the distance of the antenna from the additional conducting plate that had to be introduced for mounting the antenna in the measurement chamber. Stray currents excited on the long cables present in the measurements also contributed to this difference.

3.5 Chapter Summary

The well-known fact that the beam generated by a monopole antenna mounted on a finite ground plane becomes elevated because of the currents it induces on the ground plane was considered. It was demonstrated that by inserting resonant slot structures into the ground plane, this undesirable effect can be suppressed. Monopole-based Yagi-Uda antennas were then developed that have their main beams directed at their endfire direction along the horizontal plane with a realized gain improvement. A circular array of these monopole-based Yagi-Uda antennas was also designed and simulated. By exciting different sectors formed by sets of these Yagi-Uda antennas, full azimuthal beam scanning was achieved. Measurements of a prototype sector of this array confirmed the efficacy of the overall design process. It is anticipated that this innovative circular array with its high realized gain and its ability to have its beam scanned to provide a full 360° coverage of the azimuthal plane will be of practical interest since it can provide multicell coverage to manage the extreme traffic density in many wireless ecosystems.

CHAPTER 4

MODELLING OF METASURFACES

4.1 Chapter Introduction

In this chapter, the most significant formulas for metasurface modeling will be reviewed to provide a clear insight into metasurface design. The general sheet transition conditions (GSTCs) as well as the impedance boundary conditions (IBCs) will be listed here. The relationship between these two conditions will be highlighted, followed by a detailed explanation of the IBCs themselves. This information will be particularly useful for surface wave antenna design based on MTS. Furthermore, the surface wave antenna based on MTS will be discussed in next subsection, including single beam antenna design and subarray-based MBA design.

To design compact MBAs, it is essential to analyze the basic concepts behind MTS, such as GSTCs and IBCs. Understanding these principles enables the development of compact antenna designs that are based on a solid foundation. By leveraging the GSTCs and IBCs, it becomes possible to manipulate the behavior of electromagnetic waves at

the MTS interface. These conditions provide guidelines for controlling the transmission, reflection, and absorption of electromagnetic waves, allowing for the design of antennas with unique properties and functionalities.

Applying the principles of GSTCs and IBCs in antenna design can lead to compact configurations that offer improved performance in terms of size, bandwidth, efficiency, and radiation characteristics. By harnessing the capabilities of metasurfaces, it becomes feasible to achieve miniaturization and integration of antennas without compromising their overall performance.

In summary, the analysis of the basic concepts of MTS, including GSTCs and IBCs, serves as a foundation for proposing compact antenna designs. This knowledge empowers engineers and researchers to explore innovative approaches in developing efficient and space-saving MBAs.

4.2 GSTCs

GSTCs are crucial boundary conditions used for modeling MTS, including both isolated particles and fishnet structures. They play a vital role in characterizing the field discontinuities that may arise in the presence of a MTS with an infinite transverse dimension.

The field discontinuities across the MTS can be described using electric currents and magnetic currents. In [52], the MTS has been modeled as a surface with non-zero thickness. Consequently, both transverse and normal components of the electric currents and magnetic currents have been taken into account and are included in the final boundary conditions. In [53], the history of GSTCs has been reviewed, and the general form of them have been given.

The main objective of deriving GSTCs is to model the fields on both sides of the MTS using intrinsic parameters of the surface. During the derivation, the commonly

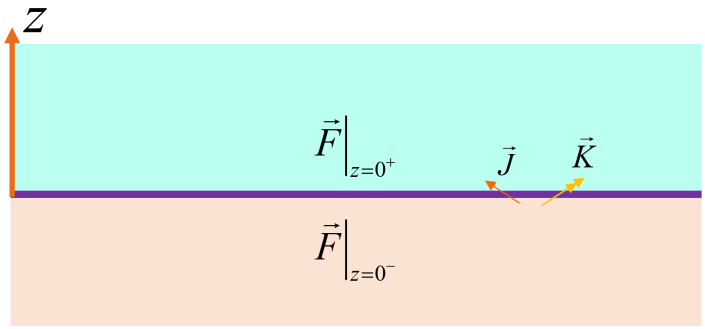

Figure 4.1: The configuration of the fields and interface of the MTS.

used discrete dipole approximation (DDA) has been applied to determine the surface electric polarization and magnetization densities. In [54], the GSTCs has been obtained. Although the GSTCs with both transversal and normal electric currents and magnetic currents have been given in [53], we will consider the ones without normal currents, which is sufficient for practice where the MTS can be modeled as thin surface.

$$\begin{cases} \hat{z} \times \Delta\vec{E} = -j\omega\mu_0 \overline{\overline{\chi}}_{mm} \cdot \vec{H}_{t,av} - j\omega\sqrt{\epsilon_0\mu_0}\,\overline{\overline{\chi}}_{me} \cdot \vec{E}_{t,av} \\ \hat{z} \times \Delta\vec{H} = j\omega\sqrt{\epsilon_0\mu_0}\,\overline{\overline{\chi}}_{em} \cdot \vec{H}_{t,av} + j\omega\mu_0 \overline{\overline{\chi}}_{ee} \cdot \vec{E}_{t,av} \end{cases} \tag{4.1}$$

where $\overline{\overline{\chi}}$ represents the surface susceptibility, and the subscripts "me", as an example, means the magnetic moments introduced by the local electric fields. The delta field for both $\vec{E}$ and $\vec{H}$ is defined as follows.

$$\Delta\vec{F} = \vec{F}\Big|_{z=0^+} - \vec{F}\Big|_{z=0^-} \tag{4.2}$$

In the case of bianisotropic particles, the electric dipole is influenced by the electric field, while the magnetic field also contributes. Similarly, the magnetic dipole is affected by the magnetic field, with the electric field playing a role as well.

Polarizability is an intrinsic parameter of a single particle, whereas surface susceptibilities account for the effects of the entire array. Therefore, the surface susceptibilities in GSTCs means that the effects from the array of the particles have been well modeled in the equation. Finally, by employing the GSTCs, we can effectively model the field

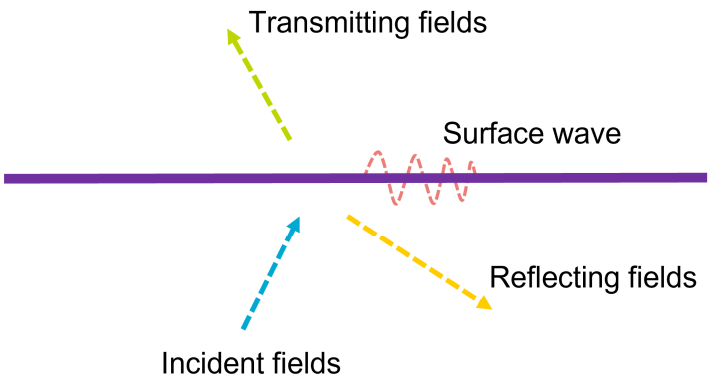

Figure 4.2: The example for the fields associated a MTS.

discontinuities on the interface of the MTS, capturing the behavior and characteristics of the fields.

4.3 IBCs

The IBCs have been developed independently with GSTCs, and has been widely utilzed for modelling the lossy surface in practice, e.g. the soil. IBCs are very useful tools to model the MTS, which connect the tangential components of the fields on the interface of the MTS and the electric and magnetic currents on the MTS.

$$\begin{bmatrix} \vec{E}_t \\ \vec{H}_t \end{bmatrix} = \begin{bmatrix} \overline{\overline{Z}}_{ee} & \overline{\overline{K}}_{em} \\ \overline{\overline{K}}_{me} & \overline{\overline{Y}}_{mm} \end{bmatrix} \begin{bmatrix} \vec{J} \\ \vec{K} \end{bmatrix} \tag{4.3}$$

where $\vec{E}_t$ and $\vec{H}_t$ depict the transversely averaged fields across the MTS. $\vec{J}$ and $\vec{K}$ represent the electric and magnetic currents respectively and they are only the transversal components on the MTS. $\overline{\overline{Z}}_{ee}$ and $\overline{\overline{Y}}_{mm}$ are the surface electric impedance and surface magnetic admittance respectively. $\overline{\overline{K}}_{em}$ and $\overline{\overline{K}}_{me}$ are the magnetoelectric coupling coefficient and the electromagnetic coupling coefficient respectively.

In the rest of this thesis, we will focus on MTS consisting of isolated particles. There are two main types of IBCs for modeling isolated particles in a specific environment [55].

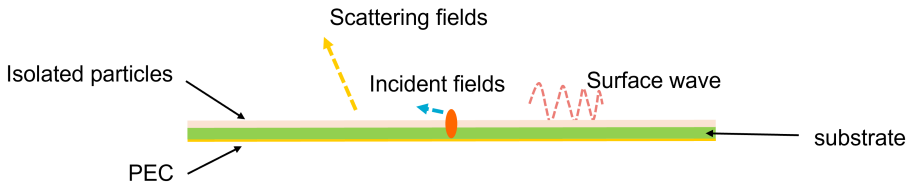

Figure 4.3: A specific case for MTS, which consists of isolated particles and a grounded slab.

The first approach involves modeling both the isolated particles and the environment as a MTS, while the second approach focuses on modeling the isolated particles themselves as a MTS. In the latter approach, the entire structure is modeled using this MTS in the given environment. For instance, consider the scenario where discrete particles are present on a grounded slab. There are two ways to model this system. Firstly, the entire structure can be modeled as an opaque MTS. Alternatively, the particles themselves can be modeled as a transparent MTS, positioned on top of a grounded slab. Clearly, the latter approach is more accurate as it accounts for the well-modeled environment. However, because of its simplicity, the opaque IBC has been widely used.

4.3.1 Opaque IBCs

For opaque IBCs, which has been shown in 4.4(a), the field discontinuities and the average field have very simple relationship given in (4.4) and (4.5). This means that in the opaque IBC, the electric currents and magnetic currents are not independent of each other as given in (4.6).

$$\begin{aligned}\Delta\vec{F} &= \vec{F}\Big|_{z=0^+} - \vec{F}\Big|_{z=0^-} \\ &= \vec{F}\Big|_{z=0^+}\end{aligned} \tag{4.4}$$

$$\begin{aligned}\vec{F}_{av} &= \frac{1}{2}\left(\vec{F}\Big|_{z=0^+} + \vec{F}\Big|_{z=0^-}\right) \\ &= \frac{1}{2}\vec{F}\Big|_{z=0^+}\end{aligned} \tag{4.5}$$

$$\vec{K} = -2\vec{E}_{t,av} \tag{4.6}$$

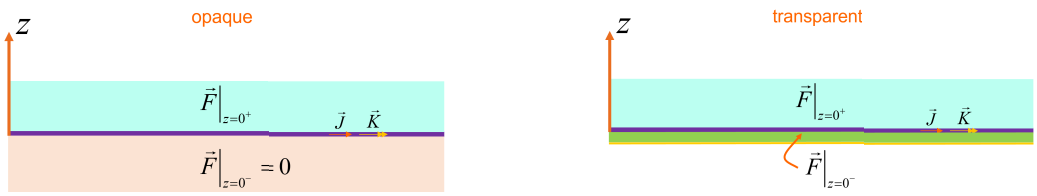

(a) (b)

Figure 4.4: Two kinds of IBCs. (a) Opaque IBCs, (b) Transparent IBCs

Therefore, the first equation in (4.3) can be simplified as follows.

$$\begin{aligned}\vec{E}_{t,av} &= \left(\overline{\overline{I}} + 2\overline{\overline{K}}_{me}\right)^{-1} \cdot \left(\overline{\overline{Z}}_{ee} \cdot \vec{J}\right) \\ &= \overline{\overline{Z}}' \cdot \vec{J}\end{aligned} \tag{4.7}$$

Then we have the commonly used IBC for opaque MTS. According to GSTCs and (4.7), relationship between "impedance" with the intrinsic parameters can be obtained. But usually this impedance will be obtained in other ways instead of the intrinsic parameters of the isolated particles.

4.3.2 Transparent IBCs

For the transparent IBC, the electric currents and magnetic currents are independent of each other. The 2 equations for both average E and H fields are required. Relationship between impedance with the intrinsic parameters can be obtained shown in Figure. 4.4(b). For the majority of designs, magnetic currents have been disregarded due to the utilization of a simple single-layered isolated patch [55]. Additionally, only anisotropic units have been utilized. These two factors combine to reduce the two equations into a single equation.

4.4 Relationship between GSTCs and IBCs

The very beginning of the history of GSTCs, the normal component of the currents are considered. However, in most research articles, the normal components have been ignored. The detail of this point has been discussed in [53, 56]. Although for both GSTCs and IBCs, the version considering normal currents have be obtained, we will only discuss the version without the normal components, which is sufficient in practice.

Although GSTCs are similar to IBCs without the inclusion of normal components of currents, initially these two boundary conditions were investigated independently. However, researchers later discovered a relationship between them. While IBCs are commonly used in practical applications, such as MTS supporting surface waves, GSTCs emphasize that the performance of a MTS can still be determined by the characteristics of the isolated particles.

It is crucial to note that there is a clear distinction between (4.1) and (4.3), despite the difference being related to inverse operations and some simple manipulations.

4.5 Surface Wave Antenna Based on Metasurface

4.5.1 Single Beam Antenna Based On Modulated Metasurface

4.5.1.1 Impedance modulation

We will use here opaque or impenetrable reactive impedance defined by tangential electric and magnetic fields at the air-MTS interface shown as follows.

$$\vec{E}_t = \overline{\overline{Z}} \cdot \hat{z} \times \vec{H}_t \Big|_{z=0^+} = \overline{\overline{Z}} \cdot \vec{J} \tag{4.8}$$

Although the model of sheet impedance (defined by discontinuity of magnetic field) over a grounded slab has been demonstrated more accurate for bandwidth description and for high-gain performance, in case of moderate gain requirements the impenetrable

impedance model is satisfactory and simpler. It is worth mentioning that the tensor reactance through this paper is Hermitian, which means that the losses are neglected and the impedance has only imaginary part $\overline{\overline{Z}} = j\overline{\overline{X}}$. For all the design examples in this section, the apertures are considered as squares of $10\lambda_0$*$10\lambda_0$, where λ_0 is the free space wavelength at 14.00 GHz.

For the MTS design, given a desired beam direction and a predefined average reactance, the tensor surface reactance can be obtained simply by the holographic formula in [16]. For the plane wave $\hat{r}_0 = \sin\theta_0\hat{x} + \cos\theta_0\hat{z}$, the components of the modulated reactance tensor are shown as follows.

$$\begin{cases} X_{\rho\rho} = X_0\left[1 + M_{\rho 0}\sin\left(\beta_{sw}\rho - k\rho\sin\theta_0\cos\varphi - \psi\right)\right] \\ X_{\rho\varphi} = X_{\varphi\rho} = X_0 M_{\varphi 0}\sin\left(\beta_{sw}\rho - k\rho\sin\theta_0\cos\varphi - \psi\right) \\ X_{\varphi\varphi} = X_0 \end{cases} \tag{4.9}$$

where X_0 is the average reactance. ρ and φ are the cylindrical coordinates of the observation point on the MTS aperture. Furthermore, $\beta_{sw} = k\sqrt{1 + \left(X_0/\eta\right)^2}$, where η is the free space wave impedance and k is the free space-wave wavenumber. The phase ψ is an arbitrary constant phase, and it has been set to be 0 in the modulations in this paper. The modulation depth for each component is taken as $M_{\rho 0} = M\cos\theta_0\cos\varphi$, $M_{\varphi 0} = -\left(M\cos\theta_0\sin\varphi\right)/2$. In this paper, we will use a reactance modulation M=0.35 and the surface wave wavenumber $\beta_{sw} = 1.35k$.

4.5.1.2 Realization Of The Modulated Impedance Surface

To realize an MTS antenna, a circular patch with a slot [57] is selected as the unit element and it is printed on Rogers 4003C substrates with a thickness of 2.032 mm by laminating two 4003C substrates (dielectric constant of 3.55 and loss tangent of 0.0027) together. The reason to choose this widely used unit cell is to demonstrate that the developed method is of general applicability. A regular hexagon cell is used in the

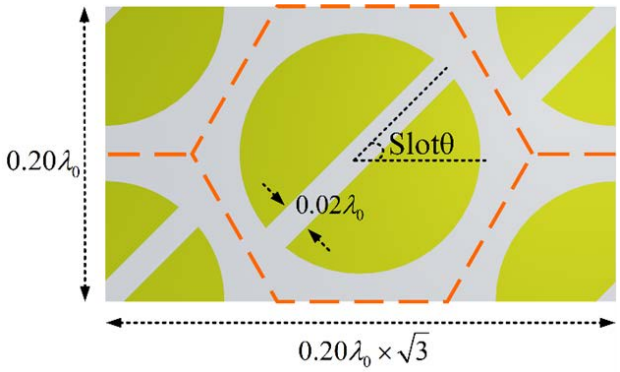

Figure 4.5: The size of the slotted circular patch (top view). In the parameter extraction, it is surrounded by periodic boundary and topped by perfectly matched layer. The slot orientation can vary to adjust the angle of the principal axis of the effective scalar reactance.

design as shown in Figure. 4.5. The distance between the center of the adjacent patches (or the width of the cell) is $0.20\lambda_0$. For the parameter extraction of the unit element, the transverse or tangential wavenumber of the wave along the surface consisting of periodic unit cells is obtained using the eigen solver of HFSS. With the wavenumber, the impedance of the surface can be calculated accordingly, which is a 2-by-2 tensor for an anisotropic impedance surface [16].

4.5.1.3 Single Beam Antenna Design

Based on the method described above, a single beam MTS antenna can be designed. The excitation of the MTS is a quarter wavelength monopole. A pencil beam in the direction of 30° relative to the Z-axis is shown in Figure. 4.6. Please note that, in this paper, the beams are scanned in the ϕ=0 degree plane, or XZ plane as shown in Figure. 4.6. Thus, the beam angle will be indicated by theta in the rest of this paper.

To investigate the performance of the single beam MTS antenna with different beam angles, 6 different antennas have been designed and simulated. The E-plane realized gain patterns from full wave simulation of these 6 antennas are given in Figure. 4.7. In all these antennas, the source is located at the center of the square aperture. The

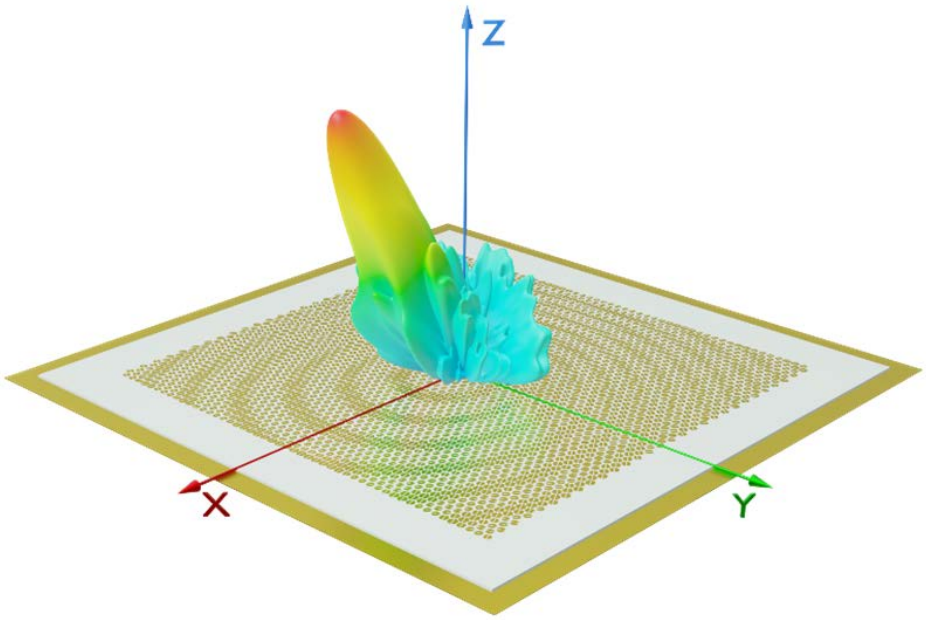

Figure 4.6: Single beam antenna with realized gain pattern.

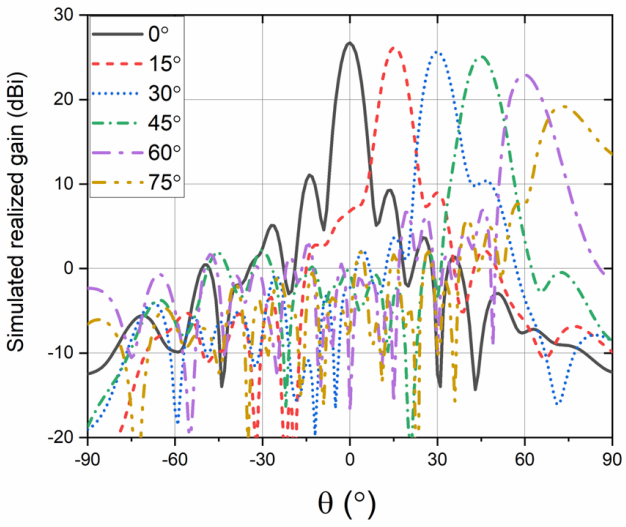

Figure 4.7: Simulated realized gain patterns at E-plane, namely XZ plane (ϕ=0 degree), for 6 single beam antennas.

E-plane for all designs in this paper is the XZ plane shown in Figure. 4.6.

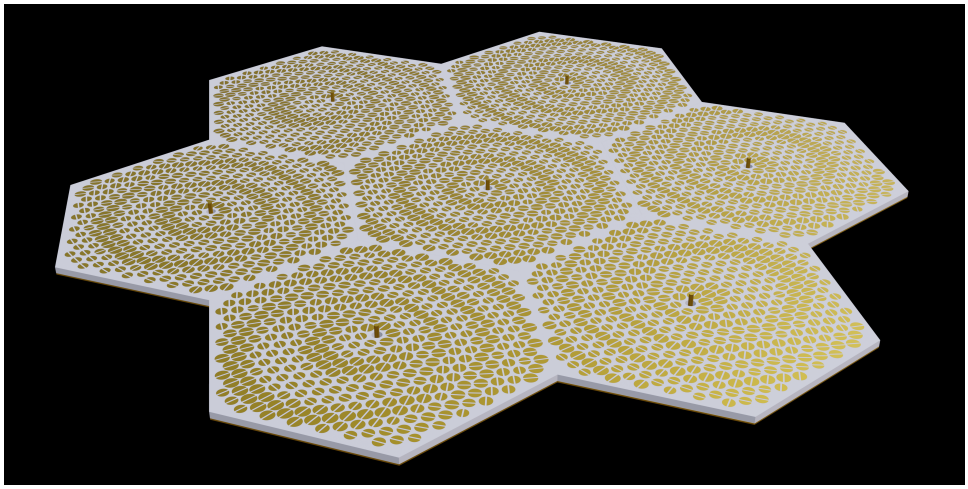

Figure 4.8: Subarray-based seven-beam antenna.

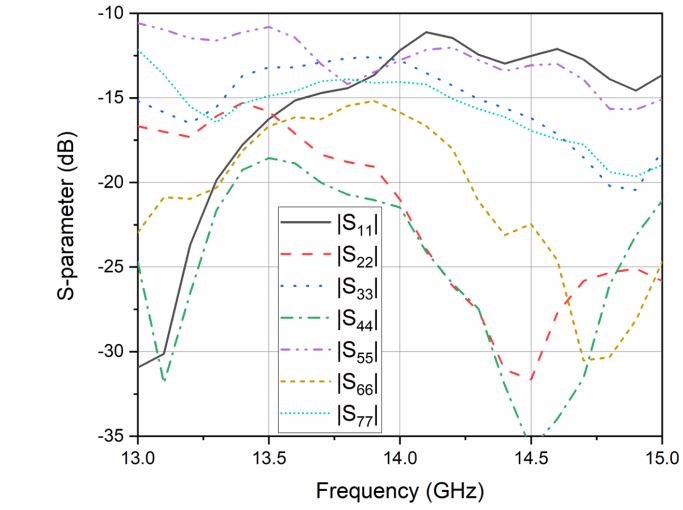

Figure 4.9: Simulated S-parameters.

4.5.2 Subarray based MBA Design

Seven subarrays are designed to implement the 7-beam antenna shown in 4.8. The whole area of the final aperture is equal to $10\lambda_0 \times 10\lambda_0$. From the simulation shown in 4.9, ports are well matched to 50 Ω loading. Mutual coupling coefficients are below -25dB for all ports. The peak AE is around 4.5% according to Figure. 4.10.

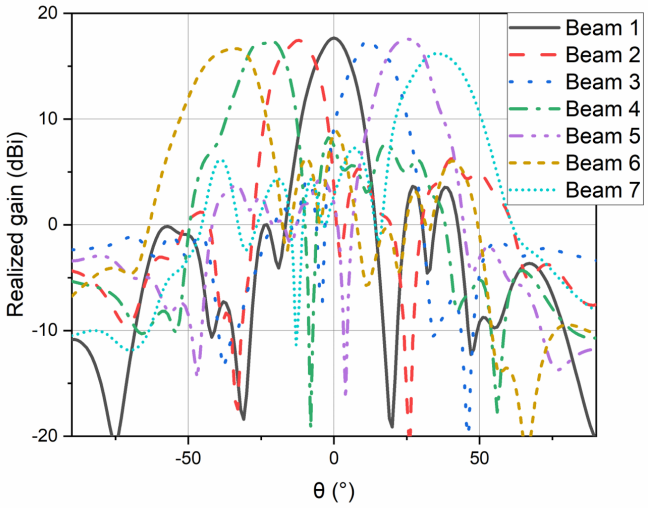

Figure 4.10: Simulated realized gain patterns at 14.0 GHz.

At the outset of the work, we designed this MBA (depicted in Figure. 4.10) with beams sharing the entire aperture. However, its performance is suboptimal, primarily due to its low AE. This design was chosen initially as it represents the simplest approach to crafting a multibeam antenna, avoiding the complexities associated with the interference issue discussed in Chapter 5, and the approach for AE improvement will be discussed in next chapter.

4.6 Chapter Summary

In this chapter, we have reviewed the concepts of GSTCs and IBCs. We have also highlighted the connection between these two important boundary conditions. To apply these concepts in practical antenna design, we have designed and analyzed both single beam antennas and subarray-based MBAs. The simulation results indicate that the performance of the single beam antenna is decent, meeting the desired specifications. However, when it comes to subarray-based MBAs, we have observed a drawback in terms

of low AE. This means that the effectiveness of utilizing the entire aperture area for radiation is compromised, leading to a reduction in overall antenna performance. The low AE in subarray-based MBAs is a challenge that needs to be addressed in order to improve their performance. Further investigations and design optimizations are necessary to enhance the AE and maximize the potential of subarray-based MBAs in practical applications.

CHAPTER 5

COMPACT MULTIBEAM ANTENNA BASED ON MODULATED MTS

5.1 Chapter Introduction

In this chapter, we will employ the concept of IBCs to model MTSs, with a particular focus on their application in the design of surface wave MTS antennas. We will also introduce an approximation technique that facilitates efficient designs of MBAs. Utilizing this approximation, we have successfully designed MBAs and evaluated their performance through simulations and measurements. Significantly, the results obtained from both simulation and measurement exhibit a high degree of agreement, serving as substantial validation for the proposed design methodology [24].

MBAs have attracted significant attention as critical components in B5G and 6G networks [58]. They can significantly enlarge the beam coverage to serve several distributed users simultaneously. Compared with digital or hybrid multi-beam technologies, passive MBAs have some commercial advantages, e.g., low manufacturing costs and low power

consumption. Recent advances on passive MBAs have been reviewed in [4, 10], including lenses [59–61], transmitarrays [62–64], reflectarrays [65], and beamforming circuits [66–68]. An alternative technology is the MTS antennas. A MTS antenna radiates by converting surface waves travelling along the surface in leaky-waves. It has advantages of a very low profile, ease of achieving high gains and a very robust antenna structure. Thus, they have been considered as attractive candidates for satellite applications [69–71], wideband/multi-band antennas [57, 72], and MBAs [73].

The theoretical basis of surface-to-leaky wave conversion modulated MTS is given in the seminal paper by Oliner and Hessel [15], who first solved the scalar problem in one dimension. It was only after sixty years that the scientific antenna community have discovered the importance of the Oliner-Hessel theory and its applicability through the use of MTS [16, 74, 75]. In particular, in [16] MTS leaky-wave 2D antenna was developed by using a design inspired by a holographic concept [76] and therefore denoted as holographic antenna. In [69, 75], the design was carried out by using the Oliner-Hessel method for the definition of local parameters. The same group further elaborated the concept in a subsequent series of papers [18, 77–79]. They introduce a more general form of modulation which makes use of boundary condition associated "penetrable" impedance boundary conditions in contrast with "impenetrable" impedance on top of a grounded dielectric slab. This allows the use of the grounded slab Green's function in the local problem, and therefore an accurate description of the dispersion phenomena and the attenuation constant along the surface. A significant improvement of the design is therefore obtained in terms of achievable gain, efficiency, side-lobes, contoured beam shape.

A multi-beam MTS was introduced in [20] by using an overlapping impedance concept and employing either a single or multiple input ports. In [80], alternatively, by using the multi-harmonics in the modulation, a single-feed 2 beam antenna was proposed. The

single-feed MBAs are useful for point-to-multi-point communications, whilst the multi-feed MBAs can provide multiple independent beams to enable multi-point-to-multi-point communications and possible MIMO optimization. For a single-feed MBAs, the surface can be divided into several sectors with each one corresponding to one beam direction; alternatively, the aperture is shared by a mathematical superposition of individual impedance modulations. The modulation superposition method has higher AE than the one obtains by the summation of individual areas and can lead to beams in the desired set of directions [20]. A single-port 2-beam MTS antenna was designed in [81] by employing the summation of the aperture fields for both beams in the synthesis. A single-port 2-beam frequency scanning antenna was proposed in [82] using multi-sector MTS. In [83], a single-feed MTS was developed to generate two Bessel beams with different beam directions. In [21] and [84], using a direct inversion process for the design of impedance, three and two symmetric shaped fan beams were generated by using three and four feed ports, respectively. In [85] and [86] an impedance MTS was developed to radiate two boresight beams at different frequencies using two ports. In [87], a dual-feed MTS was developed to generate two beams with different characteristics, e.g., polarizations, beam types, and frequencies.

It is however seen that most of the recent advances on multi-beam MTS antennas can only generate few beams, and with directions far apart. This would limit their applications in wireless communications. For most multi-point-to-multi-point communications, it is of critical importance for the MTS antennas to support a larger number of beams. There are significant challenges for MTS antennas to radiate multiple beams, which are indeed due to the significant mutual interference between different impedance modulations. Our objective in this paper is to demonstrate that the overlapping impedance concept can be applied for a higher number of pencil beams (till seven) with overlap of the aperture. To this end the total impedance is obtained by first designing the impedance

of the individual beam in isolation and then overlapping the individual modulations. It should be noted that each beam corresponds to one particular impedance modulation of MTS but there is only one surface to accommodate the modulation requirements of all the beams. As a result, there is interference between different impedance modulations, which will lead to a high SLL and a reduced directivity for each beam. One way to decrease the interference is to optimize feed locations, as the feed locations determine the final impedance modulation of the surface. In order to estimate the interference between different beams, the mutual interaction is calculated by projecting a ZOA for the current at port "i" on the impedance distribution pertinent to port "j". This allows an estimate of the electric aperture field interaction, which is eventually used for optimization of the locations of the feeding ports. In order to verify the proposed method, a 7-beam MBA with high gains and low side lobes is developed for 1-dimensional (1D) multi-beam applications. The antenna can realize a measured peak boresight realized gain of 20 dBi with SLLs less than -9 dB at 14.10 GHz and a beam coverage (10-dB overlap) up to $\pm 36^{\circ}$. The 7-beam antenna achieves a peak AE of approximately 8%, if related to the entire aperture. This efficiency is comparable or even higher than those of other MTS with a smaller number of beams. Improving the AE is the objective of our future work.

The main contributions of the paper are therefore the following. First, the definition of a new method to locate the excitation sources of an MTS antenna to decrease the SLLs. Second, based on this method, a 7-beam MTS antenna with low SLLs is achieved and successfully measured, thus demonstrating the effectiveness of the method and the feasibility to realize a high number of beams in a space which is reduced with respect to the one relevant to the summation of the apertures. It is the first time that a high number of beams is designed by making use of a single MTS.

5.2 Zeroth-Order Approaximation

In this section, based on adiabatic Floquet-wave expansion method, zeroth-order approaximation(ZOA) will be introduced to optimized the antenna. In [18][78], the Floquet-Wave expansion technique was employed to expand the currents, impedance, and aperture fields of the MTS. By performing this expansion, the different harmonics were matched at the interface of the MTS. This matching process allowed for the evaluation of the MTS's performance, particularly in the visible region of the aperture fields. In the Floquet-Wave expansion discussed earlier, solving the dispersion equation can be a complex task in practice. To simplify the design of MBAs, a ZOA of the currents on the MTS can be employed.

$$\vec{E}_t = \overline{\overline{Z}} \cdot \hat{z} \times \vec{H}_t \Big|_{z=0^+} = \overline{\overline{Z}} \cdot \vec{J} \tag{5.1}$$

where $\overline{\overline{Z}}$ represents the space-dependent impenetrable reactance, the notation 0^+ represents the limit as z approaches 0 from the upper side, $\hat{z}$ is the normal to the MTS. Although the model of "sheet" impedance (defined by discontinuity of magnetic field) over a grounded slab has been demonstrated more accurate for bandwidth description and for high-gain performance, in case of moderate gain requirements the impenetrable impedance model is satisfactory and simpler. It is worth mentioning that the tensor reactance through this paper is Hermitian, which means that the losses are neglected. For all the design examples in this section, the apertures are considered as squares of $10\lambda_0 \times 10\lambda_0$, where λ_0 is the free space wavelength at 14.00 GHz; these squares are overlapped for multi-beam design.

For the MTS design, given a desired beam direction and a predefined average reactance, the tensor surface reactance can be obtained as discussed in the previous chapter. According to [78], the reactance can be split into three contributions, which can be viewed

as three different harmonics.

$$\overline{\overline{Z}} = \overline{\overline{Z}}^{(-1)} + \overline{\overline{Z}}^{(0)} + \overline{\overline{Z}}^{(+1)} \tag{5.2}$$

After determining the impedance of the reactance surface, the tangential component of the aperture fields can be calculated by using (5.4):

$$\vec{E}_t \approx (\overline{\overline{Z}}^{(-1)} + \overline{\overline{Z}}^{(0)} + \overline{\overline{Z}}^{(+1)}) \cdot \vec{J}^{(0)} = \vec{E}^{(-1)} + \vec{E}^{(0)} + \vec{E}^{(+1)} \tag{5.3}$$

where $\vec{J}^{(0)}$ is the 0-indexed mode of the current, namely the surface wave currents on non-modulated reactance surface, and it can also be named as 0-indexed mode current. Theoretically, when modulation is introduced, it can result in a shift in the wavenumber. Consequently, the wavenumber associated with the zeroth-order mode may deviate from its predefined value. However, in the presence of a small modulation depth, the ZOA of the current enables the calculation of the aperture field from the reactance distribution with reasonable accuracy as shown in (5.3). Once the aperture fields are obtained, the far field can be calculated through the use of near-field to far-field transformation [27].

As an example, Figure. 5.1 shows the spatial and spectral domain results of the aperture fields. Figure. 5.1(a) shows the real part of the radial component of $\vec{J}^{(0)}$ on a non-modulated reactance surface with average value X0; Figure. 5.1(c) shows the magnitude of the radial component of the aperture E-field according with (5.3). The spectrum of the current and E-field on the aperture is shown in Figure. 5.1(b) and Figure. 5.1(d), respectively. The bright loops in both Figure. 5.1(b) and (d) are centered at the original point in uv plane, and the one in Figure. 5.1(d) represents the non-visible spectrum of $\vec{E}^{(0)} \approx \overline{\overline{Z}}^{(0)} \cdot \vec{J}^{(0)}$ (zero-indexed field). The radius of these two loops is β_{sw}/k=1.35, which represents the predefined refractive index for the non-modulated average reactance surface, identifying a cylindrical bounded wave on the surface whose transverse wavenumbers equal to 1.35k. The bright dot in Figure. 5.1(d) arises from the product $\vec{E}^{(-1)} \approx \overline{\overline{Z}}^{(-1)} \cdot \vec{J}^{(0)}$ between the ZOA of the current and the -1 component

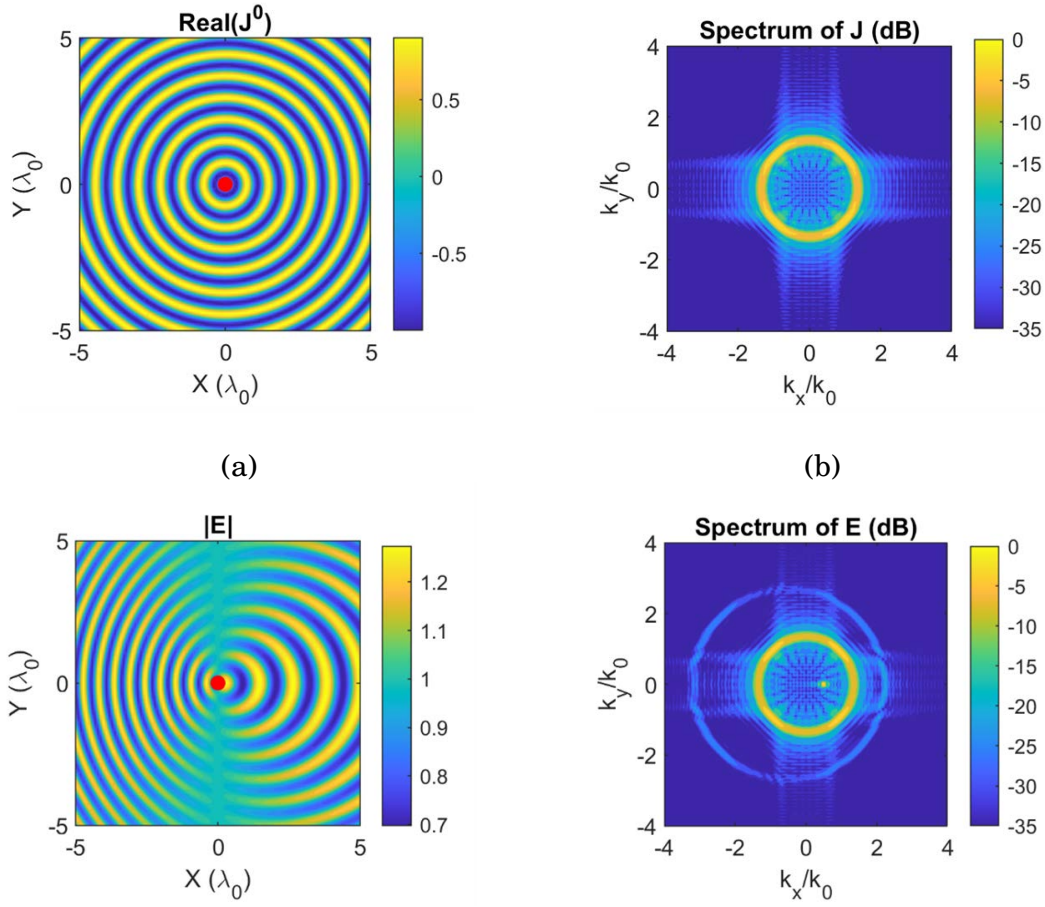

Figure 5.1: (a) Real part of normalized $\vec{J}^{(0)}$, (b) spectrum of $\vec{J}^{(0)}$, (c) magnitude of normalized $\vec{E}_t$, (d) spectrum of $\vec{E}_t$. The beam angle is θ=30° as an example.

of the impedance and indicates the direction of the desired beam by kx=ksin$\theta_0$cosϕ_0 and ky=ksin$\theta_0$sinϕ_0. The beam direction is at ϕ_0=0 ° and θ_0=30° in this example. Thus, the bright dot is at (0.5,0) in Figure. 5.1(d). The large loop in Figure. 5.1(d) represents $\vec{E}^{(+1)} \approx \overline{\overline{Z}}^{(+1)} \cdot \vec{J}^{(0)}$, the +1 indexed bounded wave introduced by the interaction between the ZOA of the current and the +1 indexed impedance contribution. We note that, in the exact expansion of currents, some extra harmonics of the expansion should appear, which are neglected here.

5.3 Shared Aperture MBA Based on MTS

5.3.1 Impedance Superposition Concept

Prior to designing the shared aperture MBA, we will conduct an investigation into the impact of the feeding location. The feeding location will be systematically varied as part of the design process. This analysis will help us determine the optimal feeding location for achieving the desired performance of the MBA.

We now investigate the effect of the source location on the performance of the single beam antenna according to full wave simulation. The coordinate system is shown in Figure. 5.2(a), (b) and (c). For simplicity, the source will be moved along the X-axis and Y-axis, respectively. Because of the symmetry of the reactance distribution, only half of the Y-axis is considered. It is worth noting that the MTS will remain unchanged with its center at the source point, and the source and the holography are moved maintaining a fixed size of the frame of $10\lambda_0 \times 10\lambda_0$ as shown in Figure. 5.2. The truncation has a different impact on the beams depending on the shift of the holography. An example is provided in Figure. 5.2(d)-(e), which shows the variation of the peak directivity of a 30 ° beam with different source locations (solid lines). The value obtained when the source is located at the center of the aperture (Figure. 5.2(a)) serves as the reference. It is observed that the directivity will drop when the source is moved far away from the aperture center in both cases. For a certain source location, it is found that the beam direction varies by a quantity θ_0 around the direction θ_0=30° when the frequency change from 13.5 GHz to 14.5 GHz. This is due to the dispersity of the MTS, which implies a change of the radial phase velocity of $\vec{J}^0$ in the bandwidth. The quantity $\partial\theta_0/\partial f \approx \Delta\theta_0/\Delta f$ is estimated for each source location and depicted in dashed line in Figure. 5.2(d) and (e). It can be seen from Figure. 5.2(d) that when the source is located along X-axis, different locations have different additional beam squint $\Delta\theta_0$ per GHz. In contrast, the beam

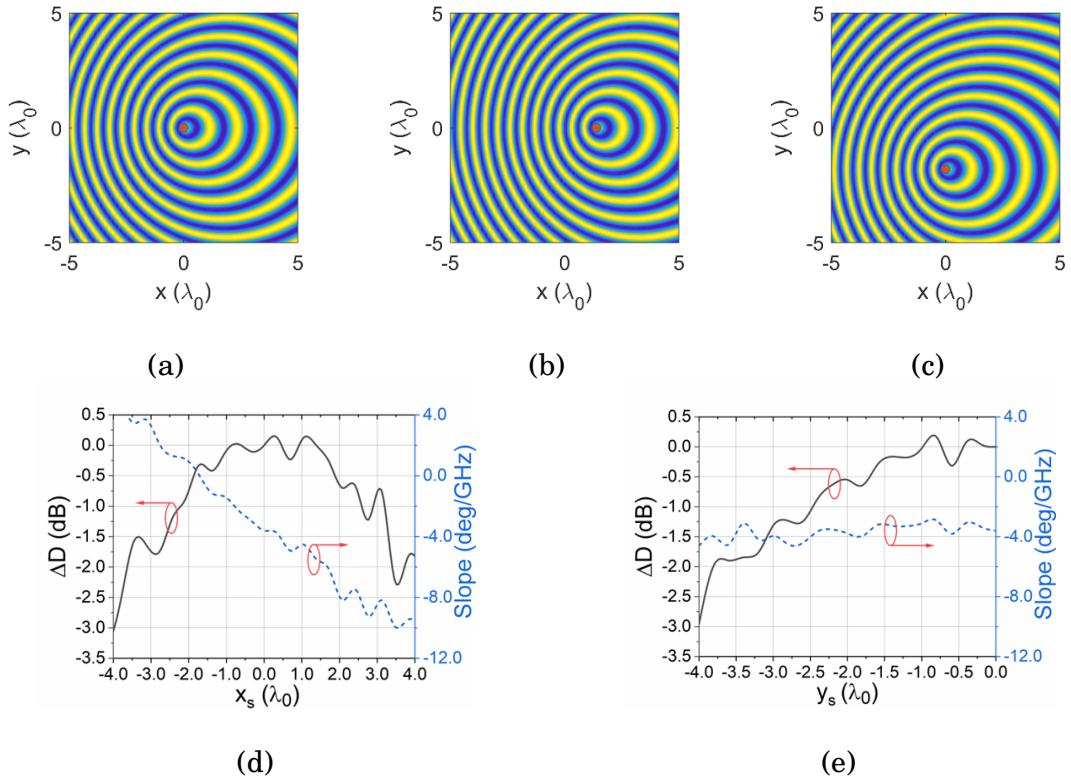

Figure 5.2: Top: (a) centered (b) x-shifted and (c) y-shifted impedance holography within the frame of $10\lambda_0 \times 10\lambda_0$. Bottom: ΔD-directivity difference between the simulated peak directivity and that for the case where x_s=0, y_s=0. (solid line, left hand scale) and the (dashed line, right hand scale) for different source-holography shifting within the fixed frame. (d) holography centered in [x_s, 0], x_s is varying; (e) holography centered in [0, y_s], y_s is varying.

direction remains relatively stable when the source is moved along Y-axis as shown in Figure. 5.2(e). Therefore, we will adopt source shifted along Y-axis in the various designs.

The design challenge for the MTS-based MBAs is the mutual interference between the impedance modulations for different beams. Such interference can increase the SLLs and decrease the directivity of each main beam. In this section, the method to alleviate the interference problem is described. We show that by analyzing the far-field results using the aperture E field based on ZOA discussed above, the optimal excitation arrangement leading to low SLLs for all beams can be found. Finally, a design procedure for the MBAs will be provided. The design example in this section has the same dimension, substrate

and modulation depth used.

For all MBAs in this paper, each beam is excited by an individual monopole. These monopoles can be excited at the same time to generate multiple beams or can be excited individually at a time to realize a single beam or beam scanning by using switches [88].

Based on the superposition of the impedance of single beam MTS antenna, the MBA impedance can be expressed as

$$\overline{\overline{Z}} = \sum_{i=1}^{N} a_i \cdot \overline{\overline{Z}}_i \tag{5.4}$$

where N is the number of the beams, a_i is the weigth coefficient of each impedance, and it is set to be 1/N, and $\overline{\overline{Z}}_i$ is the impedance of the i^{th} beam.

5.3.2 Modelling Of The Interference

The approximated aperture field along the impedance surface excited by the i^{th} source can be obtained as

$$\vec{E}_i \approx \vec{J}_i^{(0)} \cdot \overline{\overline{Z}} = a_i \cdot \vec{J}_i^{(0)} \cdot \overline{\overline{Z}}_i + \sum_{k \neq i} a_k \cdot \vec{J}_i^{(0)} \cdot \overline{\overline{Z}}_k \tag{5.5}$$

The approximated aperture field along the impedance surface excited by the ith source can be obtained. From (5.5), the first term is the self-term, which corresponds to the desired beam. The others are mutual terms, which usually contribute to the side lobes. This concept will be investigated next in the case of a 3-beam layout.

As an example, a 3-beam MTS antenna is designed to give a design guideline. For the sake of simplicity, the source of the broadside beam is always located in the center of the aperture. The beam angles are 0 °, -30 °, 30 °, respectively. The source locations for each beam are at (x_s, y_s) = (0, 0), (0, -λ_0) and (0, λ_0) respectively.

The directivity patterns for each beam in the uv plane are shown in Table (5.1) . The figures in Table (5.1) are located in a 3×5 matrix according with the following scheme.

$$\begin{bmatrix} \vec{J}_1^{(0)} \cdot \overline{\overline{Z}}_1 & \vec{J}_1^{(0)} \cdot \overline{\overline{Z}}_2 & \vec{J}_1^{(0)} \cdot \overline{\overline{Z}}_3 & \vec{J}_1^{(0)} \cdot \overline{\overline{Z}} & \vec{J}_1 \cdot \overline{\overline{Z}} \\ \vec{J}_2^{(0)} \cdot \overline{\overline{Z}}_1 & \vec{J}_2^{(0)} \cdot \overline{\overline{Z}}_2 & \vec{J}_2^{(0)} \cdot \overline{\overline{Z}}_3 & \vec{J}_2^{(0)} \cdot \overline{\overline{Z}} & \vec{J}_2 \cdot \overline{\overline{Z}} \\ \vec{J}_3^{(0)} \cdot \overline{\overline{Z}}_1 & \vec{J}_3^{(0)} \cdot \overline{\overline{Z}}_2 & \vec{J}_3^{(0)} \cdot \overline{\overline{Z}}_3 & \vec{J}_3^{(0)} \cdot \overline{\overline{Z}} & \vec{J}_3 \cdot \overline{\overline{Z}} \end{bmatrix}$$

The first three columns are the directivity patterns obtained by the individual terms in (5.5), respectively, excited by each of the 3 surface waves. The fourth column is the directivity patterns obtained by ZOA, while the fifth column is the directivity patterns obtained by HFSS full wave simulation.

The self-terms, $J_1^{(0)} \cdot \overline{\overline{Z}}_1$, $J_2^{(0)} \cdot \overline{\overline{Z}}_2$, $J_3^{(0)} \cdot \overline{\overline{Z}}_3$, represent the expected beam for each direction, while the sidelobes are attributed from the mutual terms. For example, the highlighted points shown in the second and third columns of the first row are the side lobes for the boresight beam. They are also shown in the pattern obtained by ZOA of the currents and the full wave simulation in the fourth and fifth columns of this row, respectively. Furthermore, there is reasonably good agreement between the patterns shown in column 4 and 5 on each row, as a verification of the accuracy of this model. The

Table 5.1: Different terms in equation. (5.5) for a 3-beam antenna

Term	$\overline{\overline{Z}}_1$	$\overline{\overline{Z}}_2$	$\overline{\overline{Z}}_3$	$\overline{\overline{Z}}$	HFSS
$J_1^{(0)}$	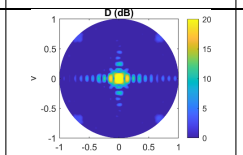	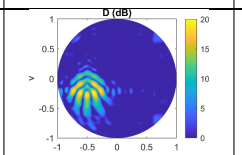	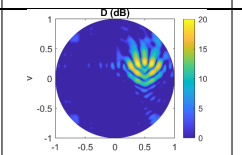	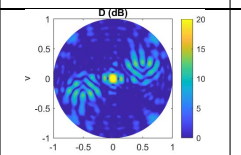	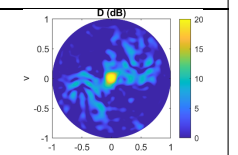
$J_1^{(0)}$	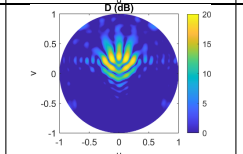	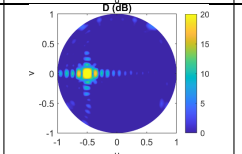	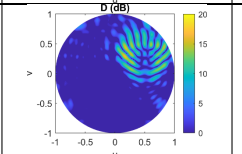	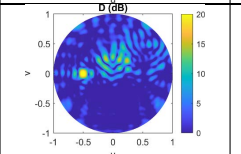	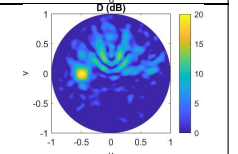
$J_1^{(0)}$	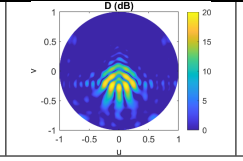	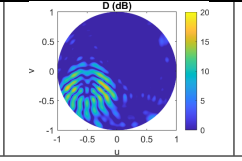	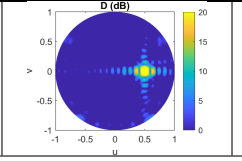	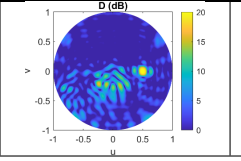	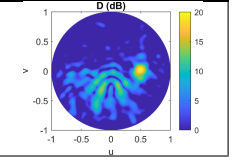

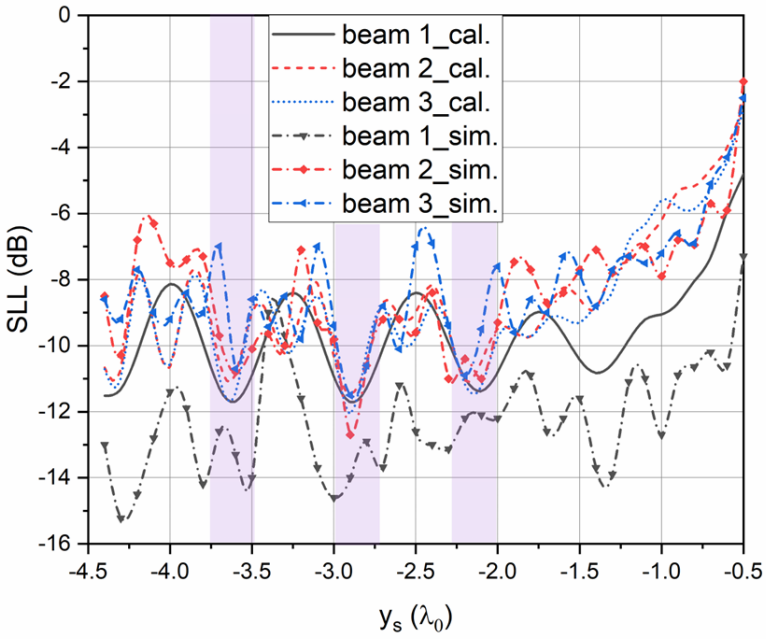

Figure 5.3: Calculated and simulated SLLs for 3-beam antennas with different source locations. The beam angles are 0 °, -30 °, 30 ° for beam 1, 2 and 3, respectively.

3-beam MTS antenna with beams at [0 °, -30 °, 30 °] and source locations at [0, 0], [0, $-y_s$] and [0, y_s] , with $-4.4\lambda_0 < y_s < -0.5\lambda_0$), is investigated to find desired ys to achieve low SLLs for each beam.

Calculated (by ZOA) and full-wave simulated SLLs are compared in Figure. 5.3. This indicates that there do exist 3 candidates in terms of low SLLs for all 3 beams as shown in the pink rectangular bars shown in Figure. 5.3. Three additional candidates exist for $0.5\lambda_0 < y_s < 4.4\lambda_0$, which are not depicted in the figure. Accordingly, 6 potential source locations can lead to low SLLs. But these locations may lead to different values of realized gains. Thus, these positions should be considered in full wave simulations to achieve high realized gains and low SLLs. Next, the influence of the source locations on the SLLs for different beam angles is investigated. The beam angles are indicated by 0 °, $-\theta_b$ °, θ_b °, respectively, where θ_b ° is an independent variable, ranging from 5 to 50

as shown in Figure. 5.4. The source locations for 3 beams are [0, 0], [0, -y_s] and [0, y_s] respectively, and y_s varies from -4.4λ_0 to -0.5λ_0 as shown in Figure. 5.3. In other words, given θ_b and ys, a 3-beam antenna will be obtained. Figure. 5.4 shows the calculated SLLs of the three beams for 3-beam antennas with different θ_b and ys. Again, the goal is to find desired ys for low SLLs. The results for y_s>0.5λ_0 are not shown in the figure since they are similar to that for y_s<0.5λ_0. It is noted that the source location for the beam at 0 ° is at the [0, 0] and it remains unchanged. For the other two beams, their source locations are mirrored with respect to the X-axis and scanned along Y-axis. The calculated SLLs for beam 1, 2 and 3 in Figure. 5.3 are the θ_b=30 ° cut of Figure. 5.4(a), (b) and (c) respectively. As shown in Figure. 5.4, the bright strip represents a high SLL. For example, when y_s=-0.5λ_0, the ports for these three beams are located at [0, 0], [0, 0.5λ_0] and [0, -0.5λ_0] respectively. The SLLs of these three beams in this case are high due to the significant interference of each surface wave. The SLLs of the beams can be reduced when the other two ports are moved away from y_s=0.5λ_0. The preferred y_s is in the dark strips, namely y_s=-2.2λ_0, -3λ_0, -3.7λ_0, considering the low SLLs for all 3 beams simultaneously. Furthermore, when the beam steering angels, θ_b, are changed, the above locations can still lead to low SLLs.

As a summary, by using ZOA based field calculation, we can obtain a few positions of the feeding ports that can lead to low SLLs. Then, we can use full-wave simulations to calculate the performance of the MTS antenna for these selected positions only rather than blindly trying all positions across the aperture.

5.3.3 Overall Design Procedure

According to the analysis and simulations discussed above, the whole design procedure for MTS-based MBA can be summarized as follows:

Step 1: Choose modulation parameters, including average refractive index and modula-

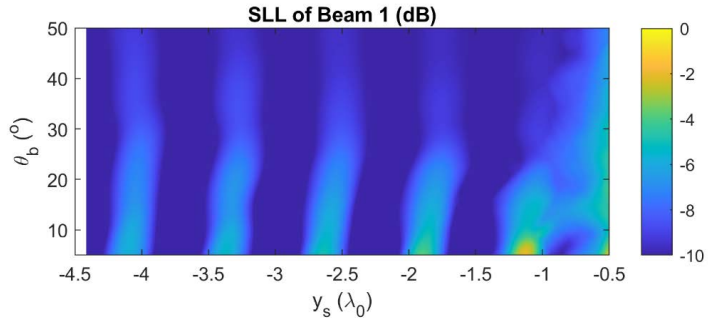

(a)

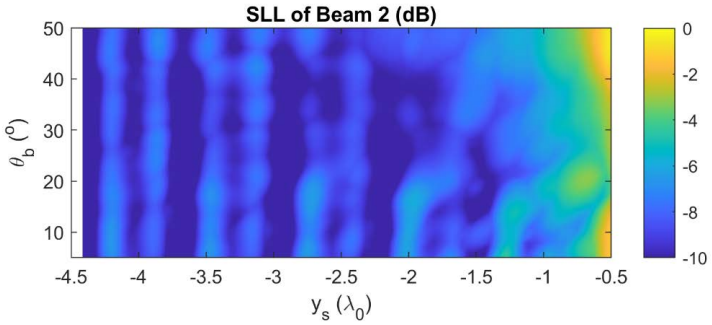

(b)

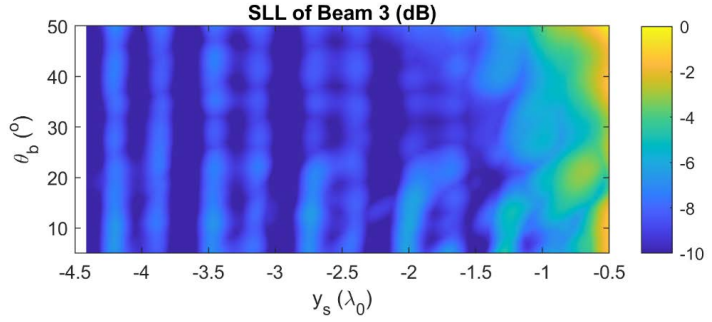

(c)

Figure 5.4: SLLs for 3-beam antenna with different source locations and beam angles. (a) the beam angle is 0, the feed location is [0,0]. (b) the beam angle is -θ_b°, the feed location is [0, -y_s]. (c) the beam angle is θ_b°, the feed location is [0, y_s].

tion depth, according to single beam antenna performance.
Step 2: According to the desired gain for each beam, choose the weighting coefficient in the superposition of the impedance in (5).
Step 3: Choose the potential feeding port locations along the line perpendicular to E-plane for each beam. For different locations, use ZOA to calculate the far-field radiation patterns and select the locations that can lead to low SLLs. Generally, the case where the distance between adjacent source is much less than λ_0 can be ignored in the calculation due to the strong mutual coupling of the ports and high SLLs.
Step 4: For the feeding port locations selected in Step 3, carry out the full-wave simulations for the antenna, and choose the designs with the highest realized gains for all beams.

It should be noted that superimposing different individual modulations to obtain one common modulation saves significant amount of time and effort in the impedance synthesis process, but this may not be the optimal method. Further research is required to find alternative solutions which may lead to reduced mutual interference between different beams.

5.4 7-Beam Antenna Design

In this section, based on the design procedure in the previous section, a 7-beam MTS antenna is designed. The design in this section keeps the dimension, substrate, and modulation parameters the same as those of the 3-beam MTS antenna. The beam angles for the 7-beam antenna are chosen as 0 °, -12 °, 12 °, -24 °, 24 °, -36 °, 36 °, respectively. The ports correspond to the beams at angles of 0 °, -12 °, 12 °, -24 °, 24 °, -36 °, 36 °, are ports 1, 2, 3, 4, 5, 6, and 7, respectively. The photo of the prototype is shown in Figure.5.5.

Similar to the 3-beam design, the 7-beam antenna steer its beam along the phi=0 °

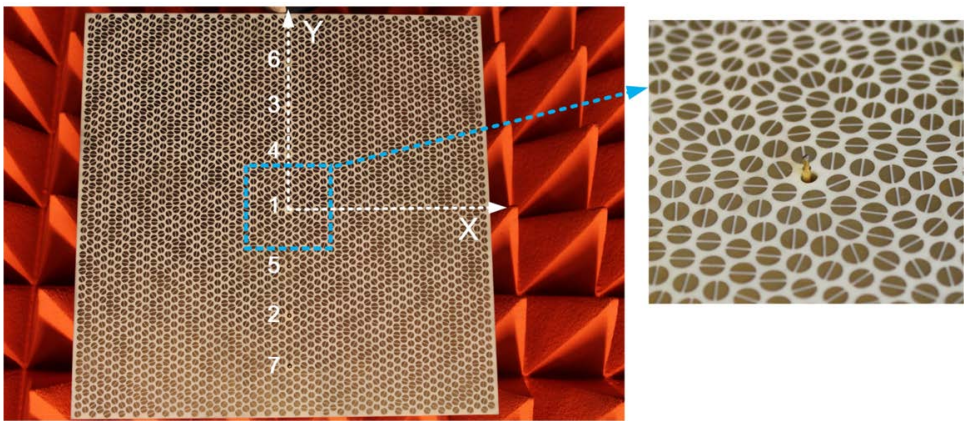

Figure 5.5: The prototype of the 7-beam antenna. The numbers represent the port index for each beam.

plane (XZ plane), as shown in Figure. 5.6, and Y-axis is chosen as the locations of the feeding ports. Again, the port locations for symmetric beams will be mirrored in terms of the x axis. Based on the calculation of 7 patterns for all potential source locations using the ZOA method, some candidates with low SLLs, say -10 dB, can be obtained. Then, full wave simulations for these small numbers of candidates are carried out to select the ports that can lead to highest realized gains. For this 7-beam antenna with beam angle [0 °, -12 °, 12 °, -24 °, 24 °, -36 °, 36 °], the optimized source locations for each beam are [0, 0], [0, -2.6λ_0], [0, 2.6λ_0], [0, 1.4λ_0], [0, -1.4λ_0], [0, 3.8λ_0], [0, -3.8λ_0], respectively. The proposed 7-beam antenna with its three-dimensional realized gain patterns are shown in Figure.5.6.

5.4.1 S-Parameters and Realized Gain Patterns

The measured S-parameters are presented in Figure. 5.7 and Figure. 5.8 When one port is excited, the others are loaded with 50 Ω matching impedances. The $|S_{ii}|$ values in Figure. 5.7 indicate that the reflection coefficients for all 7 ports are below -15 dB, with respect to the 50 Ω source across the operating band. The mutual coupling coefficients among all 7 ports are shown in Figure. 5.8. It clearly demonstrates that all 7 ports

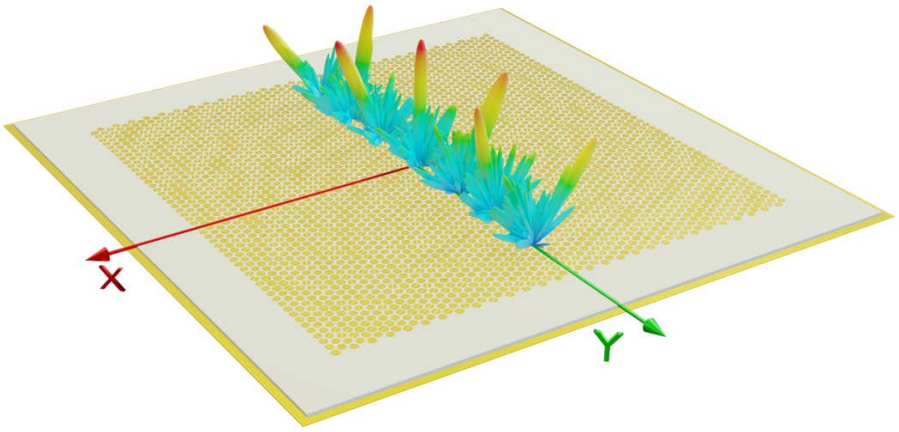

Figure 5.6: Proposed 7-beam antenna with realized gain patterns.

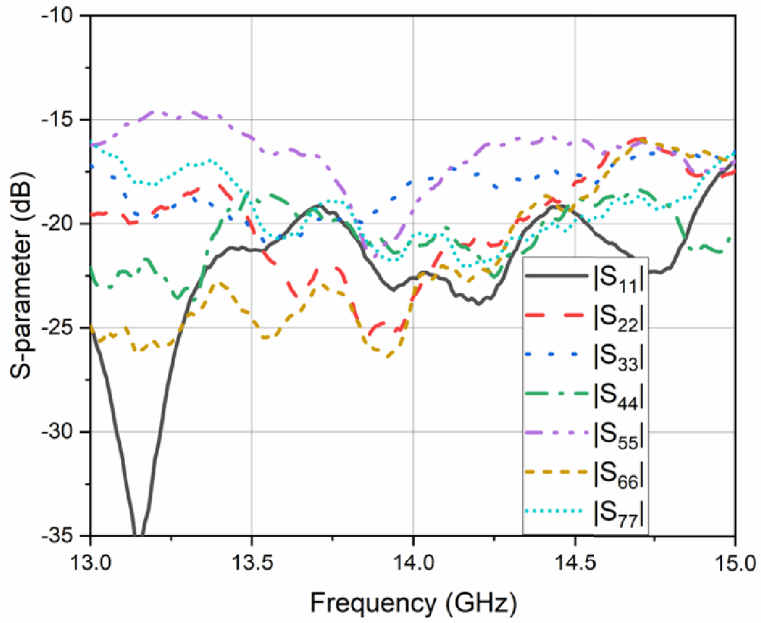

Figure 5.7: Measured reflection coefficients for different ports of the antenna.

are well isolated from each other. The radiation patterns and antenna realized gains were measured at MVG compact range located at University of Technology Sydney, Australia. The simulated and measured realized gains for each beam as a function of the frequency are plotted in Figure. 5.9(a) and (b). It should be noted that for the beams 1, 2,

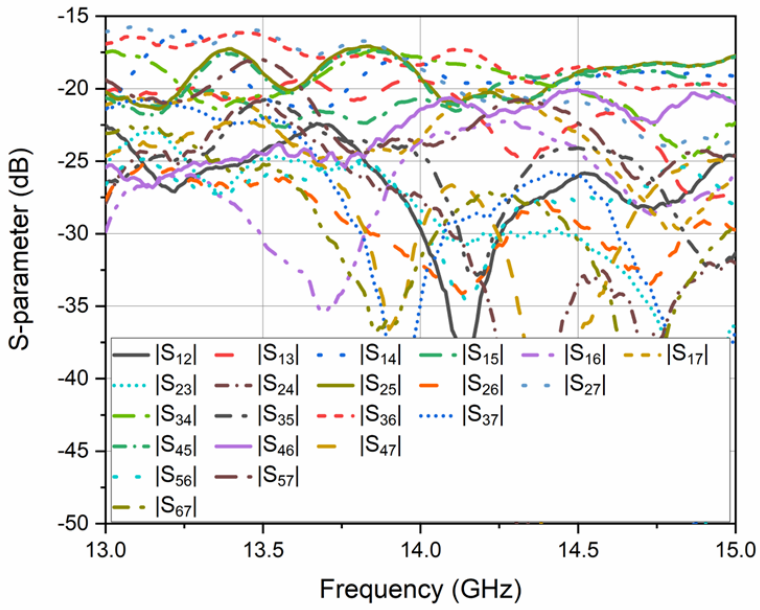

Figure 5.8: Measured mutual coupling coefficients.

4 and 6, there is an around 1.0 ° to 2.0 ° difference of the main beam angle between the simulations and measurements. The measured antenna beam directions remain very stable across the operating frequency band, as shown in Figure. 5.9(c). The simulated peak realized gain for beam 1 is 20.2 dBi at 14.20 GHz, and the 3-dB bandwidth is around 7%. The simulated peak gain for beam 6 is 2 dB lower than that for the broadside beam, while for beam 7, the gain drop is 3 dB. The measured realized gain is shown in Figure. 5.9(b). It has the peak value of 20.0 dBi at 14.10 GHz for the broadside beam. The predicted E-plane realized gain patterns at 14.20 GHz for the 7-beam antenna are shown in Figure. 5.10. The corresponding measured results are shown in Figure. 5.11. Good agreement can be observed. It is noticed that the beam can be scanned to 72 ° with an about 3-dB gain drop from the maximum value for the simulation, while the gain drop is 4 dB for the measurement which can be attributed to the fabrication tolerance and measurement errors.

From Figure. 5.10, it can be observed that the E-plane patterns are not symmetric.

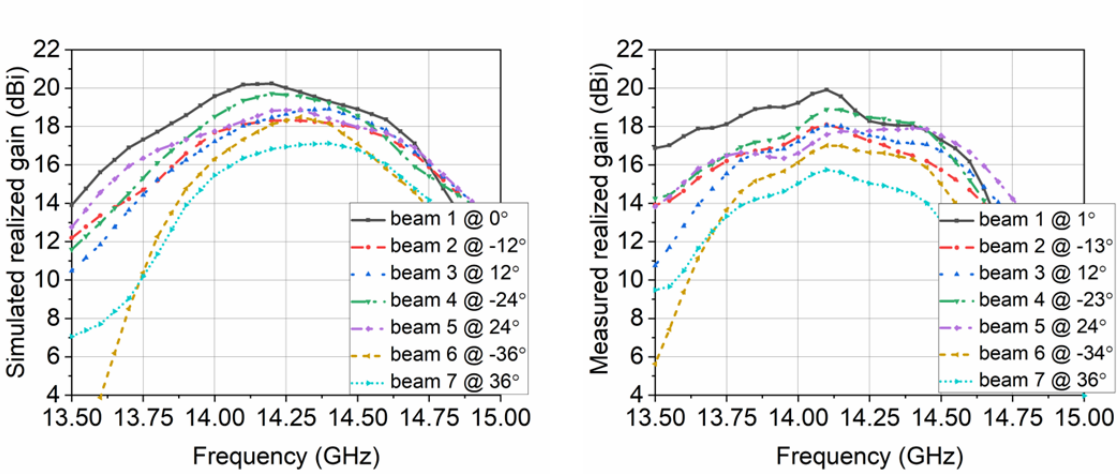

(a) (b)

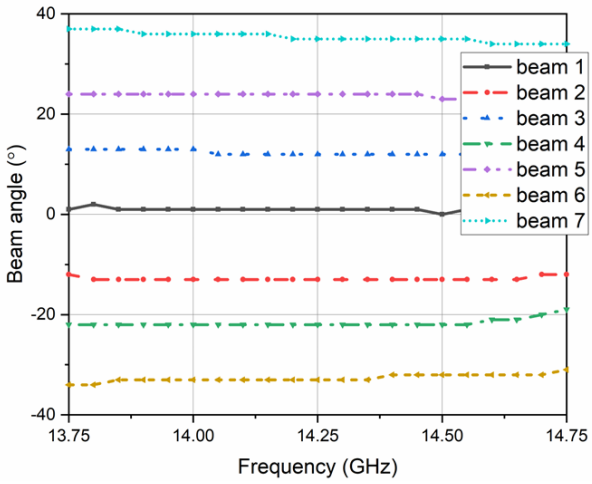

(c)

Figure 5.9: (a) Simulated realized gain. (b) Measured realized gain. Beam 1, 2, 3, 4, 5, 6, and 7, corresponds to the gain at the ports 1, 2, 3, 4, 5, 6, and 7, respectively, at the specific angles indicated in the captions. (c) Measured beam angles versus frequency.

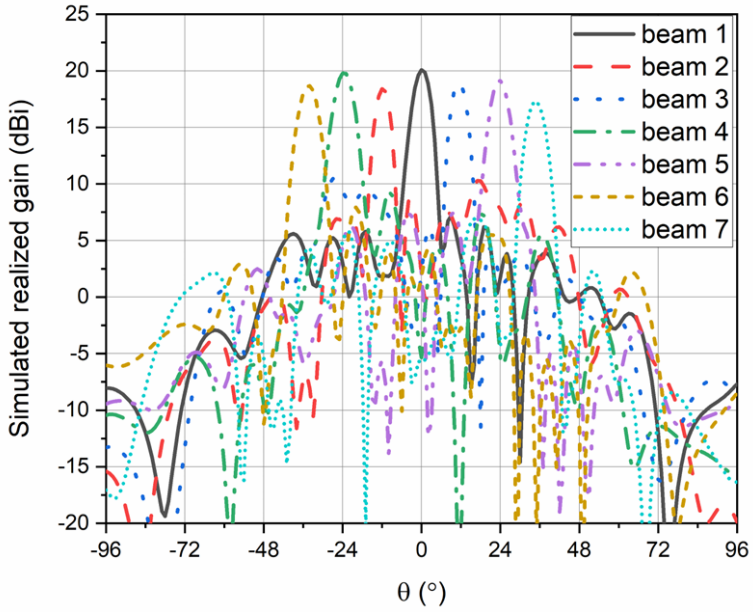

Figure 5.10: Simulated E-plane realized gain patterns at 14.20 GHz.

This can be attributed to the following two reasons. Firstly, the impedance distribution of the broadside beam is asymmetric, which results in an overall asymmetric impedance distribution of the aperture. Additionally, there could be some antenna implementation errors that lead to asymmetric patterns. The simulated and measured SLLs are lower than -9 dB for all the beams.

The measured E-plane realized gain patterns for the cross-polarization of E-plane are shown in Figure. 5.12. The cross-polarized realized gains are less than 5 dBi for all the 7 beams, which is less than -10 dB comparing with the realized gains of col-polarization.

5.4.2 Comparisons with other solutions presented in literatures

Table 5.2 lists the performance characteristics of MBAs reported in the open literature as well as those achieved in this work, such as beam number, AE, and SLLs. It can be noted that most of the reported work has a limited number of beams. The antenna in

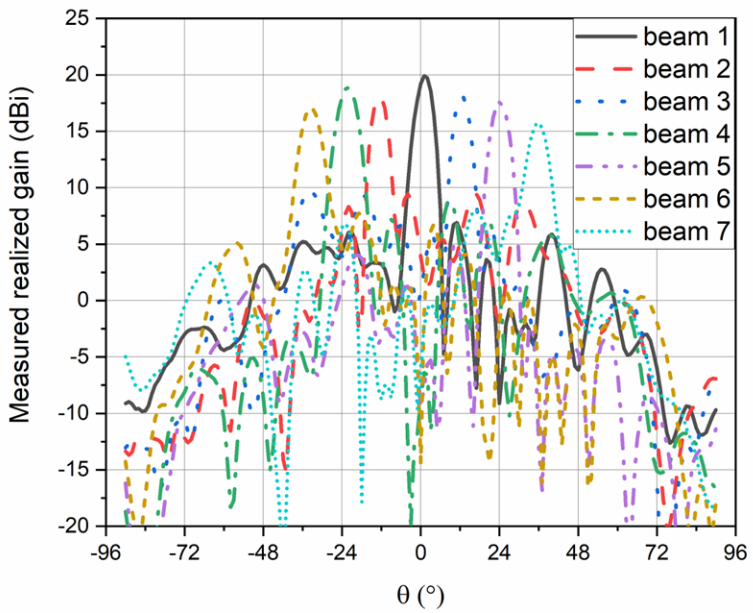

Figure 5.11: Measured E-plane realized gain patterns at 14.10 GHz.

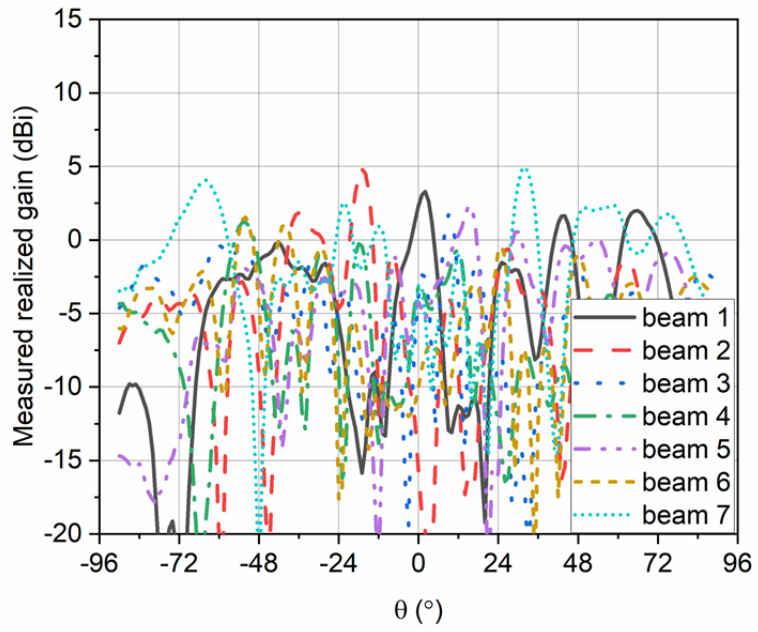

Figure 5.12: Measured E-plane realized gain patterns of cross-polarization at 14.10 GHz.

[20] can achieve 4 beams with 2 beams at each principal plane. In our work, 7 pencil beams are generated which can further enhance the feasibility for MTS-based MBAs to be employed in future wireless communications systems. Additionally, it should be

noted that almost all the MBAs have a low AE with no more than 3 beams. Nonetheless, in this work, our 7-beam antenna achieved a peak AE of around 8%. The AE has been calculated using the realized gain of the broadside beam.

For a larger aperture with a given number of beams, we can achieve at least comparable performance as the current design. This is because as shown in Figure. 5.4, the locations of the feed ports that leading to low SLLs can still be satisfied for a larger aperture. More importantly, a larger aperture will be very helpful if we want to achieve a larger number of beams as more space are needed for more feeds.

5.4.3 Flexibility of the optimized source locations

As shown in Figure. 5.4, for different beam directions, the source locations for low SLLs do not change much. As an example, this subsection verifies the performance of a 7-beam antenna with beam directions of 0 °, -10 °, 10 °, -20 °, 20 °, -30 °, and 30 °, using the same source locations as the previous 7-beam antenna with beam angles of 0 °, -12 °, 12 °, -24 °, 24 °, -36 °, and 36 °.

The size of the aperture and the modulation depth are the same as those of the previous 7-beam design. But the surface impedance of this MTS antenna has been re-calculated according to the new beam directions, thereby leading to different layout of the configurations of the slotted circular patches across the aperture. The details are omitted here for brevity.

The simulated realized gains across the frequency band are shown in Figure. 5.13. The 3-dB bandwidth for the boresight beam is about 8% (13.60 GHz-14.70 GHz). The simulated E-plane realized gain patterns at 14.20 GHz are shown in Figure. 5.14. The maximum gain is around 19 dBi for the boresight beam and the beams can be scanned to 60 ° with a scanning loss of around 1 dB. In this example, the lower scanning loss is due to both the reduced realized gain of the broadside beam and the smaller scanning

Table 5.2: Performance Comparison of MTS based MBAs

Ref.	Freq (GHz)	Aperture area	Beam info.	Port num.	Beam num.	AE	Realized gain (dBi)	SLLs (dB)
[20]	26.25	$\pi\times(12\lambda_0)^2$	Pencil beam	4	4 beams at two orthogonal planes	12.2% (sim.)	27.8 (sim.)	-10 (sim.)
[82]	16.00 to 19.00	$14\lambda_0\times14\lambda_0$ at 17.50 GHz	Pencil beam	1	2	-	-	-10
[83]	15.00	$11.75\lambda_0\times11.75\lambda_0$	Bessel beams	1	2	-	-	-14
[21]	24.00	$\pi\times(10\lambda_0)^2$	Shaped beam	3	3 sectoral beams	-	20.0 (sim.)	-7 (sim.)
[84]	24.00	$\pi\times(10\lambda_0)^2$	Shaped beam	4	2	-	21.0 (sim.)	-13 (sim.)
[85]	17.00 and 20.00	$13.5\lambda_0\times13.5\lambda_0$ at 17 GHz and $15.9\lambda_0\times15.9\lambda_0$ at 20 GHz	Pencil beam	2	2	3%, 5.5%	18.3, 22.4	-14.1, -10.5
[87]	12.00 and 15.00	$9.4\lambda_0\times9.4\lambda_0$ at 12 GHz and $11.75\lambda_0\times11.75\lambda_0$ at 15 GHz	Vortex beam, Bessel beam	2	2	-	-	-
This work	14.00	$10\lambda_0\times10\lambda_0$	Pencil beam	7	7	8%	20	-9

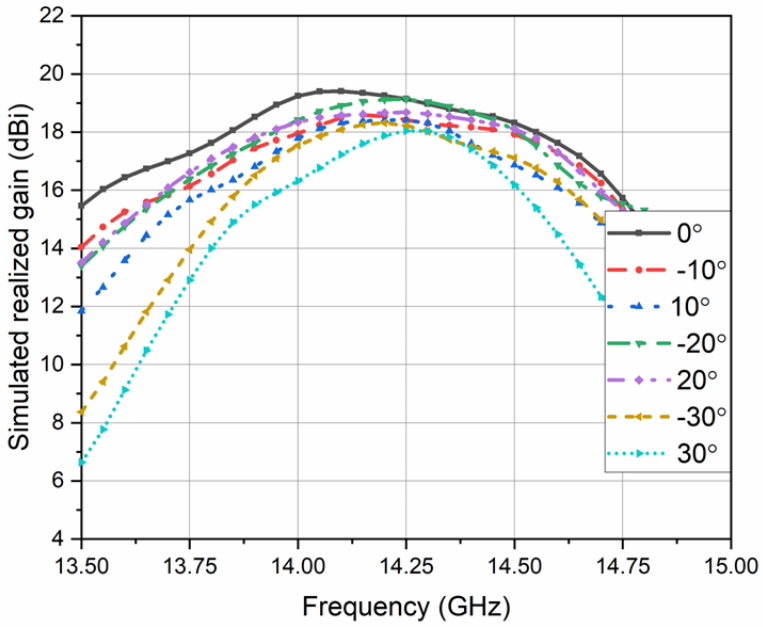

Figure 5.13: Simulated realized gains across the frequency band.

range compared to the previous design.

It should be noted that although a certain source location may be suitable for achieving different beam angles, better antenna performance can be realized if we use Steps 3 and 4 in Section 5.3.3 to re-calculate the optimal feed positions for different beam angles.

5.5 Chapter Summary

This chapter has presented a new method to address the mutual interference between the surface waves excited by multiple ports for an MTS-based MBA. A time-efficient optimization of the port locations is employed to generate multiple high-gain pencil beams with low SLLs. As a validation, a 7-beam prototype operating at 14.20 GHz is designed, fabricated, and successfully measured. The realized gain of the boresight beam is 20 dBi with multi-beam radiation angles covering from -36 ° to 36 °. The developed

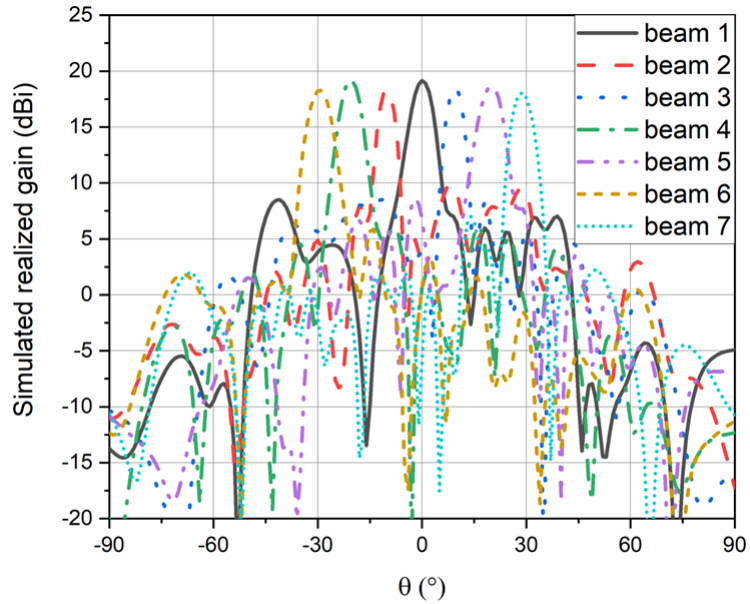

Figure 5.14: Simulated E-plane realized gain patterns at 14.20 GHz.

MBA is expected to find wide applications in future advanced wireless communications systems where multiple beams are used to serve multiple users simultaneously.

CHAPTER 6

CONCLUSIONS

6.1 Chapter Introduction

In this chapter, the conclusions drawn from the work will be presented. The findings and outcomes of the research will be summarized, highlighting the key contributions and implications. Following the conclusion, a discussion on future work related to the topic will be presented. This will involve identifying potential areas for further investigation, suggesting possible improvements or extensions to the current research, and outlining potential research directions to advance the field.

6.2 Concluding Remarks

A monopole mounted on a finite ground plane radiates an elevated main beam, resulting from the induced currents on the ground. By inserting resonant slots in the ground, this elevated angle can be suppressed significantly. Yagi-Uda monopoles were then developed to redirect the beam back to endfire direction along the horizontal plane with a gain

improvement. Simulation and measurements of a sector of a circular array verified the design concepts.

Regarding the coverage of MBAs, it is useful for practice that due to the rotational symmetry of the entire array, full azimuth coverage can be achieved. This means that the antenna array can effectively cover a complete 360° azimuthal angle. The rotational symmetry enables the antenna to provide uniform coverage in all directions around its central axis. This property is advantageous in applications where omnidirectional coverage is required, allowing for reliable communication or sensing in various directions without the need for mechanical rotation or repositioning of the antenna system.

Therefore, the technology developed to re-direct the main beam of a monopole-based Yagi-Uda array to the horizontal direction is validated. It is noted that the realized gain patterns of the Yagi-Uda unit excited by Port 1 in the prototype sector are slightly different from those of the single unit (unit 1) of the circular array. These differences occur because the dimensions of the three fabricated units of the sector were optimized in regards to the entire circular array environment, not just as a single unit.

The measured radiation patterns have larger backlobe levels than the simulated ones do. This difference is attributed to inaccuracies in the distance of the antenna from the additional conducting plate that had to be introduced for mounting the antenna in the measurement chamber. Stray currents excited on the long cables present in the measurements also contributed to this difference.

To design compact MBAs, it is essential to analyze the basic concepts behind metasurfaces, such as GSTCs and IBCs. Understanding these principles enables the development of compact antenna designs that are based on a solid foundation.

By leveraging the GSTCs and IBCs, it becomes possible to manipulate the behavior of electromagnetic waves at the MTS interface. These conditions provide guidelines for controlling the transmission, reflection, and absorption of electromagnetic waves,

allowing for the design of antennas with unique properties and functionalities.

Applying the principles of GSTCs and IBCs in antenna design can lead to compact configurations that offer improved performance in terms of size, bandwidth, efficiency, and radiation characteristics. By harnessing the capabilities of metasurfaces, it becomes feasible to achieve miniaturization and integration of antennas without compromising their overall performance.

In summary, the analysis of the basic concepts of metasurfaces, including GSTCs and IBCs, serves as a foundation for proposing compact antenna designs. This knowledge empowers engineers and researchers to explore innovative approaches in developing efficient and space-saving MBAs.

Regarding to MTS based MBA design, this thesis has presented a new method to address the mutual interference between the surface waves excited by multiple ports for an MTS-based MBA. A time-efficient optimization of the port locations is employed to generate multiple high-gain pencil beams with low SLLs.

6.3 Future Works

When considering the coverage of MBAs, it is important to acknowledge the need for further research to achieve wider coverage ranges. The designs discussed in Chapter 3, which include commonly used planar lenses, primarily support full coverage in the azimuthal plane. However, they may not provide complete coverage in other planes or angles.

Similarly, the designs presented in Chapter 5, as described in various research articles, typically focus on achieving coverage in a single elevation plane. While these designs can be effective within that specific plane, they may not provide comprehensive coverage in other planes or angles of interest.

Expanding the coverage range of MBAs is a topic that warrants further investigation

and exploration. Researchers can explore novel approaches and techniques to extend the coverage capabilities of MBAs beyond specific planes. This could involve developing MTS designs that offer multi-plane coverage or investigating the integration of multiple MBAs to achieve comprehensive coverage across different angles and planes.

By addressing the challenge of wider coverage, researchers can unlock new possibilities for MBAs in various applications, including wireless communications, radar systems, and satellite communications. The development of MBAs with broader coverage ranges will enhance their versatility and enable their deployment in diverse scenarios where comprehensive coverage is required.

In conclusion, further research is necessary to advance the field of MBAs and develop designs that provide wider coverage ranges, surpassing the limitations of existing designs that are predominantly focused on specific planes or angles. By doing so, MBAs can fulfill the demands of a broader range of applications and contribute to advancements in wireless communication and sensing systems.

When considering the development of compact high-gain MBAs in the future, metasurfaces emerge as a promising solution. However, the synthesis of metasurfaces specifically tailored for MBA design requires further investigation and exploration.

Chapter 4 of the research provides valuable insights into the synthesis and design aspects of metasurfaces. By leveraging complex materials, such as bianisotropic materials, it is possible to enhance the performance of metasurfaces and, consequently, the performance of MBAs.

Introducing bianisotropic materials into the synthesis process offers an opportunity to manipulate electromagnetic fields with greater flexibility. These materials exhibit unique properties that enable control over both electric and magnetic responses simultaneously. By incorporating such materials into the design of metasurfaces, improved performance in terms of radiation characteristics, beam shaping, polarization control, and other

desired parameters can be achieved.

The investigation of MTS synthesis for MBA design entails exploring various approaches, such as optimization algorithms, computational methods, and advanced material engineering techniques. These investigations aim to develop systematic methodologies that can efficiently synthesize metasurfaces to meet specific requirements, such as compact size, high gain, and customized radiation patterns.

By advancing the synthesis techniques for metasurfaces, researchers can unlock the full potential of compact high-gain MBAs. These antennas have numerous applications, including wireless communications, satellite systems, and radar technology, where high-gain performance within limited physical dimensions is crucial.

In summary, the future development of compact high-gain MBAs can benefit significantly from the utilization of metasurfaces. The synthesis of metasurfaces, particularly incorporating complex materials like bianisotropic materials, requires further investigation. Through such research, improved performance and enhanced capabilities can be achieved, leading to advancements in compact high-gain MBA designs with applications across various industries.

LIST OF FIGURES

FIGURE **Page**

BIBLIOGRAPHY

[1] "All.space." `https://www.all.space/`.
Accessed: 2023-12-01.

[2] H. Fan, X. Liang, J. Geng, R. Jin, and X. Zhou, "Switched multibeam circular array with a reconfigurable network," *IEEE Transactions on Antennas and Propagation*, vol. 64, no. 7, pp. 3228–3233, 2016.

[3] Z. L. Ma and C. H. Chan, "A novel surface-wave-based high-impedance surface multibeam antenna with full azimuth coverage," *IEEE Transactions on Antennas and Propagation*, vol. 65, no. 4, pp. 1579–1588, 2017.

[4] W. Hong, Z. H. Jiang, C. Yu, J. Zhou, P. Chen, Z. Yu, H. Zhang, B. Yang, X. Pang, M. Jiang, *et al.*, "Multibeam antenna technologies for 5g wireless communications," *IEEE Transactions on Antennas and Propagation*, vol. 65, no. 12, pp. 6231–6249, 2017.

[5] D. Archer, "Lens-fed multiple beam arrays," *Microwave Journal*, vol. 27, p. 171, 1984.

[6] Y. Li, L. Ge, M. Chen, Z. Zhang, Z. Li, and J. Wang, "Multibeam 3-d-printed luneburg lens fed by magnetoelectric dipole antennas for millimeter-wave mimo applications," *IEEE Transactions on Antennas and Propagation*, vol. 67, no. 5, pp. 2923–2933, 2019.

[7] D. McGrath, "Planar three-dimensional constrained lenses," *IEEE Transactions on Antennas and Propagation*, vol. 34, no. 1, pp. 46–50, 1986.

[8] G. Liu, M. R. D. Kodnoeih, K. T. Pham, E. M. Cruz, D. González-Ovejero, and R. Sauleau, "A millimeter-wave multibeam transparent transmitarray antenna at ka-band," *IEEE Antennas and Wireless Propagation Letters*, vol. 18, no. 4, pp. 631–635, 2019.

[9] D. Berry, R. Malech, and W. Kennedy, "The reflectarray antenna. ieee transaction on antennas and propagation, 11, 645-651," 1963.

[10] Y. J. Guo, M. Ansari, R. W. Ziolkowski, and N. J. Fonseca, "Quasi-optical multi-beam antenna technologies for b5g and 6g mmwave and thz networks: A review," *IEEE Open Journal of Antennas and Propagation*, vol. 2, pp. 807–830, 2021.

[11] J. Zenneck, "Propagation of plane em waves along a plane conducting surface," *Ann. Phys.(Leipzig)*, vol. 23, no. 1, p. 907, 1907.

[12] A. Sommerfeld, "Propagation of waves in wireless telegraphy," *Ann. Phys.(Leipzig)*, vol. 28, pp. 665–737, 1909.

[13] J. A. Polo Jr and A. Lakhtakia, "Surface electromagnetic waves: a review," *Laser & Photonics Reviews*, vol. 5, no. 2, pp. 234–246, 2011.

[14] R. E. Collin, *Field theory of guided waves*, vol. 5.
John Wiley & Sons, 1990.

[15] A. Oliner and A. Hessel, "Guided waves on sinusoidally-modulated reactance surfaces," *IRE Transactions on Antennas and Propagation*, vol. 7, no. 5, pp. 201–208, 1959.

[16] B. H. Fong, J. S. Colburn, J. J. Ottusch, J. L. Visher, and D. F. Sievenpiper, "Scalar and tensor holographic artificial impedance surfaces," *IEEE Transactions on Antennas and Propagation*, vol. 58, no. 10, pp. 3212–3221, 2010.

[17] F. Caminita and S. Maci, "New wine in old barrels: The use of the oliner's method in metasurface antenna design," in *2014 44th European Microwave Conference*, pp. 437–439, 2014.

[18] G. Minatti, F. Caminita, E. Martini, M. Sabbadini, and S. Maci, "Synthesis of modulated-metasurface antennas with amplitude, phase, and polarization control," *IEEE Transactions on antennas and propagation*, vol. 64, no. 9, pp. 3907–3919, 2016.

[19] O. Yurduseven, C. Lee, D. González-Ovejero, M. Ettorre, R. Sauleau, G. Chattopadhyay, V. Fusco, and N. Chahat, "Multibeam si/gaas holographic metasurface antenna at w-band," *IEEE Transactions on Antennas and Propagation*, vol. 69, no. 6, pp. 3523–3528, 2020.

[20] D. González-Ovejero, G. Minatti, G. Chattopadhyay, and S. Maci, "Multibeam by metasurface antennas," *IEEE Transactions on Antennas and Propagation*, vol. 65, no. 6, pp. 2923–2930, 2017.

[21] M. Bodehou, E. Martini, S. Maci, I. Huynen, and C. Craeye, "Multibeam and beam scanning with modulated metasurfaces," *IEEE Transactions on Antennas and Propagation*, vol. 68, no. 3, pp. 1273–1281, 2019.

[22] J. Ruiz-Garcia, M. Faenzi, A. Mahmoud, M. Ettorre, P. Potier, P. Pouliguen, R. Sauleau, and D. González-Ovejero, "Multi-beam modulated metasurface antenna for 5g backhaul applications at k-band," *Comptes Rendus. Physique*, vol. 22, no. S1, pp. 47–52, 2021.

[23] S. Biswas and M. Mirotznik, "High gain, wide-angle qcto-enabled modified luneburg lens antenna with broadband anti-reflective layer," *Scientific reports*, vol. 10, no. 1, p. 12646, 2020.

[24] Y. Wen, P.-Y. Qin, S. Maci, and Y. J. Guo, "Low-profile multibeam antenna based on modulated metasurface," *IEEE Transactions on Antennas and Propagation*, vol. 71, no. 8, pp. 6568–6578, 2023.

[25] A. Epstein and G. V. Eleftheriades, "Huygens' metasurfaces via the equivalence principle: design and applications," *JOSA B*, vol. 33, no. 2, pp. A31–A50, 2016.

[26] D. M. Kerns, *Plane-wave scattering-matrix theory of antennas and antenna-antenna interactions*, vol. 162.
US Department of Commerce, National Bureau of Standards, 1981.

[27] C. A. Balanis, *Antenna theory: analysis and design*.
John wiley & sons, 2015.

[28] W. Geyi, *Foundations of applied electrodynamics*.
John Wiley & Sons, 2011.

[29] D. R. Prado, "The generalized intersection approach for electromagnetic array antenna beam-shaping synthesis: A review," *IEEE Access*, vol. 10, pp. 87053–87068, 2022.

[30] S. Mikki and Y. Antar, *New Foundations for Applied Electromagnetics: The Spatial Structure of Electromagnetic Fields*.
Artech House, 2016.

[31] Y. Wen, P.-Y. Qin, G.-M. Wei, and R. W. Ziolkowski, "Circular array of endfire yagi-uda monopoles with a full 360 degree azimuthal beam scanning," *IEEE Transactions on Antennas and Propagation*, vol. 70, no. 7, pp. 6042–6047, 2022.

[32] M. Kahar and M. K. Mandal, "A wideband tightly coupled slot antenna for 360° full azimuthal beam steering applications," *IEEE Transactions on Antennas and Propagation*, vol. 69, no. 6, pp. 3538–3542, 2021.

[33] H. Fan, X. Liang, J. Geng, R. Jin, and X. Zhou, "Switched multibeam circular array with a reconfigurable network," *IEEE Transactions on Antennas and Propagation*, vol. 64, no. 7, pp. 3228–3233, 2016.

[34] L. Ge, M. Li, Y. Li, H. Wong, and K.-M. Luk, "Linearly polarized and circularly polarized wideband dipole antennas with reconfigurable beam direction," *IEEE Transactions on Antennas and Propagation*, vol. 66, no. 4, pp. 1747–1755, 2018.

[35] P.-Y. Wang, T. Jin, F.-Y. Meng, Y.-L. Lyu, D. Erni, Q. Wu, and L. Zhu, "Beam switching antenna based on a reconfigurable cascaded feeding network," *IEEE Transactions on Antennas and Propagation*, vol. 66, no. 2, pp. 627–635, 2018.

[36] D. V. Thiel and S. Smith, *Switched parasitic antennas for cellular communications*. Artech House, 2002.

[37] R. Schlub and D. Thiel, "Switched parasitic antenna on a finite ground plane with conductive sleeve," *IEEE Transactions on Antennas and Propagation*, vol. 52, no. 5, pp. 1343–1347, 2004.

[38] S. Preston, D. Thiel, and J. LU, "A multibeam antenna using switched parasitic and switched active elements for space-division multiple access applications," *IEICE transactions on electronics*, vol. 82, no. 7, pp. 1202–1210, 1999.

[39] R. Schlub, D. Thiel, J. Lu, and S. O'Keefe, "Dual-band six-element switched parasitic array for smart antenna cellular communications systems," *Electronics Letters*, vol. 36, no. 16, pp. 1342–1343, 2000.

[40] L. Zhang, S. Gao, Q. Luo, P. R. Young, and Q. Li, "Planar ultrathin small beam-switching antenna," *IEEE Transactions on Antennas and Propagation*, vol. 64, no. 12, pp. 5054–5063, 2016.

[41] R. Schlub, J. Lu, and T. Ohira, "Seven-element ground skirt monopole espar antenna design from a genetic algorithm and the finite element method," *IEEE Transactions on Antennas and Propagation*, vol. 51, no. 11, pp. 3033–3039, 2003.

[42] C. Gu, S. Gao, B. Sanz-Izquierdo, E. A. Parker, F. Qin, H. Xu, J. C. Batchelor, X. Yang, and Z. Cheng, "3-d coverage beam-scanning antenna using feed array and active frequency-selective surface," *IEEE Transactions on Antennas and Propagation*, vol. 65, no. 11, pp. 5862–5870, 2017.

[43] L. Zhang, Q. Wu, and T. A. Denidni, "Electronically radiation pattern steerable antennas using active frequency selective surfaces," *IEEE Transactions on Antennas and Propagation*, vol. 61, no. 12, pp. 6000–6007, 2013.

[44] B. Liang, B. Sanz-Izquierdo, E. A. Parker, and J. C. Batchelor, "Cylindrical slot fss configuration for beam-switching applications," *IEEE Transactions on Antennas and Propagation*, vol. 63, no. 1, pp. 166–173, 2015.

[45] A. Sarkar and S. Lim, "Annular surface plasmon polariton-based frequency-scanning leaky-wave antenna for full azimuth coverage," *IEEE Transactions on Antennas and Propagation*, vol. 70, no. 1, pp. 180–188, 2022.

[46] T. Maruyama, K. Uehara, and K. Kagoshima, "Analysis and design of multi-sector monopole yagi-uda array mounted on a ground plane using moment method," in *1996 Third International Conference on Computation in Electromagnetics (Conf. Publ. No. 420)*, pp. 289–294, 1996.

[47] M. D. Migliore and D. Pinchera, "Correction of beam direction in adaptive parasitic monopole arrays using a truncated cone structure," *IEEE Antennas and Wireless Propagation Letters*, vol. 11, pp. 1486–1488, 2012.

[48] D. Thiel, "Optimised slot reradiation to modify foreground reflection into an array," in *Proceedings of the Institution of Electrical Engineers*, vol. 120, pp. 962–964, IET, 1973.

[49] Z. Liang, Y. Li, J. Liu, S. Y. Zheng, and Y. Long, "Microstrip magnetic monopole end-fire array antenna with vertical polarization," *IEEE Transactions on Antennas and Propagation*, vol. 64, no. 10, pp. 4208–4217, 2016.

[50] N. Honma, T. Seki, K. Nishikawa, K. Tsunekawa, and K. Sawaya, "Compact six-sector antenna employing three intersecting dual-beam microstrip yagi,Äìuda arrays with common director," *IEEE Transactions on Antennas and Propagation*, vol. 54, no. 11, pp. 3055–3062, 2006.

[51] J. E. Hansen, *Spherical near-field antenna measurements*, vol. 26.
Iet, 1988.

[52] M. M. Idemen, *Discontinuities in the electromagnetic field*.
John Wiley & Sons, 2011.

[53] V. S. Asadchy, A. Díaz-Rubio, and S. A. Tretyakov, "Bianisotropic metasurfaces: physics and applications," *Nanophotonics*, vol. 7, no. 6, pp. 1069–1094, 2018.

[54] E. F. Kuester, M. A. Mohamed, M. Piket-May, and C. L. Holloway, "Averaged transition conditions for electromagnetic fields at a metafilm," *IEEE Transactions on Antennas and Propagation*, vol. 51, no. 10, pp. 2641–2651, 2003.

[55] M. A. Francavilla, E. Martini, S. Maci, and G. Vecchi, "On the numerical simulation of metasurfaces with impedance boundary condition integral equations," *IEEE Transactions on Antennas and Propagation*, vol. 63, no. 5, pp. 2153–2161, 2015.

[56] M. Albooyeh, D.-H. Kwon, F. Capolino, and S. Tretyakov, "Equivalent realizations of reciprocal metasurfaces: Role of tangential and normal polarization," *Physical Review B*, vol. 95, no. 11, p. 115435, 2017.

[57] M. Faenzi, G. Minatti, D. González-Ovejero, F. Caminita, E. Martini, C. Della Giovampaola, and S. Maci, "Metasurface antennas: New models, applications and realizations," *Scientific reports*, vol. 9, no. 1, pp. 1–14, 2019.

[58] Y. J. Guo and R. W. Ziolkowski, *Advanced Antenna Array Engineering for 6G and Beyond Wireless Communications*.
John Wiley & Sons, 2021.

[59] J.-W. Lian, Y.-L. Ban, and Y. J. Guo, "Wideband dual-layer huygens' metasurface for high-gain multibeam array antennas," *IEEE Transactions on Antennas and Propagation*, vol. 69, no. 11, pp. 7521–7531, 2021.

[60] Y. Liu, H. Yang, Z. Jin, F. Zhao, and J. Zhu, "A multibeam cylindrically conformal slot array antenna based on a modified rotman lens," *IEEE Transactions on Antennas and Propagation*, vol. 66, no. 7, pp. 3441–3452, 2018.

[61] Y. J. Cheng, W. Hong, and K. Wu, "Millimeter-wave substrate integrated waveguide multibeam antenna based on the parabolic reflector principle," *IEEE Transactions on Antennas and Propagation*, vol. 56, no. 9, pp. 3055–3058, 2008.

[62] L.-Z. Song, P.-Y. Qin, H. Zhu, and J. Du, "Wideband conformal transmitarrays for e-band multi-beam applications," *IEEE Transactions on Antennas and Propagation*, vol. 70, no. 11, pp. 10417–10425, 2022.

[63] P.-Y. Qin, L.-Z. Song, and Y. J. Guo, "Conformal transmitarrays for unmanned aerial vehicles aided 6g networks," *IEEE Communications Magazine*, vol. 60, no. 1, pp. 14–20, 2022.

[64] L.-Z. Song, P.-Y. Qin, S.-L. Chen, and Y. J. Guo, "An elliptical cylindrical shaped transmitarray for wide-angle multibeam applications," *IEEE Transactions on Antennas and Propagation*, vol. 69, no. 10, pp. 7023–7028, 2021.

[65] Y. Hu, W. Hong, and Z. H. Jiang, "A multibeam folded reflectarray antenna with wide coverage and integrated primary sources for millimeter-wave massive mimo applications," *IEEE Transactions on Antennas and Propagation*, vol. 66, no. 12, pp. 6875–6882, 2018.

[66] Y. J. Guo, M. Ansari, and N. J. Fonseca, "Circuit type multiple beamforming networks for antenna arrays in 5g and 6g terrestrial and non-terrestrial networks," *IEEE Journal of Microwaves*, vol. 1, no. 3, pp. 704–722, 2021.

[67] C. A. Guo and Y. J. Guo, "A general approach for synthesizing multibeam antenna arrays employing generalized joined coupler matrix," *IEEE Transactions on Antennas and Propagation*, vol. 70, no. 9, pp. 7556–7564, 2022.

[68] H.-T. Chou, "An effective design procedure of multibeam phased array antennas for the applications of multisatellite/coverage communications," *IEEE Transactions on Antennas and Propagation*, vol. 64, no. 10, pp. 4218–4227, 2016.

[69] G. Minatti, F. Caminita, M. Casaletti, and S. Maci, "Spiral leaky-wave antennas based on modulated surface impedance," *IEEE Transactions on antennas and propagation*, vol. 59, no. 12, pp. 4436–4444, 2011.

[70] A. T. Pereda, F. Caminita, E. Martini, I. Ederra, J. C. Iriarte, R. Gonzalo, and S. Maci, "Dual circularly polarized broadside beam metasurface antenna," *IEEE Transactions on Antennas and Propagation*, vol. 64, no. 7, pp. 2944–2953, 2016.

[71] A. T. Pereda, F. Caminita, E. Martini, I. Ederra, J. Teniente, J. C. Iriarte, R. Gonzalo, and S. Maci, "Experimental validation of a ku-band dual-circularly polarized metasurface antenna," *IEEE transactions on antennas and propagation*, vol. 66, no. 3, pp. 1153–1159, 2018.

[72] G. Minatti, M. Faenzi, M. Sabbadini, and S. Maci, "Bandwidth of gain in metasurface antennas," *IEEE transactions on antennas and propagation*, vol. 65, no. 6, pp. 2836–2842, 2017.

[73] Y. J. Guo and R. W. Ziolkowski, *Antenna and Array Technologies for Future Wireless Ecosystems*.
John Wiley & Sons, 2022.

[74] A. M. Patel and A. Grbic, "A printed leaky-wave antenna based on a sinusoidally-modulated reactance surface," *IEEE transactions on antennas and propagation*, vol. 59, no. 6, pp. 2087–2096, 2011.

[75] S. Maci, G. Minatti, M. Casaletti, and M. Bosiljevac, "Metasurfing: Addressing waves on impenetrable metasurfaces," *IEEE Antennas and Wireless Propagation Letters*, vol. 10, pp. 1499–1502, 2011.

[76] M. ElSherbiny, A. E. Fathy, A. Rosen, G. Ayers, and S. M. Perlow, "Holographic antenna concept, analysis, and parameters," *IEEE Transactions on Antennas and Propagation*, vol. 52, no. 3, pp. 830–839, 2004.

[77] G. Minatti, M. Faenzi, E. Martini, F. Caminita, P. De Vita, D. González-Ovejero, M. Sabbadini, and S. Maci, "Modulated metasurface antennas for space: Synthe-

sis, analysis and realizations," *IEEE Transactions on Antennas and Propagation*, vol. 63, no. 4, pp. 1288–1300, 2014.

[78] G. Minatti, F. Caminita, E. Martini, and S. Maci, "Flat optics for leaky-waves on modulated metasurfaces: Adiabatic floquet-wave analysis," *IEEE Transactions on Antennas and Propagation*, vol. 64, no. 9, pp. 3896–3906, 2016.

[79] G. Minatti, E. Martini, and S. Maci, "Efficiency of metasurface antennas," *IEEE Transactions on Antennas and Propagation*, vol. 65, no. 4, pp. 1532–1541, 2017.

[80] N. Montaseri and A. Mallahzadeh, "Modulated reactance surfaces with several modulation indices for multibeam leaky-wave antenna design," *IEEE Transactions on Antennas and Propagation*, vol. 68, no. 12, pp. 8156–8161, 2020.

[81] A. M. Hakimi, H. Oraizi, A. Keivaan, and A. Amini, "Wideband vertically polarized dual-beam antenna using modulated metasurfaces," in *2020 14th European Conference on Antennas and Propagation (EuCAP)*, pp. 1–5, IEEE, 2020.

[82] Y. B. Li, X. Wan, B. G. Cai, Q. Cheng, and T. J. Cui, "Frequency-controls of electromagnetic multi-beam scanning by metasurfaces," *Scientific reports*, vol. 4, no. 1, p. 6921, 2014.

[83] Y. Shen, S. Xue, J. Yang, and S. Hu, "Tensor holographic metasurface using addition theory to independently manipulate orthogonally polarized bessel beams," *Advanced Materials Technologies*, vol. 6, no. 4, p. 2001047, 2021.

[84] M. Bodehou and C. Craeye, "Array surface-wave launcher for the efficient generation of shaped beam and multibeam with metasurface," *IEEE Transactions on Antennas and Propagation*, vol. 69, no. 12, pp. 8860–8865, 2021.

[85] Y. Li, A. Li, T. Cui, and D. F. Sievenpiper, "Multiwavelength multiplexing hologram designed using impedance metasurfaces," *IEEE Transactions on Antennas and Propagation*, vol. 66, no. 11, pp. 6408–6413, 2018.

[86] M. Faenzi, D. González-Ovejero, and S. Maci, "Design methodologies for dual-band modulated metasurface antennas," in *2021 Fifteenth International Congress on Artificial Materials for Novel Wave Phenomena (Metamaterials)*, pp. 138–140, IEEE, 2021.

[87] Y. Shen, S. Xue, G. Dong, J. Yang, and S. Hu, "Multiplexing tensor holographic metasurface with surface impedance superposition for manipulating multibeams with multimodes," *Advanced Optical Materials*, vol. 9, no. 22, p. 2101340, 2021.

[88] Y. Zhou, X. Qing, *et al.*, "Switched beam steering antenna system at ka-band," in *2021 IEEE International Symposium on Antennas and Propagation and USNC-URSI Radio Science Meeting (APS/URSI)*, pp. 563–564, IEEE, 2021.